EXPERIMENTAL STUDY OF THE TURBULENT MIXING OF TWO PARALLEL JETS FOR BENCHMARKING NUMERICAL MODELS

A Dissertation

by

HUHU WANG

Submitted to the Office of Graduate and Professional Studies of
Texas A&M University
in partial fulfillment of the requirements for the degree of

DOCTOR OF PHILOSOPHY

Chair of Committee,	Yassin A. Hassan
Committee Members,	Hamn-Ching Chen
	Maria King
	William H. Marlow
Head of Department,	Yassin A. Hassan

December 2015

Major Subject: Nuclear Engineering

ABSTRACT

Turbulent mixing of parallel jet flows has broad engineering applications. For example, in Gen IV conceptual nuclear reactors, high-temperature flows mix in the lower plenum before entering the secondary cooling system. The mixing condition needs to be accurately estimated and fully understood. In addition, massive computational works involved in the design process necessitate high-fidelity experimental data sets for benchmarking simulation results.

The purpose of this study is to use laser Doppler anemometry (LDA) and particle image velocimetry (PIV), both non-intrusive measuring techniques, to evaluate the mixing characteristics of two submerged parallel jets issuing from two rectangular channels. Flow characteristics including distributions of mean velocities, turbulence intensities, and Reynolds stresses were studied for the cases with equal and non-equal discharge velocities. The locations of the merging point (MP) and combining point (CP) were found. Spectral analyses including fast Fourier transform, power spectral density estimation and continuous wavelet transform of a segment of the LDA results revealed the scale and the evolution in time of varied-size eddies in the mixing region of the flow. At last, the results obtained from LDV and PIV with two different magnification factors were compared, and the discrepancies were quantified.

The experimental data obtained from the LDA and PIV measurements of the averaged quantities and transient are not only valid for benchmarking steady-state

numerical simulations using turbulence models to solve RANS equations but they also enlarge the database of the experimental data for twin jets.

DEDICATION

To my father

ACKNOWLEDGEMENTS

I would like to thank my advisor, Dr. Yassin A. Hassan, and my committee members, Dr. Hamn-Ching Chen, Dr. Maria King and Dr. William H. Marlow for their help and encouragement.

Second thanks go to my colleagues in the lab. Thank you all for your support.

I thank my mother, my wife, younger brother, my newly-born son Easton, Coach Linda for loving me and having faith in me. My sincere thankfulness go to my dear and deeply respected father Laufu Wang who passed away on Jan. 21, 2013. I would not have been able to finish my study without his blessings from heaven.

NOMENCLATURE

U	Streamwise Velocity
V	Lateral Velocity
a	Jet Width
S	Jet Spacing, the Distance between the Centers of Two Jets
l	Jet Length
x	X Axis which is Perpendicular to the Direction of Main Stream
y	Y Axis which is Parallel to the Direction of Main Stream
z	Z Axis which is Perpendicular to the x-y Plane
U_{max}	Local Maximum Value of U
U_0	Average Discharge Velocity of the Jet
U_{rms}	Root Mean Square Value of U
V_{rms}	Root Mean Square Value of V
ω	Z-component Vorticity
MP	Merging Point
CP	Combing Point
N	Number of Samples
R	Velocity Ratio between the Left and Right Jet

TABLE OF CONTENTS

Page

LIST OF FIGURES

LIST OF TABLES

1. INTRODUCTION[*]

High temperature gas-cooled and sodium-cooled reactors have been designated as two of the six candidate reactors for next generation, also Generation IV, (Gen. IV) nuclear power plants. The design process needs large amounts of numerical simulations such as computational fluid dynamics (CFD) computations and, as any large-scale experiments requires significant amount of money and time. However, the inherent uncertainties existing in the turbulence models and wall functions of any CFD codes solving Reynolds-averaged Navier-Stokes (RANS) equations negatively influence the credibility of the CFD simulation results. This necessitates high-fidelity experimental data sets for benchmarking these results.

In Gen. IV reactors, mixing of high-temperature flows appears in the lower plenum. The spacing ratio of the jets is relatively small, for instance in the sodium-cooled reactor, compared to those in the external aerodynamics applications. The mixing condition and the mixing length are of great importance to the reactor safety because of the existence of thermal stresses and possible temperature oscillations induced by the turbulent mixing. These temperature oscillations will further result in output power instabilities. In this work, two submerged parallel waters jets issuing from two

---

[*] Part of the content in this section is reprinted with permission from “Laser-Doppler Measurements of the Turbulent Mixing of Two Rectangular Water Jets Impinging on a Stationary Pool” by Wang, H., et al., 2016. International Journal of Heat and Mass Transfer, Vol. 92, 206-227, Copyright [2016] by Elsevier.

rectangular channels, also known as twin-jet flow, were selected to study the turbulent mixing phenomenon.

Different from a single jet flow, twin jets issuing from two adjacent rectangular slots are characterized by the formation of a subatmospheric pressure region due to the mutual entrainment of the two jets. This negative-pressure region deflects the jets, causing them to move toward each other and form a converging region. Inside this region, strong recirculation near the slot area create a flow reversed with respect to the direction of the main flow. The converging region ends at the merging point (MP) which is defined as the point at which the mean velocity is zero along the symmetry axis [1]. Beyond this point the jets start to combine until they form a single jet at the combining point (CP). The region between the MP and the CP is called the merging region. The combined jet then behaves as a single jet and analytical solutions derived for a single jet hold in this combined region. The mixing does not only happen between the jets themselves but also between the jets and the static surrounding fluid that was entrained as a result of the shear force created. In engineering applications, knowing the length of the mixing region and the locations of the CP and MP are often important to ensure a good mixing. The schematic structure of a typical twin jet is shown in Fig. 1.

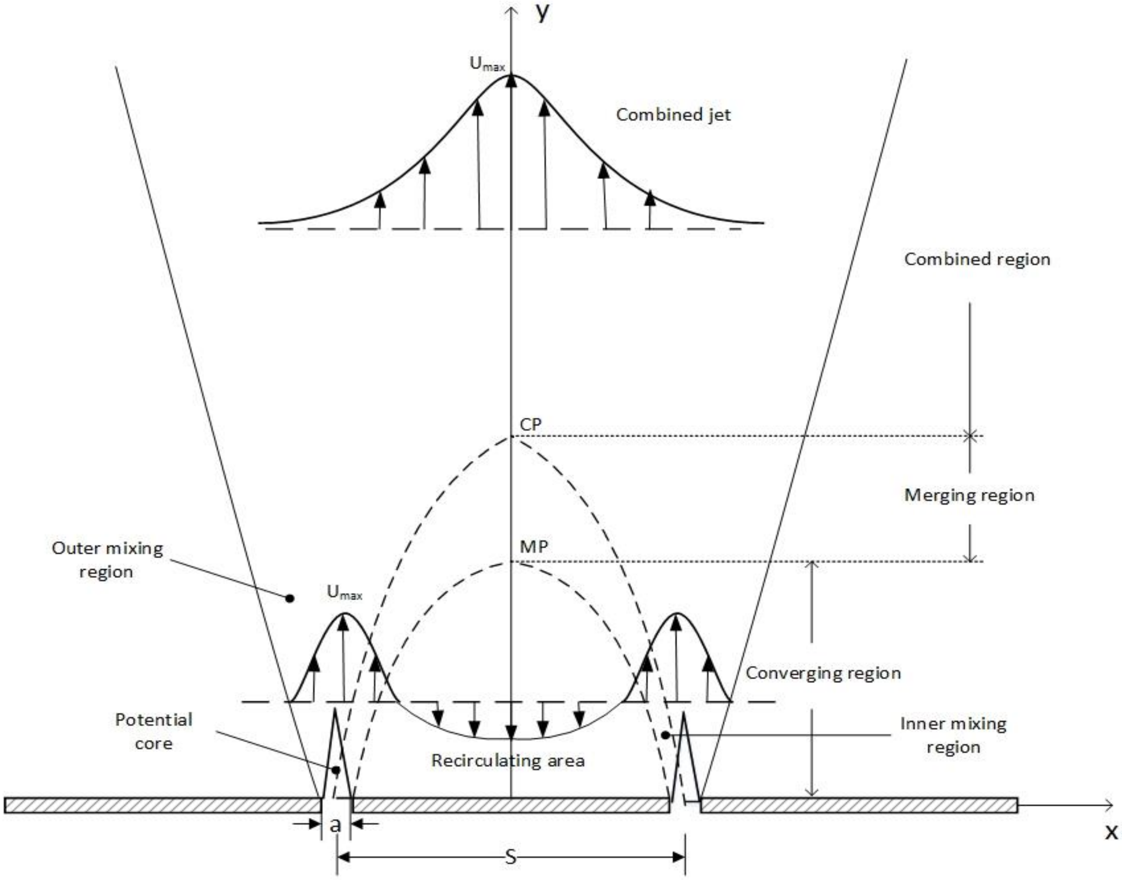

Fig. 1. Diagram of a typical twin jet system. *a* is the channel width, *S* is the distance between centers of the two jets, U_{max} is the local maximum velocity in the streamwise direction, *x* is the coordinate perpendicular to the direction of the jets, *y* is the coordinate along the streamwise direction, CP stands for the combining point, and MP is the merging point [30].

In 1959 Miller and Comings [2] made the first measurements of the 2-D twin jets using a constant temperature hot-wire anemometer (HWA). The non-dimensional jet spacing ratio, the ratio between the jet spacing S and the jet diameter a, was 6. By measuring the mean and fluctuating velocity as well as the static pressure and comparing them to a single jet, they found that the flow of the 2-D twin jets had a high degree of symmetry about the centerline of jets. The two jets merged at certain location behaving as a single jet. This location was defined as the separating point of the converging region and the combined region. Before the MP, there was a stagnation point, also called the combining point, at which point the static pressure gradient and the turbulent shear stress force were equal but with different signs.

Tanaka [3] conducted a similar measurement using a dual jet of air issuing from parallel slot nozzles but focused on the effect of the spacing ratio ranging from 8.5 to 25. The static pressure was determined to be negative near the nozzle region but suddenly increased to atmospheric pressure or even higher after the free stagnation point [3]. The author also concluded that the streamwise velocity distribution was independent of the Reynolds number within the limits of velocity studied. An empirical equation relating the curvature of the central stream-line of the jet and the nozzle distance was proposed. In another report [4], the combined flow of the twin jets was found to have a velocity distribution similar to a single jet with its width spread linearly downstream. The decay of the center velocity was stronger than that of a single jet.

A crude integral model of two parallel jets was proposed, and the results predicted the mixing behavior surprisingly well, despite the fact that the model overpredicted the entrainment rates. The experiments revealed that the velocity distributions were self-preserved upstream and downstream of the merging region [5]. Elbanna and Gahin [6] evaluated the turbulent characteristics of the twin jets and compared with the behavior of a single jet. The spacing between the two nozzles applied was 12.5 slot widths. The results indicated that the half-width of the combined flow grew linearly in the direction of the stream but the spread angle was slightly smaller than that of a single jet.

Research on non-equal parallel jets studied shows that the slower jet was more attracted to the faster jet when the velocity ratio decreased [7]. However, the total momentum, including the velocity and pressure momentum, was still conserved. Using a similar measuring technique, the distributions of the overall Reynolds stress and the velocity fluctuations of two parallel jets with a spacing ratio of about 2.5 was evaluated, and the presence of inner and outer mixing regions in each jet was found [8]. The directions of rotation of the inner and outer vortices were opposite. The jets did not converge because side plates were not installed in the experiment. Later, Lin and Sheu [9] reported that for 2-D plane jets with spacing ratios of 30 and 40 and a nozzle width of 2 mm, the mean velocity was self-preserving in the converging region and the combined region. The fluctuating velocities and the Reynolds stress presented a self-preserving behavior in the combined region only. Their experiments confirmed that the jet widths increased linearly in the converging region and combined region [9]. Although used for numerous other purposes prior to this, in 1977 the non-intrusive measuring technique laser Doppler anemometry (LDA), also called laser Doppler velocimetry, was first used to study a twin jet flow field [10]. The spacing ratio was 4.25 and the nozzle exit Reynolds number was 11,000. The spectral analysis showed that the vortex roll-up frequency in the outer shear layer was the same as that of a single jet. The experimental results also indicated that the dynamics of the twin jets was strongly related to the development of the coherent structures generated from the shear layer instability

[10]. LDA was also used to explore the impinging flow of two water jets, evaluating the effect of the jet imbalance [11]. This work showed that several flow features captured by the LDA were likely to be important to CFD model validation studies.

A study that investigated 2-D parallel jets with spacing ratios between 9 and 18.25 evaluated the standard k-e model and Reynolds stress transport model by comparing the numerical results with the experimental data [12]. The results indicated that the CFD technique was capable of estimating the location of the merging and combining points. HWA measurements showed that a convex surface deflects the jets stronger than a flat surface in the case of two parallel rectangular jets with a small spacing ratio [1]. The researchers provide detailed experimental conditions such as the turbulence intensity at the nozzle exit section and the initial boundary conditions. The initial condition is very valuable especially for comparisons with numerical results and experimental data from other researchers. However, the majority of publications mentioned above fail to provide detailed initial and boundary conditions.

For a small spacing ratio of 1.89, the normalized streamwise mean velocity was found to remain independent of the Reynolds number [13]. The authors suggest that the mixing length could be increased by reducing the spacing ratio or increasing the Reynolds number. A superposition technique based on Reichardt's hypothesis can predict the flow pattern well given the condition that the jet deflection was not significant [14]. Obviously, this method does not work if the spacing ratio is too small as the jet deflection under this condition is significant.

Most of the previous studies in this field have used a relatively large spacing ratio [e.g., 2, 3, 4, 6, 7, 9, and 12]. However, in many engineering applications, such as coolant mixing in the lower plenum in a VHTR, the spacing ratio is relatively small. This necessitates more work focused on the jets from nozzles with a small spacing ratio. In addition, the majority of studies to date have used HWA to measure the air flow in a wind tunnel [e.g., 1-9, 12, 13]. The main issue with HWA measurements is the lack of ability to measure reversed flows accurately, such as the flow in the converging region of a twin-jet flow. Nasr and Lai [10] applied LDA to the study of the mixing phenomenon but the seeding particles used, like fog fluid, may introduce significant errors. These fog particles amalgamate to form larger particles, which are too heavy to follow the flow.

Table 1 summarizes the previous studies of the parallel jets under varied experimental conditions. It was reported that the velocity field and the turbulence characteristics were functions of the spacing ratio S/a and the aspect ratio l/a [2]. Previous works have mainly focused on large spacing ratios and aspect ratios. However, these ratios are relatively small in nuclear reactors. Moreover, the working fluid reported was mainly air, and the measuring technique used was a hot-wire anemometer (HWA). Although the governing equations are the same for water and air, the type of working fluids will introduce different measurement uncertainties and challenges into the specific experiments. Compared to HWA, PIV is superior in handling the reversed flows, which exist in the recirculating zone of the parallel jets.

There has not been a valid empirical correlation proposed so far to accurately predict the flow field of the twin jets flow according the previous literature survey. One of the main reasons is the lack of high-fidelity experimental data. Thus, the purpose of this work is to investigate the turbulent mixing phenomenon of parallel jets with a small spacing ratio by performing 2-D LDA and PIV measurements. The results can enlarge the experimental database of the twin jets and help better understand its mixing characteristics. Furthermore, the LDA and PIV data can be utilized to validate the numerical models, e.g., the turbulence models in the CFD simulations which are heavily used in the design process. Spectral analysis of a fluctuation velocity signal obtained by LDA can provide an insight into the flow structures which cannot be revealed by the investigation of averaged quantities. However, the applications of spectral analysis on the study of twin water jets with small spacing ratios have rarely been reported in the literature. Thus, spectral analysis by employing methods such as fast Fourier transform, power spectrum density estimation, and continuous wavelet transform will be carried out to explore the flow behaviors in the mixing region.

Table 1. Summary of the literature review [31]

Year	Authors	Working fluid	Spacing ratio (S/a)	Aspect ratio (l/a)	Re	Measuring tools	Contributions
1959 [1]	Miller and Comings	Air	6	very large	17,800	Hot-wire anemometer	Symmetry, Merging into single jet, MP = 7
1970 [2]	E. Tanaka	Air	8.5 - 26.3	very large	4,290 - 8,750	Hot-wire anemometer	Negative pressure region, Independence of Re
1974 [3]	E. Tanaka	Air	8.5 - 26.3	very large	4,290 - 8,751	Hot-wire anemometer	For S/a =20, MP = 13~15a, CP=30a
1977 [4]	G.F. Marsters	Air	17.25	40	12,000	Hot-wire anemometer	Proposed a crude integral model
1983 [5]	H. Elbanna and S. Gahin	Air	12.5	40.8	20,000	Hot-wire anemometer	Half-width of the combined flow grew linearly
1987 [6]	H. Elbanna and S. Gahin	Air	27.64	89	n/a	Hot-wire anemometer	CP = 60 for equal velocity, studied uneven jets
1989 [7]	N.W.M. Ko and K.K. Lau	Air	2.5	5.6	10,000	Hot-wire anemometer	MP = 2.5a, CP = 10.5a
1990 [8]	Y.F. Lin and M.J. Sheu	Air	30 & 40	90	9,000	Hot-wire anemometer	For S/a=30a, MP = 40, CP = 60a
1997 [9]	A. Nasr and J.C.S. Lai	Air	4.25	24	11,000	LDA (using frog fluids)	MP = 4a, CP = 8a
1998 [10]	P. Behrouzi and J. J. Mcguirk	Water	13	n/a	37,500	LDA	Flow Impingement
2001 [11]	E. A. Anderson and R. E. Spall	Air	9 - 18.25	32	5,900 - 6,100	Hot-wire anemometer	For S/a = 9, MP = 12a, CP = 19a
2007 [12]	Z. Q. Yin et. al	Air	1.5, 1.75, 1.89	6.8	33,300 - 83,300	Hot-wire anemometer	U was independent of Reynolds number
2011 [13]	A. Nasr and J. Lai	Air	2.5	n/a		LDA & Numerical	MP = 1.75a, CP = 4.4a, the proposed model didn't work for small S/a

2. EXPERIMENTAL METHODS*

2.1 Laser Doppler anemometry (LDA) method

2.1.1 Principle of LDA

The principle of the LDV (Fringe model) is based on the Doppler frequency shift caused by particles passing through the intersection (measuring volume) of two coherent laser beams as shown in Fig. 2, producing a burst signal. Then the velocity of this moving particle can be calculated based on this shift frequency. The direction of the flow is determined with the help a Bragg cell generating a positive and a negative frequency shift. The accuracy of the LDA results highly rely upon the laser power, laser wavelength, optic alignments, and the seeding particles.

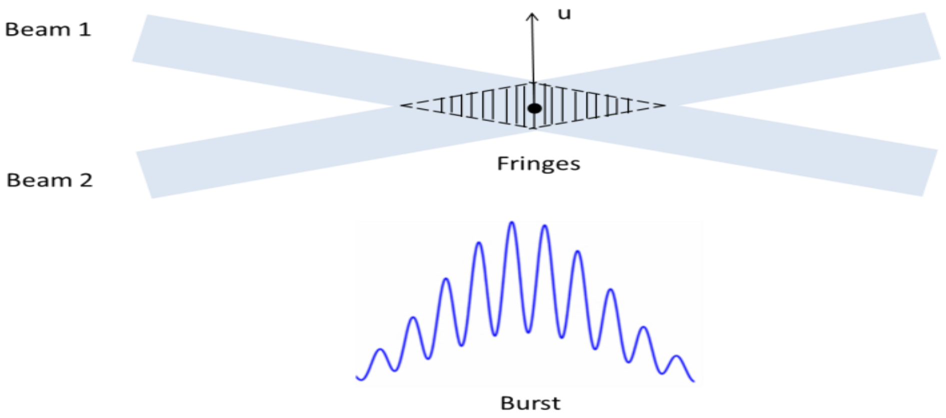

Fig. 2. Principle of LDV (Fringe Model) [30]

---

*Parts of this section are reprinted with permission from “Laser-Doppler Measurements of the Turbulent Mixing of Two Rectangular Water Jets Impinging on a Stationary Pool" by Wang, H., et al., 2016. International Journal of Heat and Mass Transfer, Vol. 92, 206-227, Copyright [2016] by Elsevier.

2.1.2 Experimental setup

The experiment was performed in a water tunnel. The experimental rig, not including the measuring instrumentations, was the one used in Crosskey and Ruggles's work [15]. Fig. 3 presents a snapshot of the setup. The flow was driven by two identical 0.5 horsepower pumps. The control of the two jets was independent. The flow meter used was GPI TM100 with an accuracy of 97% and repeatability of 95%. The 1-inch thick water tank with dimensions of 1016 mm by 762 mm was made of acrylic to provide an optical access to the flow inside. The experiment setup was a closed loop with water recycled to the tank. Two identical rectangular channels were located at the center of the tank. The length of each channel was 87.6 mm and the width 5.8 mm making the aspect ratio 15.1. The centers of each channel were 17.8 mm apart, giving a spacing ratio of 3.07. Each channel is 279.4 mm high to ensure that the exit flow is a fully developed turbulent flow. The detailed dimensions and the corresponding coordinates used in this work are shown in Fig. 4. The LDA system was from Dantec and included a 2-D flow explorer with a laser head and photomultiplier tube, a 3-D transverse system with accuracy of 0.01mm, and a data acquisition system.

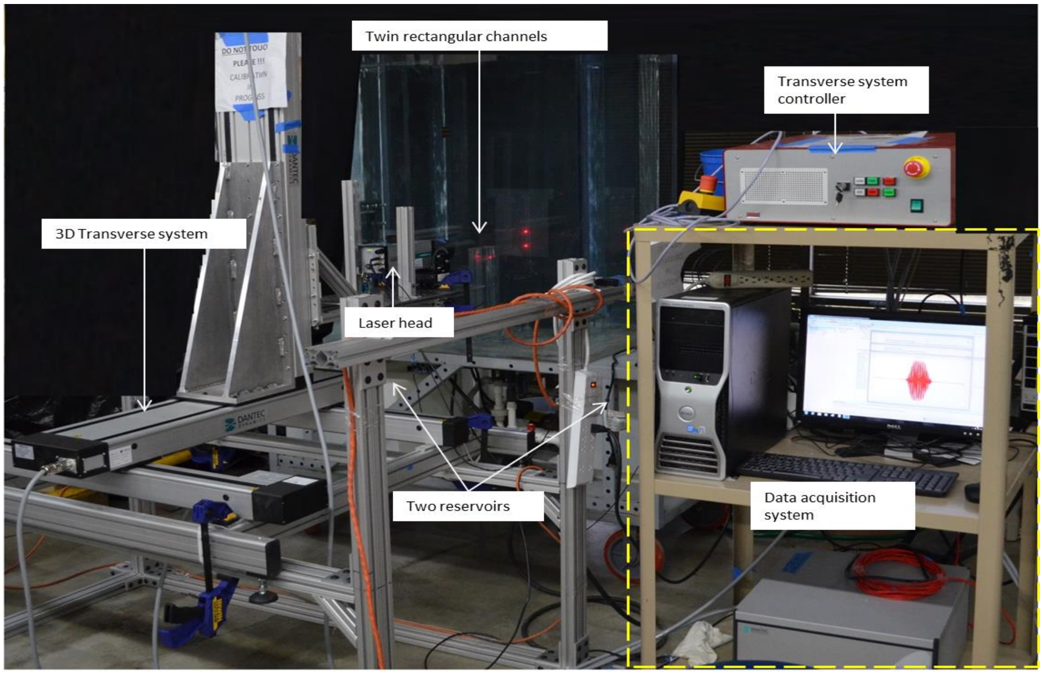

Fig. 3. Experimental setup [30]

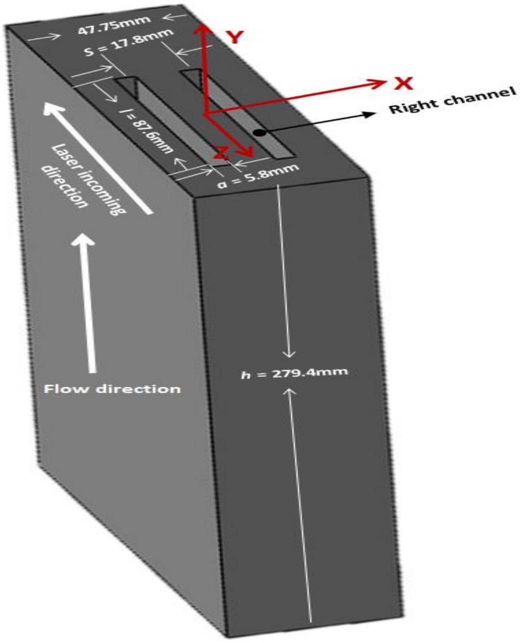

Fig. 4. Detailed dimensions of the twin rectangular channels [30]

The 2-D flow measurements were performed using the fringe-mode based Dantec LDV optics which has a back-scattering arrangement. The focal length of the two laser beams was 500 mm with wavelengths of 660 nm and 785nm. The laser beam had a diameter of 2.5 mm and a nominal power of 35 mW. Each beam was split into two beams after passing an 80 MHz Bragg cell and intersected with the other at a half-crossing angle of 3.43 °. The seeding particle used was hollow glass spheres from TSI with a centered diameter of 10μm. The seeding concentration was about 1.9 g/m^3 which was optimized to increase the signal-to-noise ratio (SNR). The tradeoff was that higher concentration of particles reduced the light intensity in water significantly. On average, 3000 samples were taken at each location, except at those located near the outer mixing region where the data rate was extremely low. The LDA measurements were operated in coincidence mode meaning that the u and v components were acquired simultaneously. This mode could reduce the data rate significantly especially for the jet flow. It is because under this mode the bursts from both u and v components must be recognizable in order for them to be counted as valid signals. If the magnitude of one of them, for example *v* component, is too small and then a low data rate will be generated no matter how large the *u* component is. That is the exact case for jet flows in which the lateral v component is very small in most regions at the most of time. In this study, the data rate ranged from 10 Hz in the almost static region to 150 Hz in the core flow region, which was the maximum frequency that could be reached in the experiment with respect to the high SNRs. The low frequency may also be attributed to many factors, such as low power laser beams, attenuations by thick wall of the tank and relatively low particle concentrations in the outer mixing region. A higher data rate of about 200 Hz was obtained by operating the LDA in the 1-componennt mode to perform the spectral analysis.

2.1.3 Calibration procedure

For LDA measurements, the influence of the light refraction from the surface of the water tank and from the water itself needs to be addressed. That is, the system must be calibrated in order to know the exact position of the measuring volume in the water. This system was calibrated by taking photos of the measuring volume where the beams cross as presented in Fig. 5. Then by calculating the relative position in pixels of the measuring volume to the center of the edge the channels, the calibration factor was obtained. Due to the crossing angle of the two beams, the lowest accessible position along the Y-axis was located at 10 mm above the channel surface. The measurements were carried out at the middle plane, P2 as shown in Fig. 5.

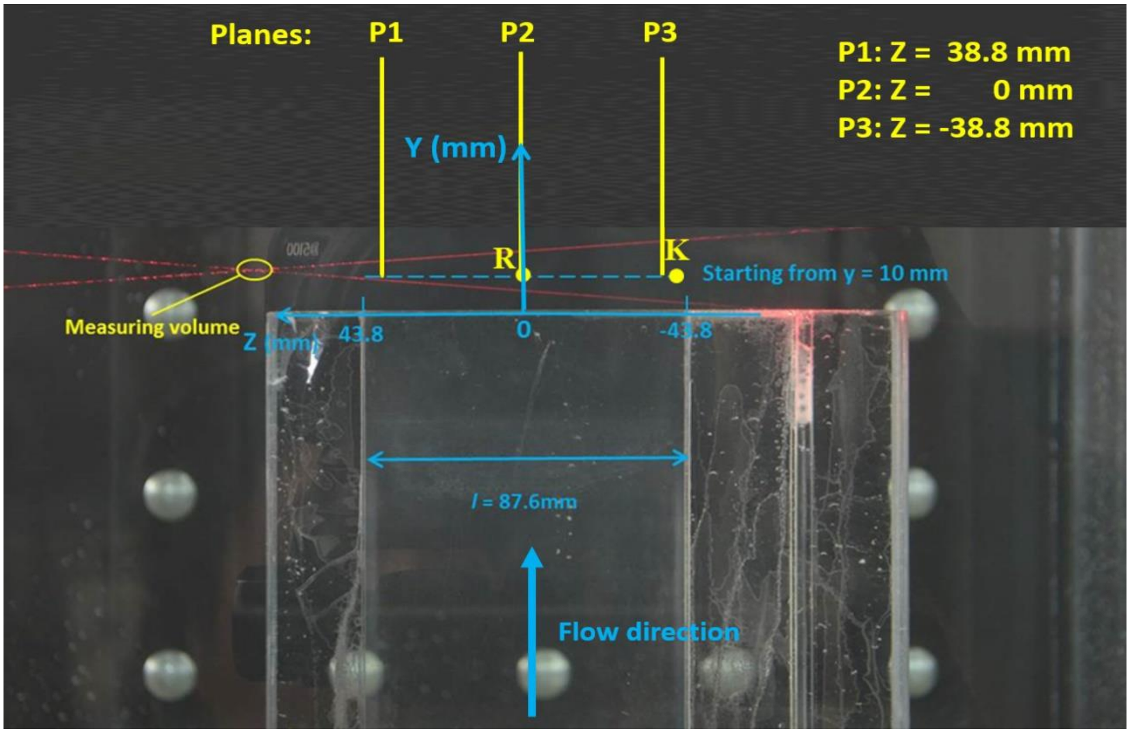

Fig. 5. Calibration of the measuring volume position in water [30]

2.1.4 Measurement uncertainties

For all LDA measurements, many uncertainties are involved. Unfortunately, a few important factors are sometimes beyond the researchers' control [J. F. Meyers, personal communication, March 2014], such as the particle tacking fidelity, seeding bias, influence of the scattered light on the signal quality, and photo resolved signal bursts owing to insufficient scattered light. The particle size distribution is another source of uncertainty which is difficult to quantify. However, a study from F. Durst and B. Ruck [16] suggested that the maximum diameter of the particle should be less than 2 to 2.5 times the average diameter to achieve the optimum size distribution for LDA measurements. The particles used in this work have a nominal mean diameter of 8 μm to 12 μm. 90% of the particles have a diameter of 14 μm to 17 μm. Therefore, the ratio between the maximum diameter and the average diameter meets the requirement.

In this study, the LDA measurements cannot be finished within a short period of time due to the low data rates in some regions. So, a single measurement task may last a few days and require the experimental facility to be turned on and off multiple times. The flow rate is controlled by two plastic ball valves and sometimes flow rates shift. The stability of the pumps and the velocity shift are monitored by recording the readings of the flow meters. The maximum velocity shift within each measurement period was about 0.66%. Moreover, readings from the flow rate fluctuate continuously due to the nature of turbulence. Thus, considering all these effects, a certain degree of error must have been introduced to results reported in this work.

To quantify these uncertainties, the same measurement of the flow parameters including the mean and the fluctuating velocities at the center of the right channel along the y-direction was repeated five times within five days. Only u-component of the LDA was activated. Figs. 6 and 7 show the results. In order to demonstrate the absolute values of the errors associated with results reported previously, the flow parameters were not normalized. The error bars in the figures represent the standard deviations, which are small, of five measurements performed each day for five days for a total of 25 measurements.

For the mean velocity, the main discrepancies were from the locations in the combining region. This is not surprising because it is the most complicated region for this type of flow, and small perturbations from the initial and boundary conditions result in significant changes to the results. The largest error was approximately 9% for days 1 and 4 at y/a = 5.17, where y is the distance from coordinate along Y-axis. For the fluctuating velocity, the largest error came from y/a = 3.45, again for days 1 and 4. The error was about 12%. However, the average standard deviations of the U and U_{rms} measurements at all locations over the five days were 1.5% for U and 1.6% for U_{rms}. Thus, the overall error resulting from the long measuring window were insignificant.

Another possible source of error is the sampling size. For the majority of the regions, 3000 samples were taken at each measuring point. To evaluate the uncertainty in the sampling process, the standard error of the mean (SEM) of the Reynolds stress component $\overline{U'V'}$ at point x/a = -0.86, y/a = 5.17 were studied. The SEM is the ratio of the standard deviation, σ, of the whole population and the square root of the sample size N, with the results shown in Fig. 8. The smallest SEM is equal to 0.00038 m^2/s^2 when N is equivalent to 3000, 4.3% of the mean of the Reynolds stress. Consequently, 4.3% is the maximum uncertainty in the sampling process.

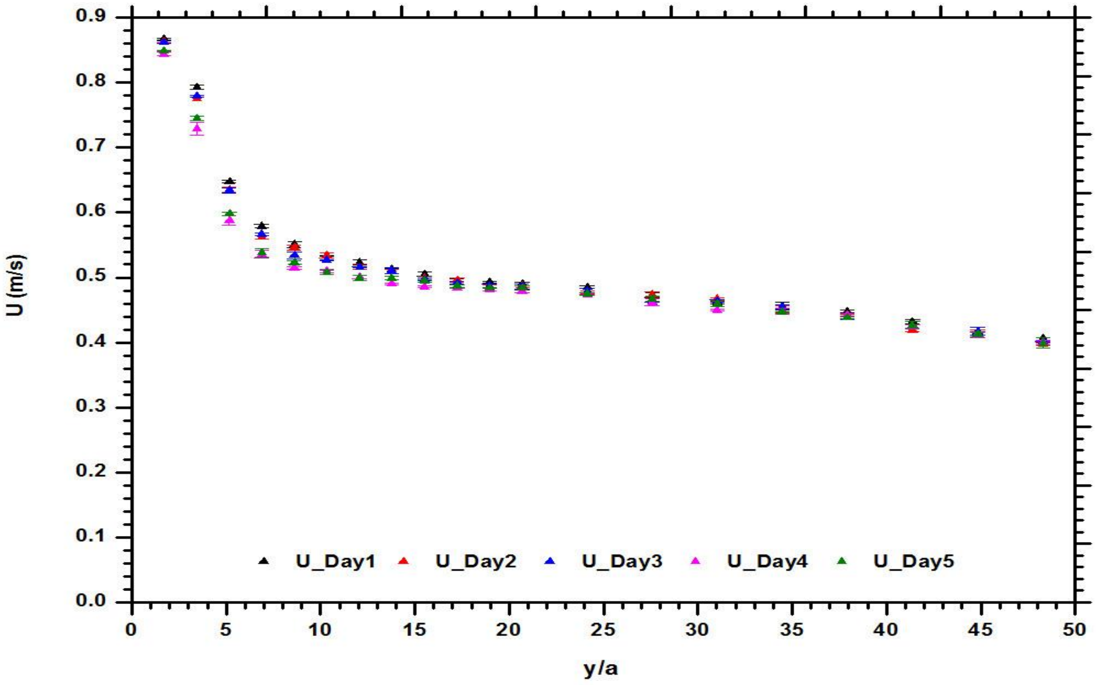

Fig. 6. Streamwise mean velocity U at the center of the right channel along the Y direction [30]

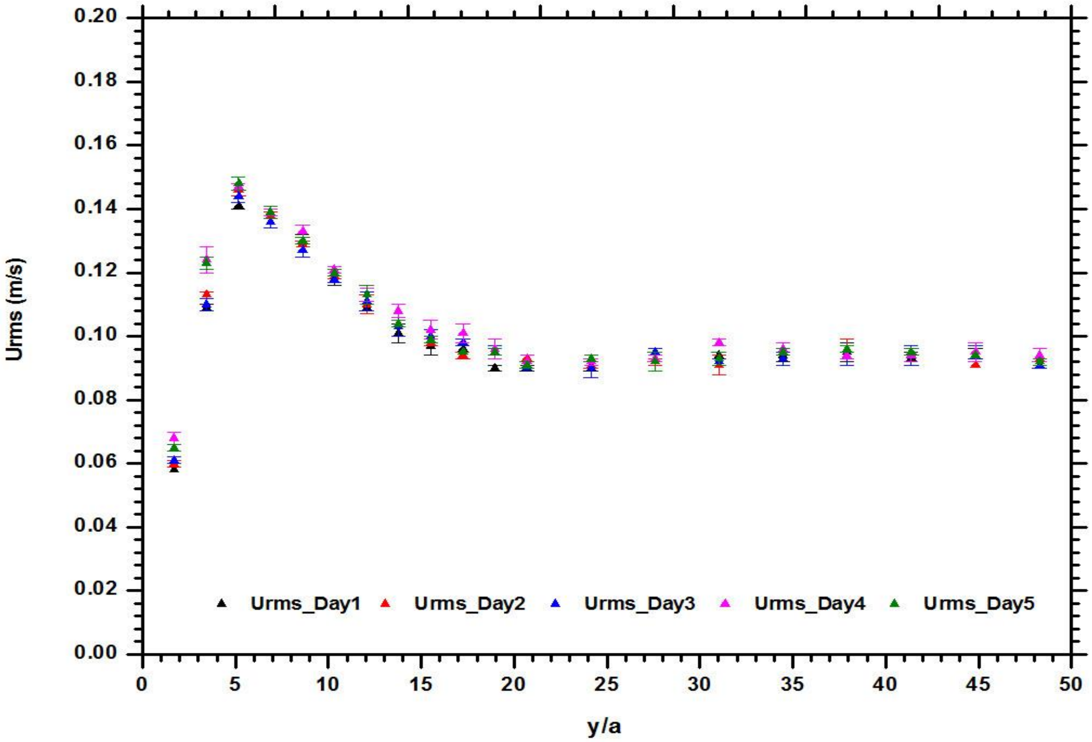

Fig. 7. Streamwise fluctuating velocity at the center of the right channel along the Y direction [30]

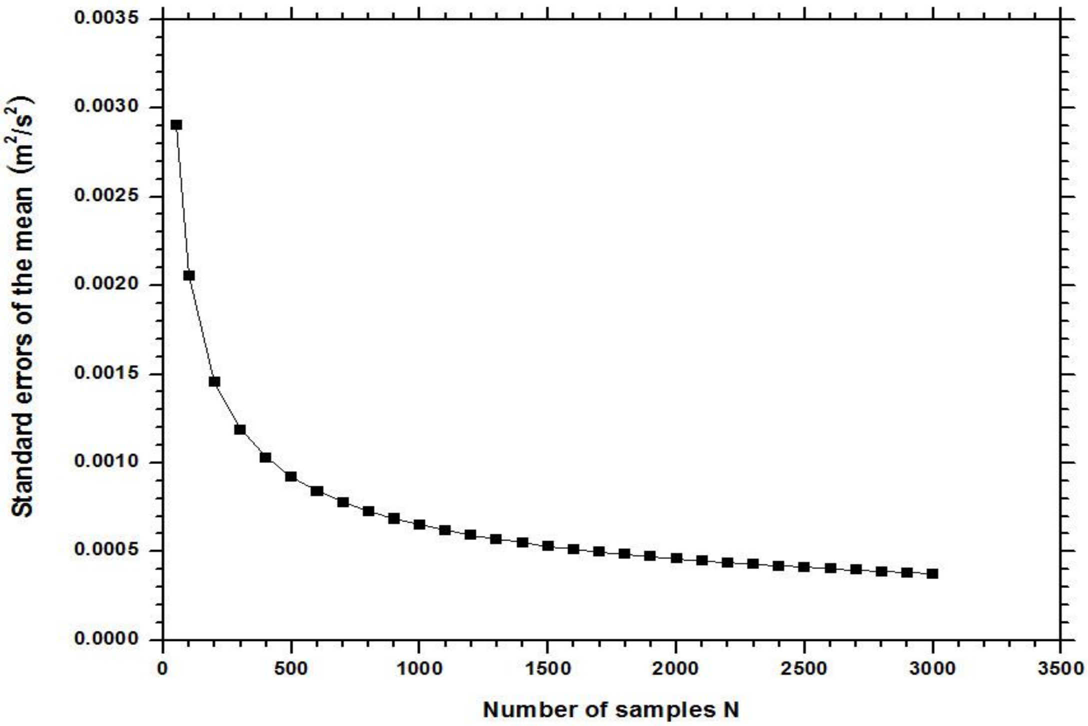

Fig. 8. An evaluation of the sampling uncertainty in the measurement of the Reynolds stress component $\overline{U'V'}$ at point (x/a = -0.86, y/a = 5.17) [30]

2.2 Particle image velocimetry (PIV)

2.2.1 Principle of PIV

The working principle of PIV is to utilize a laser sheet to illuminate the seeding particles twice within a short time period of Δt to obtain an image pair. The displacement of the particle traveled within Δt can be calculated by analyzing the image pair. The instantaneous velocity is determined by averaging the displacements of all particles within a small interrogation window. PIV is a non-intrusive and whole-field measuring technique, which enables one to obtain the instantaneous flow field spontaneously. Compared to the point-to-point methods, such as LDA, PIV is good for studying the coherent turbulence structures. The accuracy of PIV measurement depends on the laser power, frame rate, laser sheet thickness, post-treatment methods of the image, seeding particles and so on.

2.2.2 Experimental setup

The setup of the PIV system is shown in Fig. 9. The water flow was driven by two 0.5 horsepower pumps. The rectangular nozzle had a width of 5.8mm and length of 87.6mm. The spacing ratio S was 17.8mm. The height of the slots was 279.4 mm, which was long enough to ensure that the turbulent flow was fully developed. The flow passed a stagnation box before entering the channels to dampen the undesired fluctuations in the flow. The exit Reynolds number was 9,100 based on the average discharge velocity, which was 0.75 m/s. The acrylic tank had a capacity of 0.76 m^3. The flow rate was controlled by two values and monitored using two GPI TM100 flow meters with an accuracy of 97% and repeatability of 95%. The channels were located at the center of the tank as illustrated in Fig. 10 with detailed dimensions presented. The jets could develop freely without being disturbed by the walls. The two jets had the same discharge velocity and were at room temperature.

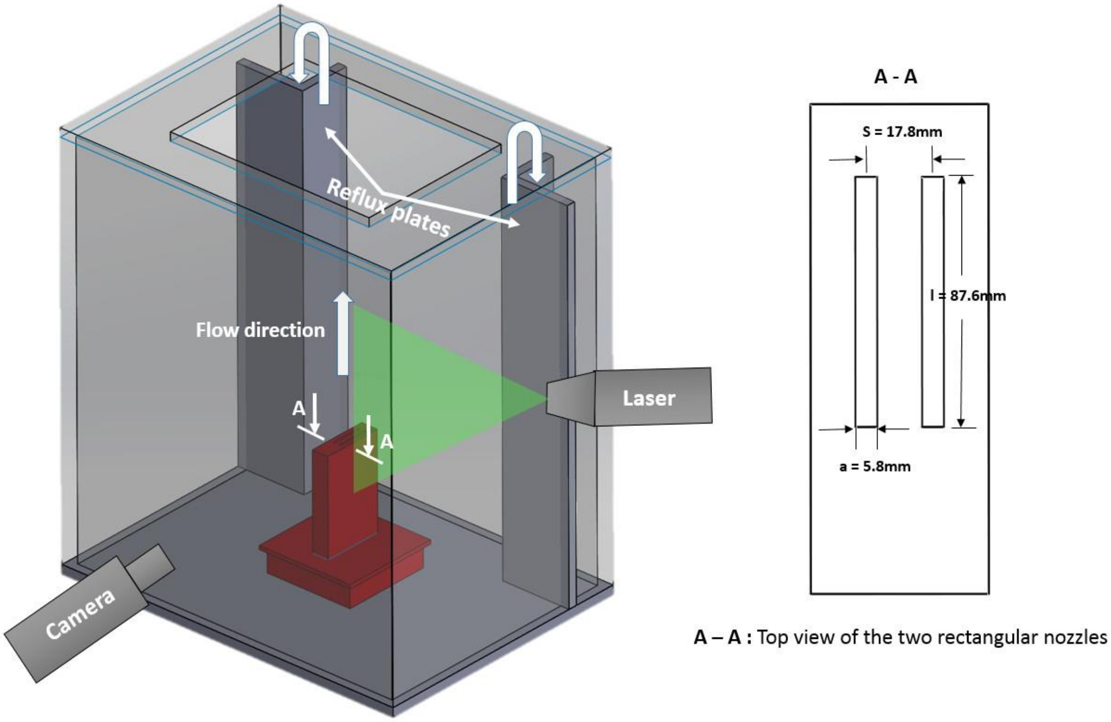

Fig. 9. PIV setup [31]

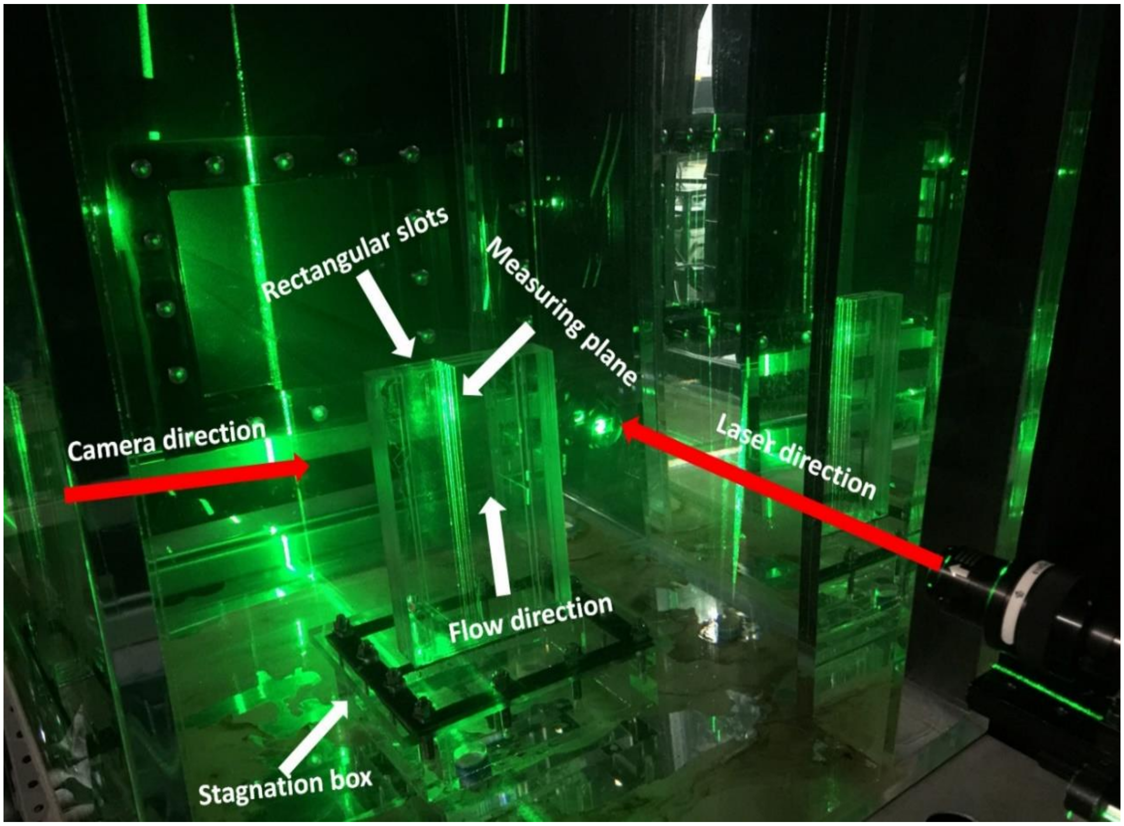

Fig. 10. Illustration of the parallel jets system [31]

The PIV system used to measure the velocity field consisted of a high-power Nd:YAG dual- head laser (Beamtech PIV200) with a wavelength of 527 nm and a high speed camera (GX3 V-190-B/W) equipped with a 1.3 Mega pixel sensor. The maximum laser energy was 100 mJ per head, and the maximum shooting frequency was 15 Hz, which was employed in this study. The maximum frame rate of the camera was 198,000 fps. 4G memories enabled a longer period of measurements with respect to a fast transport speed of the data. The maximum resolution was 1280 x 1014, which was used in this work. The high speed camera and the laser were synchronized by a high accuracy pulse generator. The time period between each pair of images in this experiment was 500 μs.

The high speed camera was sitting on a 3-D traversing system from Dantec with an accuracy of 0.01 mm so that the camera could be able to move accurately to investigate different regions of the jets. The seeding particles used in this experiment were hollow glass spheres from TSI centered at 10 μm with a refractive index of 1.5. The density ranged from 1.05 g/cc to 1.15 g/cc. The Stokes number, an indication of the tracer fidelity, calculated using Eq. (1) was 0.0009 implying that the particles could follow the fluid very well [17].

$$Sk = \frac{\tau U}{L} = \frac{D_p^2 \rho_p C_c u_o}{18 \mu L} \tag{1}$$

where τ is the relaxation time of the particle, u_o is fluid velocity, L is the characteristic length of the fluid, D_p is particle diameter, ρ_p is particle density, and C_c is the slip correction factor which is equal to 1.017 for the particle with a diameter of 10 um.

The particles were injected into the system from two water reservoirs under the water tank, and the system ran long enough before the measurements were taken to minimize any unstable effects. The laser was operated at the pulse mode with a frequency of 15 Hz. The full 4 Gb memory was used for each measurement generating about 812 pairs of images. Two measuring scales were employed to study the mixing condition in and above the converging region. The camera was moved closer to the target area after completing the measurements of the two regions together. These two cross-validated data sets helped reveal the uncertainties introduced by the enlargement factor, which was a common uncertainty that existed in any PIV measurements [18]. The images were then analyzed using an open-source code PIVlab V. 1.2. Pre-processing techniques of contrast limited adaptive histogram equalization (CLAHE) and a high-pass filter were employed to enhance the quality of the raw images [19]. A comparison of original raw image and the enhanced one is shown in Fig. 11.

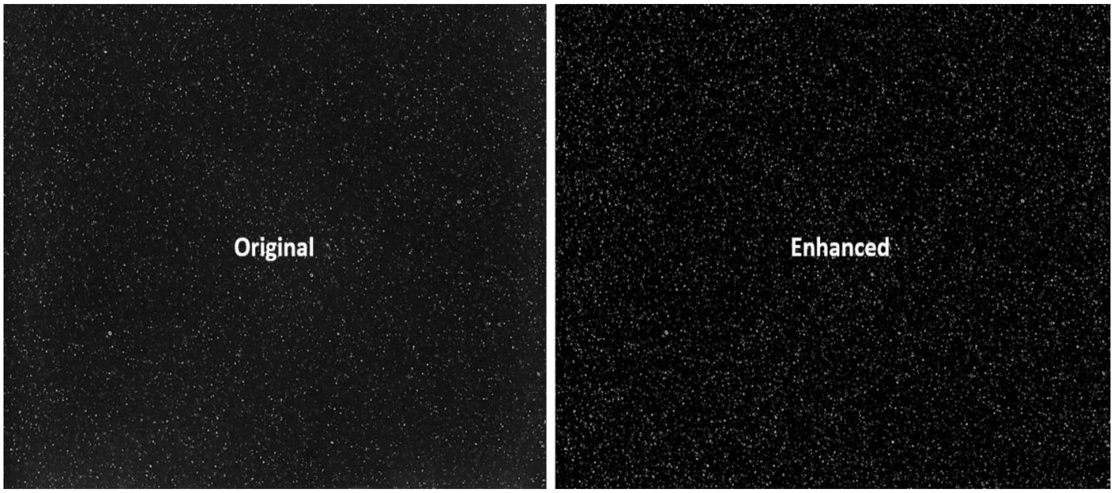

Fig. 11. A comparison of original raw image and the one enhanced by pre-processing techniques of CLAHE and a high-pass filter [31]

3. POST ANALYSIS METHODS[*]

3.1 Fast Fourier transform (FFT)

FFT is a faster way to calculate the discrete Fourier transform (DFT) of a sequence or signal. It transforms a discrete signal X in the time or space domain into the frequency domain representation. The mathematic expression is defined as:

$$X\ (n) = \frac{1}{N}\sum_{k=0}^{N-1} x(k) e^{-jk2\pi n/N} \ \ for\ n = 0,1,2 \ldots N-1 \tag{2}$$

FFT is useful for exploring the dominant phenomenon or frequencies of any eddies in the flow by decomposing a complex velocity signal into simpler segments.

3.2 Power spectral density (PSD)

Power spectral density (PSD) is a tool widely used to investigate the turbulent kinetic energy distribution as a function of frequency or wavenumber depending on the type of the signal. By mapping the energy distribution of a given signal into a Fourier-space domain, the energy cascade process can be better examined and understood. By definition, PSD is the Fourier integral transform of the autocorrelation *R(τ)* of a given signal. For a real and stationary signal *s(t),* the PSD function *P(f)* can be described as follows:

---

[*] Reprinted with permission from "Laser-Doppler Measurements of the Turbulent Mixing of Two Rectangular Water Jets Impinging on a Stationary Pool" by Wang, H., et al., 2016. International Journal of Heat and Mass Transfer, Vol. 92, 206-227, Copyright [2016] by Elsevier.

$$P(f) = \int_{-\infty}^{\infty} R(\tau) e^{-2\pi i f \tau} \, d\tau \tag{3}$$

where f is the frequency, τ is the time shift, $i = \sqrt{-1}$, $R(\tau) = E[s(t+\tau)s(t)]$, and E is the expected value.

3.3 Continuous wavelet transform

In 1981, Morlet introduced wavelet transform to study seismic signals [20]. Farge [21] reviewed its application to turbulence in 1992. Compared to Fourier analysis in which the local information is lost after the signal is transformed into Fourier domain, wavelet analysis is able to analyze the signal in the scale or frequency and time domain while providing a history of the signal's evolution. Turbulence happens at different scales, so decomposing the turbulent flows into local scales is beneficial to further understand the turbulence process. Although short-time Fourier transform provides some time information, the size of the time window to examine the signal is fixed which is not always useful. In contrast, wavelet analysis is capable of analyzing the signal with a flexibly sized time window. By definition, continuous wavelet transform (CWT) is the convolution of a given signal *s(t)* with a family of wavelet functions as represented mathematically by Eq. (4):

$$W(b,a) = \frac{1}{\sqrt{a}} \int_{-\infty}^{\infty} s(t) \psi^{*} \left(\frac{t-b}{a}\right) dt \tag{4}$$

where W is the wavelet coefficient; a is the wavelet scale; b is the position (time or space); the asterisk stands for the conjugated value; ψ is the mother wavelet function.

The wavelet function can be elongated and shifted by altering the scale *a* and the analyzing position *t*, respectively. For a better understanding of wavelet transform, an interpretation of its physical meaning is necessary. In mathematics, convolution is an evaluation of how close two functions are. Thus, the physical meaning of the wavelet coefficient W is the degree of similarity between signal *s(t)* and the wavelet function. By changing the parameters of *a* and *b*, the whole signal can be inspected at varied scales and positions in time or space. That is why many researchers describe the wavelet transform as a mathematical microscope. The resulting wavelet coefficients *W(b, a)* indicate the average differences between two neighboring segments of the signal, which is another important interpretation of the physical meaning of the wavelet coefficients. CWT means the transforms are continuous in the scale and time domain.

Farge [21] reviewed some basic requirements for the selection of a proper wavelet function, such as the admissibility condition. Two widely used wavelets, the Mexican hat wavelet and the Morlet wavelet, were compared by Christopher and Compo [22]. They found that the real-valued Mexican hat is broader in the scale domain but narrower in the time domain compared to the complex-valued Morlet wavelet. The authors [22] also stated that a complex wavelet such as the Morlet was suitable for identifying the oscillations in the signal; whereas, real wavelet such as Mexican hat was better for detecting discontinuities. A signal S with random noises was chosen to demonstrate the differences between these two wavelets. This signal S is described in Eq. (5):

$$S = sin\,(2\pi * 10t) + sin\,(2\pi * 20t) + sin\,(2\pi * 50t) + random\ noises \qquad (5)$$

This signal clearly contains the frequencies of 10 Hz, 20 Hz, and 50 Hz. Fig. 12 presents the wavelet transform results using these two wavelet. The colors in the figure indicate the magnitude of the wavelet coefficients: The magnitude decreases from red to blue. The Morlet wavelet clearly identifies 10 Hz, 20 Hz, and 50 Hz as the three dominant frequencies, while the peaks obtained from Mexican hat overlap in the scale space and are not distinguishable. Thus, the Morlet wavelet was selected for this study.

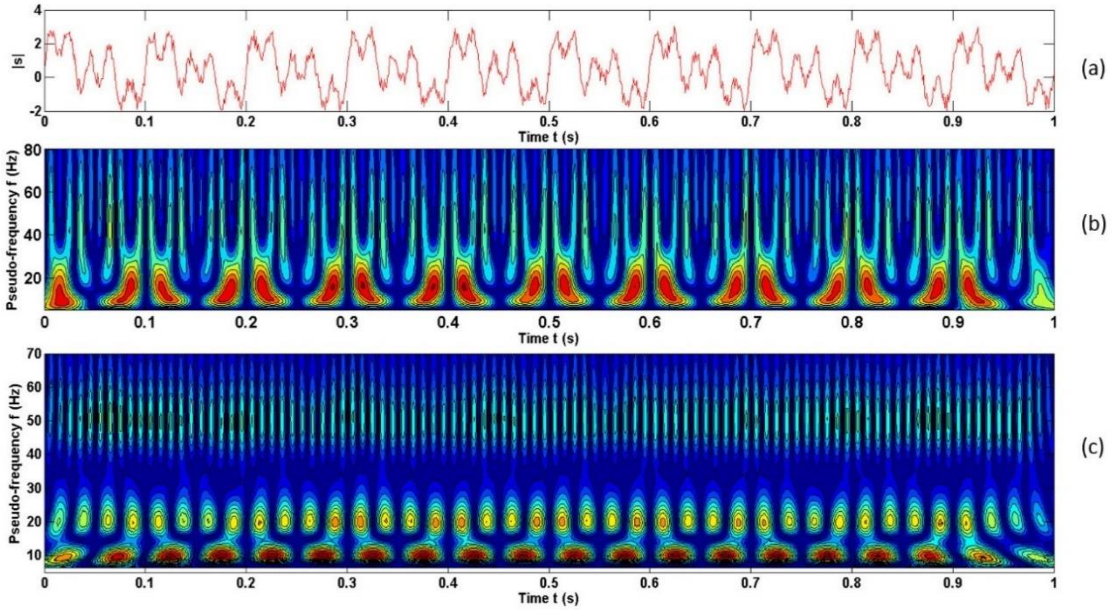

Fig. 12. Comparison of wavelet transform results of signal S shown in (a) using Mexican hat wavelet (b) and Morlet wavelet (c) [30]

4. RESULTS AND DISCUSSION*

4.1 LDA results

All results presented in this work are based on the point by point measurements. Thus, one should not assume that the distributions of any parameters presented were obtained at the same time. This factor must be considered when comparing results from this work with any CFD simulations or particle image velocimetry (PIV) data. Except for the case of imbalanced flow, the flow rate was set at 0.385 kg/s for each jet, corresponding to an exit velocity of 0.75 m/s on average. The Reynolds number at the exit based on the dimensions of the channel was about 9100. The temperature of the water (tap water) was about 23 ℃. The temperature rise during the normal operation was less than 2 ℃, depending on the length of the experiment. All the flow parameters shown on the Y axis were normalized by the local maximum velocity U_{max}, which was different for each case while the position values on the X-axis were normalized by the channel width which was 5.8 mm. The jets were approximately issued from $-2 < x/a < -1$ and $1 < x/a < 2$.

4.1.1 Outlet condition

To verify if the flow at the outlet has reached the fully turbulent flow and the symmetry condition near the exit, measurements were performed along the Z-axis for

---

*Parts of this section are reprinted with permission from "Laser-Doppler Measurements of the Turbulent Mixing of two Rectangular Water Jets Impinging on a Stationary Pool" by Wang, H., et al., 2016. International Journal of Heat and Mass Transfer, Vol. 92, 206-227, Copyright [2016] by Elsevier.

both channels. The measuring plane was 10mm above the channel surface, which, as explained in section 2.3, was the lowest position the laser could reach. Fig. 13 shows the mean streamwise velocity distribution of the two channels. The denominator U_0 is the nominal mean discharge velocity with a value of 0.75 m/s. The error bars are the standard deviations of five independent sets of data. The deviations are less than 1%, which indicates a good repeatability of LDA measurements in this work. Obviously, the flows are not symmetrical along the Z-axis in the two channels. This may be attributable to the influence from the small mixing boxes located at the bottoms of the channels. The inlets to the mixing boxes are not at the center, which creates uneven flows. However, the velocity profiles clearly show that the flows, which are 10 mm above the exits, are fully turbulent for both channels. Another important parameter of the initial outlet conditions is the turbulence intensity which plays an important role in determining the mixing characteristics of the twin jets. The average streamwise turbulence intensity at 10 mm above the outlet was 11.5%. The distribution of the Reynolds stress component is plotted in Fig. 14. The error bars represent the standard deviation of five independent measurements. The Y-axis is normalized by the nominal mean discharge velocity U_0. The shape of the Reynolds stress component is relatively flat except in the regions near the walls of the channels.

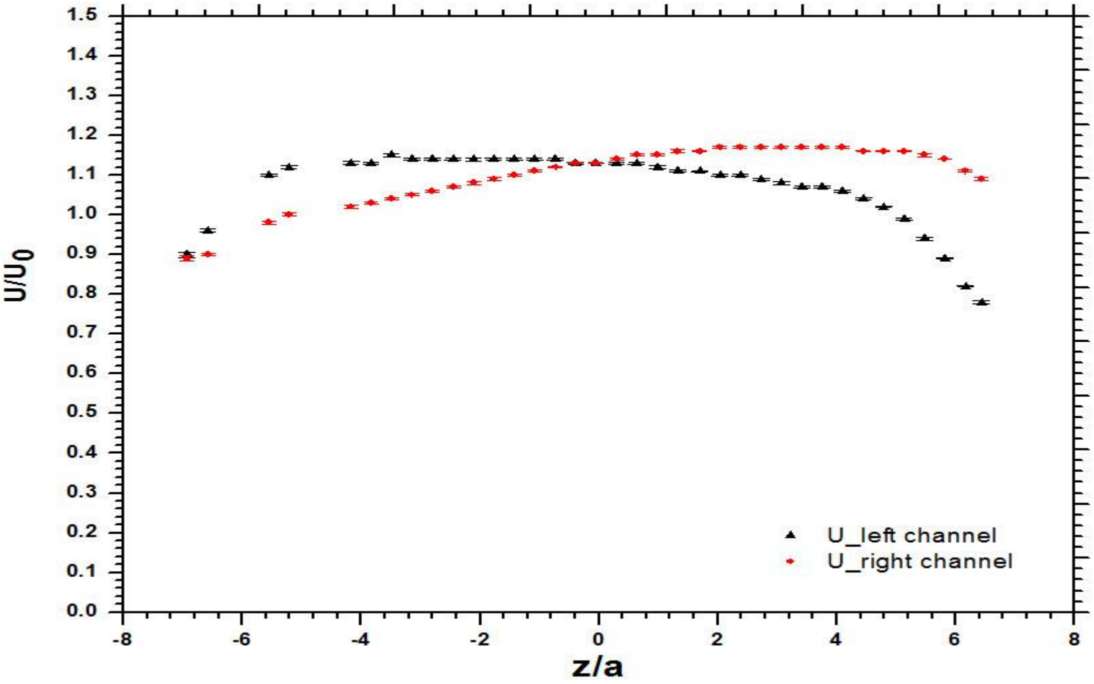

Fig. 13. Mean streamwise velocity distributions near the exits of the two channels along the Z direction. The measuring locations were 10 mm above the exits. U_0 is the nominal mean discharge velocity with a value of 0.75 m/s. [30]

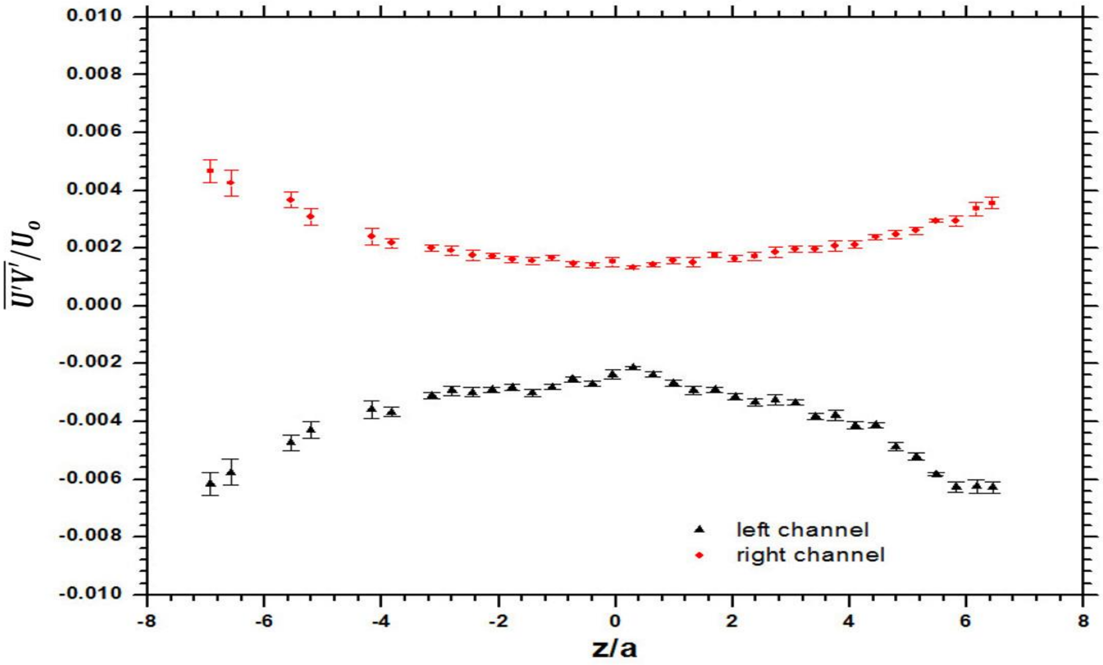

Fig. 14. Reynolds stress component distribution at 10 mm above the outlets. The error bars represent the standard deviations of five independent measurements. [30]

4.1.2 Twin jets with equal discharge velocity

4.1.2.1 Mean velocity distributions

The spatial flow field was scanned by LDA from *y/a* = 1.72 to 48.28 in the streamwise direction. Fig. 15a presents the distribution s of the mean streamwise velocity *U*. The triangles represent the measured points, while the remaining parts of the contour were obtained by extrapolations from the experimental data. A recirculating zone clearly exists in the combining region in which some of the velocities are negative. In order to compare these results with the ones from other works, specific numbers of *U* at each locations and a zoom-in view of the combining region are plotted in Fig. 15b. The streamwise velocity *U* is normalized by U_{max} which has a value of 0.882 m/s. The combination of the jets happened at around *y/a* = 15.52, where *U* on the symmetry plane reaches its maximum. The combination may happen earlier than this because no measurements were taken in the region between *y/a* = 13.79 and *y/a* = 15.52. This result is close to the PIV result in [23] which is *y/a* = 15. MP is the location where the streamwise mean velocity *U* is zero. Fig. 15b shows that MP falls into the region between *y/a* = 1.72 and *y/a* = 3.45, which is smaller than 5.8 found in [23]. The mixing of the twin jets happens in the merging region between the MP and CP. The length of the merging region depending on the relative location of MP and CP and is an important parameter in order to understand the mixing of the twin jets. Only few studies use small nozzle spacing ratios comparable to those in the present work, such as 2.5 [8] and 4.25 [10]. For 2.5, the authors reported values of 1.5 for MP and 10.5 for CP with an aspect ratio of 5.6 [8]. Considering the fact that spacing ratio *S/a* is 3.1 and the aspect ratios 15.1 in the present work, these results look similar in some sense because a smaller *S/a* will reduce the length of the merging region. As for the results reported in [10], the authors found that MP was at *y/a* = 4 and CP was at *y/a* = 8, which are also comparable to the results in this work. Based on these comparisons, we can confirm that the positions of MP and CP are greatly influenced by *S/a* and the aspect ratio *l/a*, where *l* is the length of the channel as shown in Fig. 4.

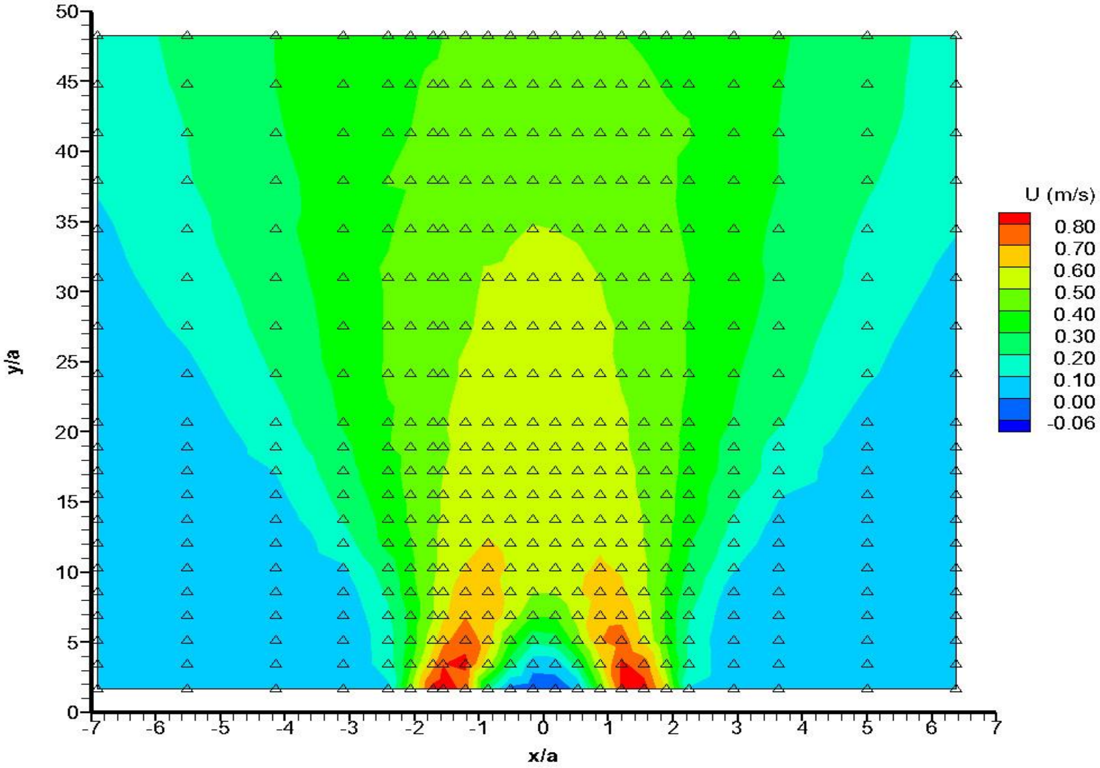

Fig. 15a. Mean streamwise velocity distributions (contour view) [30]

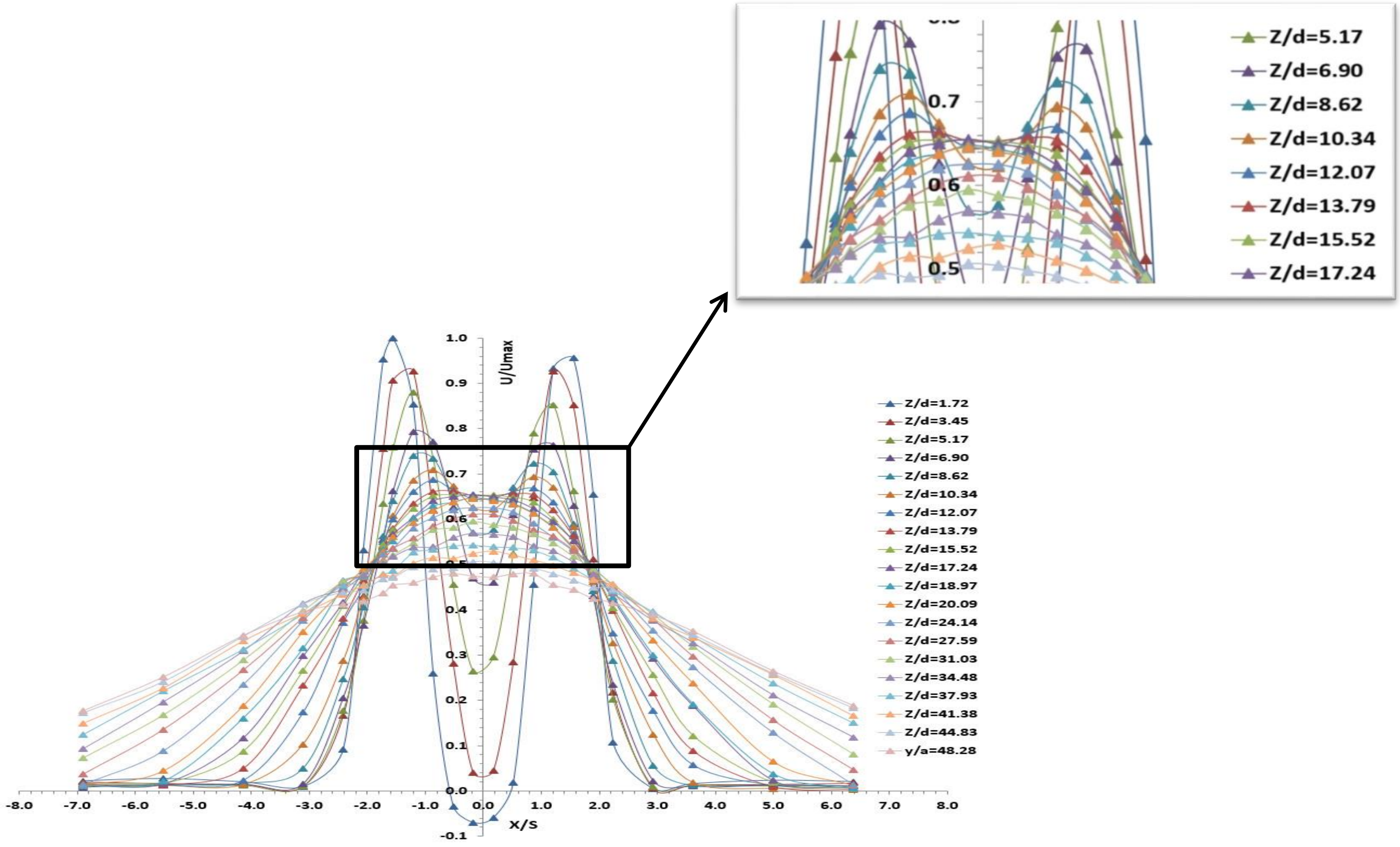

Fig. 15b. Mean streamwise velocity distributions (line plots with zoom-in view) [30]

4.1.2.2 Turbulence intensity distributions

Streamwise and lateral turbulence intensities are presented in Figs.16a and b, respectively. The turbulence intensities were normalized by the local maximum streamwise velocity among all the data U_{max} which had a value of 0.882 m/s. High symmetry was observed along the center plane with stronger streamwise turbulence intensities found near the edges of the jet shear layers. The streamwise turbulence level was much lower in the recirculation zone than in the lateral component in that region. The flow presented self-preserving characteristics beyond CP for both components. The high turbulence levels mainly came from the interactions between the combined jets and the static surroundings. The turbulence intensities in the outer region were then proportional to the entrainment rate of the surrounding fluids due to the movements of the twin jets. A sudden jump in the turbulence intensity occurred in the center area, from 1.72 to 3.45, indicating strong merging activity.

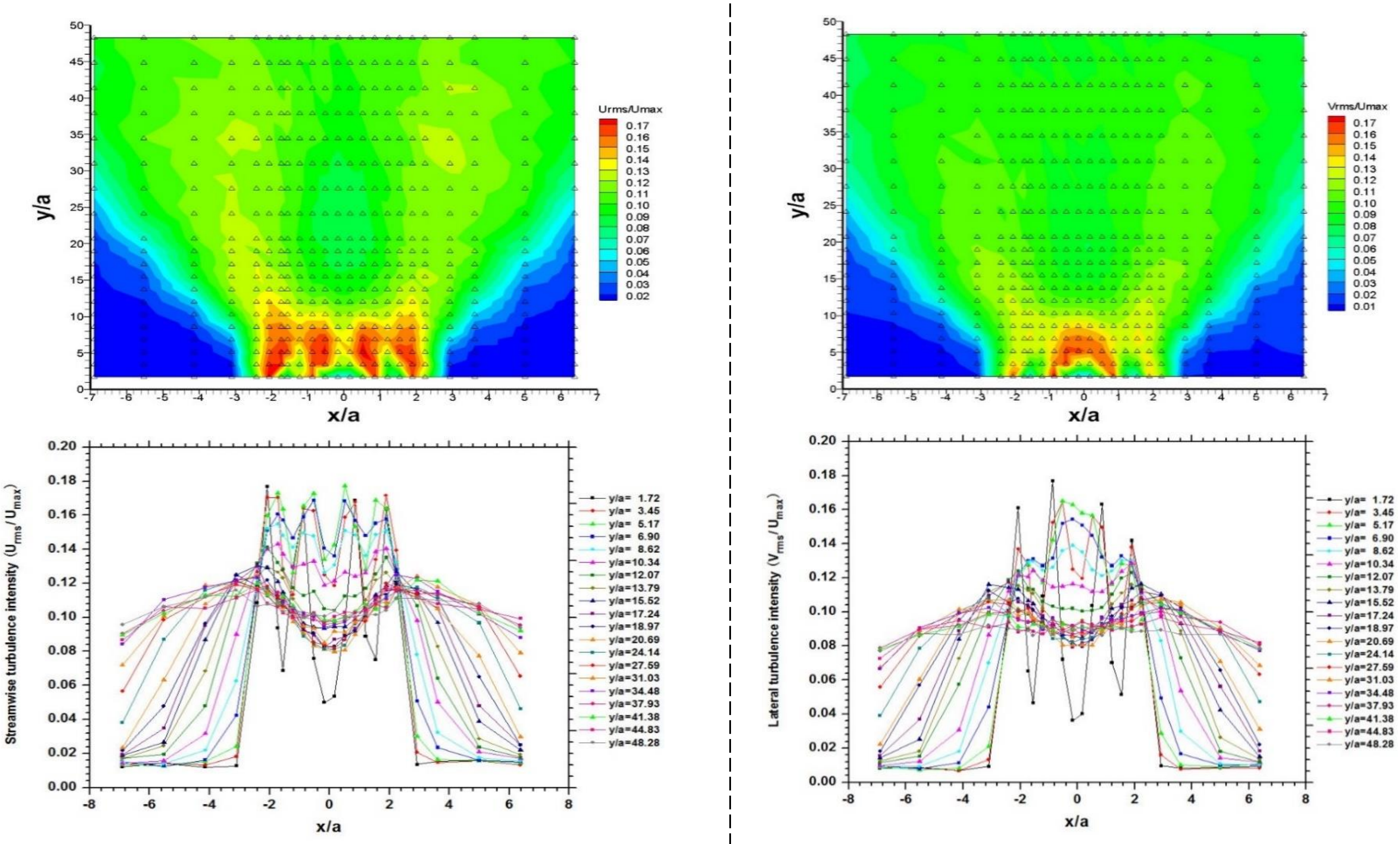

(a) (b)

Fig. 16. Turbulence intensity distributions: (a) streamwise and (b) lateral [30]

4.1.2.3 The Reynolds stress component distributions

Fig. 17 shows the distribution of the Reynolds stress component. Reynolds stress represents the momentum flux transfer in the flows. Momentum flux decreases rapidly from *y/a* = 3.45 to 12.07, indicating that most momentum transfers occur between the inner shear layers of the two jets in the merging region. The two peaks imply strong interactions between the jets. After the jets combine, momentum transfers mainly exist in the outer shear layers where the velocity gradients are large. The maximum value of the Reynolds stress component appear at the position of *y/a* = 5.17, where the two jets start to combine. The self-preserving behavior is only observed in the core region after *y/a* = 12.07.

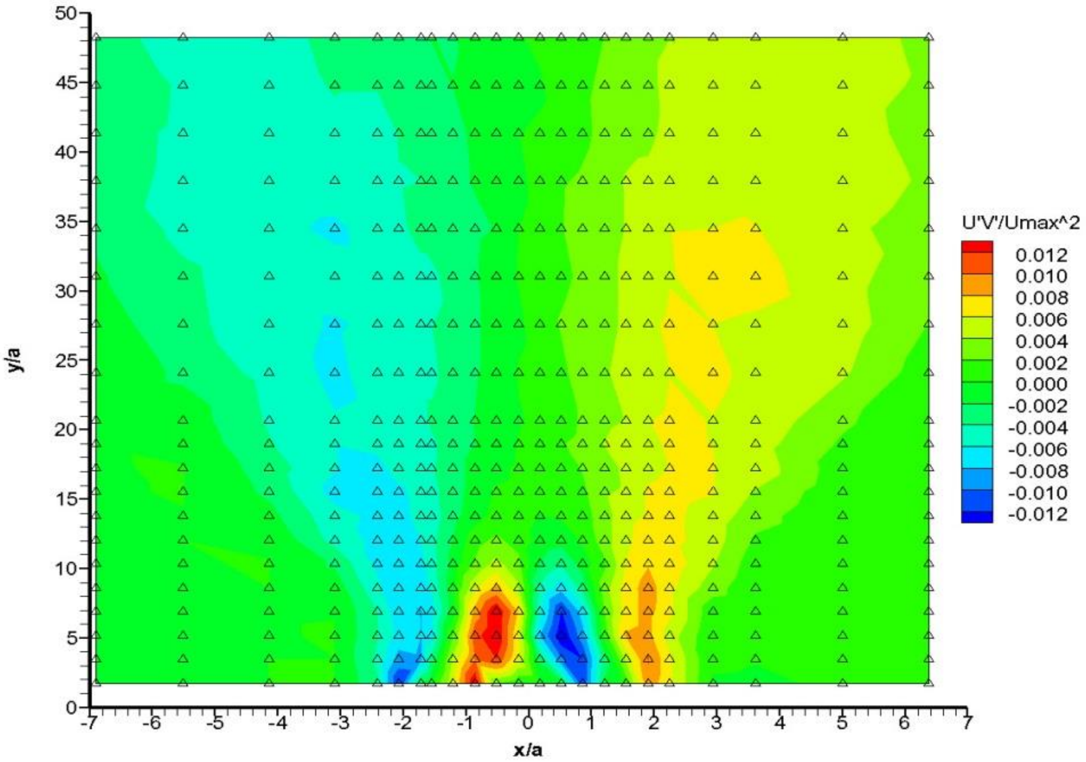

(a)

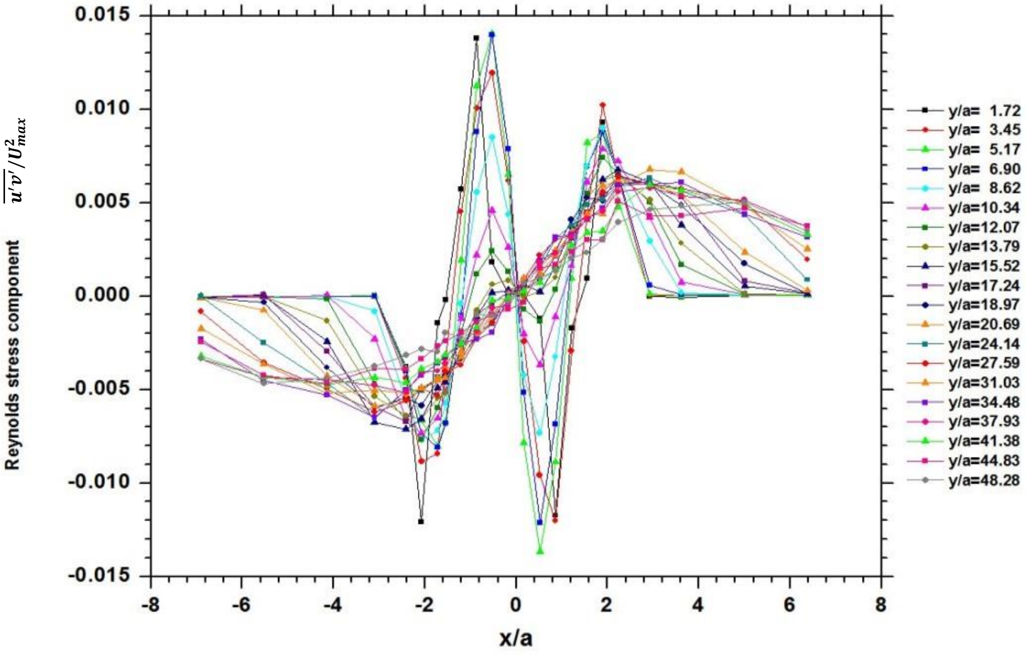

(b)

Fig. 17. Reynolds stress distributions: (a) contour view and (b) line-plot view [30]

4.1.2.4 Z-component vorticity

Vorticity represents the local rotation speed of a fluid particle. It can be calculated mathematically by Eq. (6). For a two dimensional flow, vorticity is perpendicular to the X-Y plane, and the Z-component vorticity can be expressed by Eq. (7). To maintain the freedom of the jets and avoid influence from the wall of the water tank, the length of the rectangular channel used in this work is limited. With an aspect ratio of 15.1, studying the vorticity distribution in the X-Y plane of this twin jets flow is still useful to help understand the fluid particles' behaviors.

$$\vec{\omega} = \vec{\nabla} \times \vec{u} = \begin{vmatrix} \vec{e}_x & \vec{e}_y & \vec{e}_z \\ \frac{\partial}{\partial x} & \frac{\partial}{\partial y} & \frac{\partial}{\partial z} \\ u_x & u_y & u_z \end{vmatrix} \tag{6}$$

$$\vec{\omega} = (\frac{\partial u_y}{\partial x} - \frac{\partial u_x}{\partial y})\vec{e}_z \tag{7}$$

where $\vec{\omega}$ is the Z-component vorticity, u_x, u_y and u_z are the three components of the velocity $\vec{u}$.

The Z-component vorticity distributions and the velocity vector field are presented in Fig. 18. Due to the attraction of the two jets and the entrainment of the surrounding fluid, fluid particles in the inner and outer region of the jets rotated in opposite directions. Fig. 18b indicates that the vorticity peaks around the jet outlet region are moving towards the center point of the two jets. No strong vorticities were observed after y/a = 12.07, and the self-preserving phenomenon is presented in those far field. As for the magnitude, rotation speed was faster in the inner region of the two jets as a result of the interactions between them. The vector field shown in Fig. 18a clearly reveals that significant entrainment of the surrounding fluid existed in the region between y/a = 1.72 and y/a = 17.24. In the negative pressure region, the flow mainly moved downward. The flow did not move completely straight in the far region, although ideally it should. This may be attributable to the slight imbalance in the outlet flow. The flow rate is controlled by two ball valves and so the two discharge flow rates cannot be exactly the same due to mechanical constraints. However, as discussed in section 3, the maximum velocity shift is only 0.66%, which is negligible.

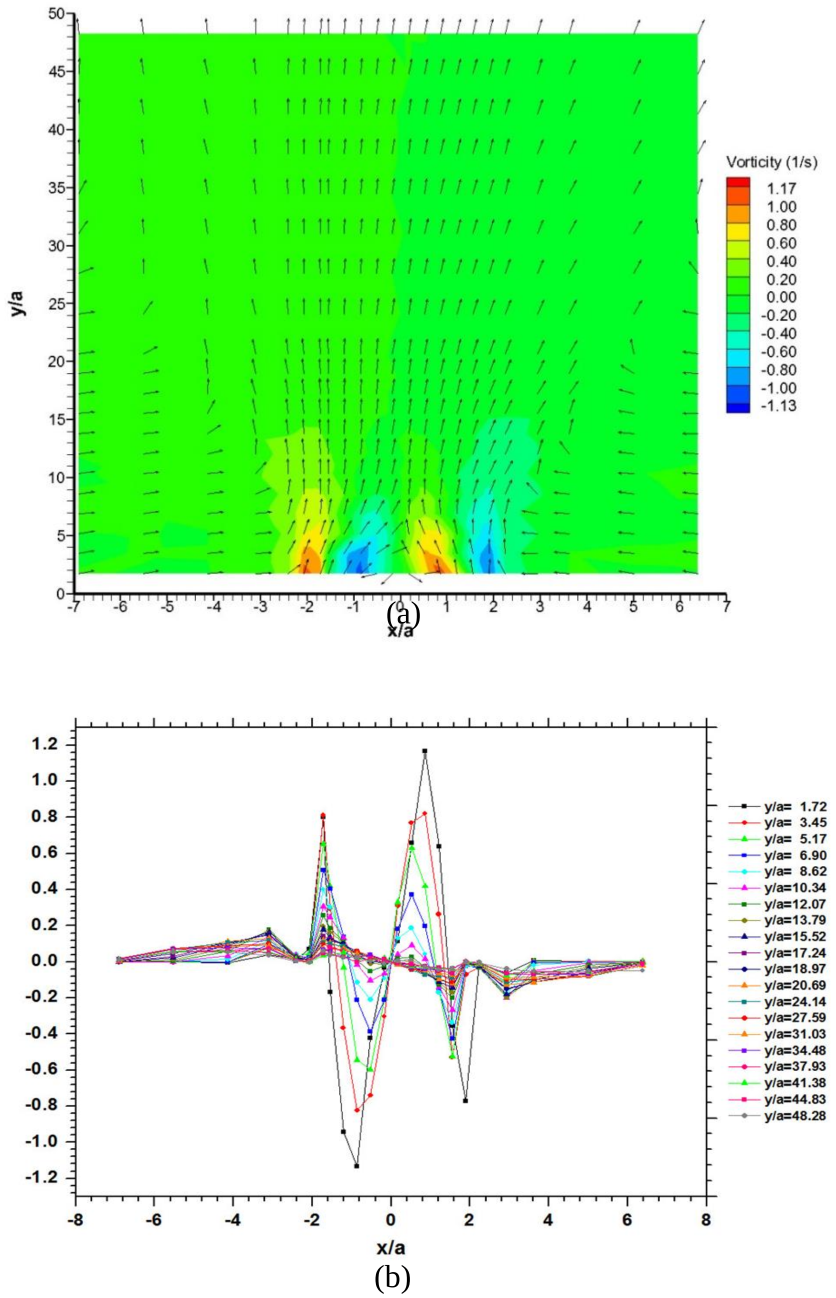

Fig. 18. Z-component vorticity distributions: (a) contour view and (b) line-plot view. The velocity vectors shown in (a) have uniform length to demonstrate the flow direction only; the positive Z direction is pointing out of the paper [30].

4.1.3 Effect of the flow imbalance on the middle plane

In practical engineering applications, the jet discharge velocities may not be the same, e.g., the coolant flows passing through the reactor core and mixing in the lower plenum in high temperature gas-cooled or liquid-cooled nuclear reactors. The flow imbalance or the velocity ratio has a significant impact on the mixing condition and changes the locations of the MP and CP. In order to focus on the core region or the mixing region, the measurements employed a 0.5 mm resolution instead of 1 mm. This doubled resolution ensured better measurements of the flow behaviors in the imbalanced condition. The locations of the jets were kept the same, $-2 < x/a < -1$ and $1 < x/a < 2$. The measured plane was P2 as shown in Fig. 5. In the vertical direction (Y direction), the measurements were performed from $y/a = 1.72$ to 20.69. The right jet discharge velocity was kept the same while the left one was changed to generate velocity ratios of 1.3, 1.5, and 1.9. The velocity ratio R is defined as $R = U_{left}/U_{right}$ in which the U_{left} and U_{right} are the average discharge velocities of the left jet and right jet, respectively. All the results presented in Fig. 19a and Fig. 19b were normalized by the maximum velocity at each velocity ratio. For all three velocity ratios, the velocities reached their maxima at y/a = 1.72. The detailed experimental conditions are summarized in Table 2.

Table 2. Summary of the experimental conditions for the imbalanced jets [30]

R	U_{left} (m/s)	U_{right} (m/s)	U_{max}^{*} (m/s)
1.3	0.988	0.760	1.144
1.5	1.140	0.760	1.295
1.9	1.444	0.760	1.632

* The maximum velocities are all located at y/a = 1.72 for each velocity ratio.

Self-preserving phenomenon is observed for the mean streamwise velocities at positions higher than $y/a = 10.34$ in the three cases. The normalized mean streamwise velocities present a similar distribution in the imbalanced condition as shown in Fig. 19b. The independence of the Reynolds number for the jet flows could be the main reason for this phenomenon. A significant difference in U among the three cases is the change in the relative position of the black ($y/a = 1.72$) and red lines ($y/a = 3.45$) shown in Fig. 19a (left). The streamwise velocity at $y/a = 3.45$ is more negative than that at $y/a = 1.72$, when R is larger. This can be explained by the fact that a larger velocity ratio will generate a larger shear force, which further increases the negativity of the pressure in the recirculation region. The negative pressure has its largest influence on the velocity profile in the mixing region ($1.72 < y/a < 3.45$). As for the turbulent intensity distributions, no self-preserving behavior was found for any velocity ratio. This is in accordance with the results shown in Fig. 16 and is because the two jets have not combined into one single jet yet in that region and thus, merging activity still exists. In addition, by comparing the patterns for the different R shown in Fig. 19b, one can find that the area with high turbulent intensity is larger with an increased R. Similar to what is found in the velocity distribution, the relative values of the turbulence intensities at the locations of $y/a = 1.72$ and $y/a = 3.45$ change as a function of R.

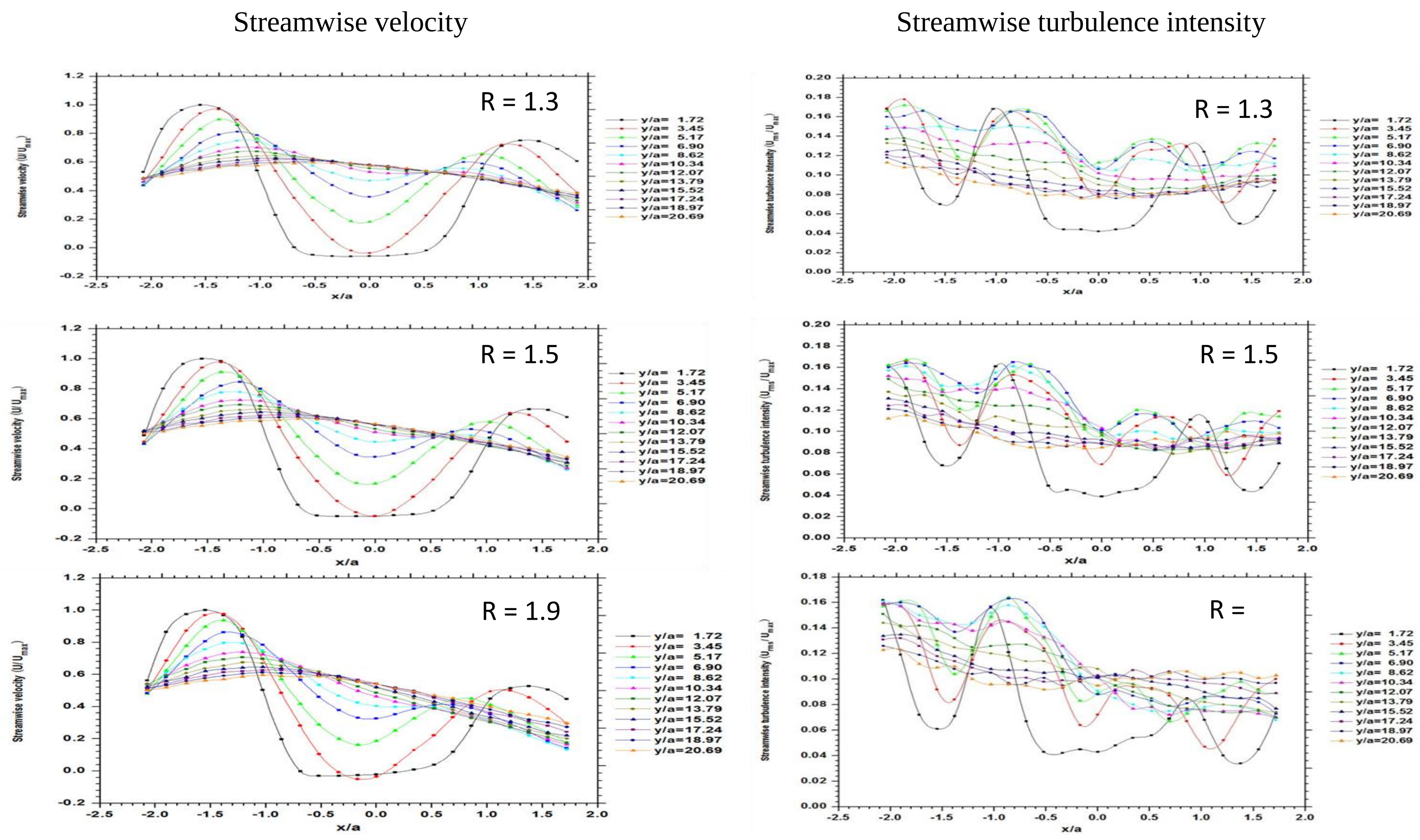

Fig. 19a. Streamwise velocity (left) and turbulence intensity distribution (right) of imbalanced jets (plot view) [30]

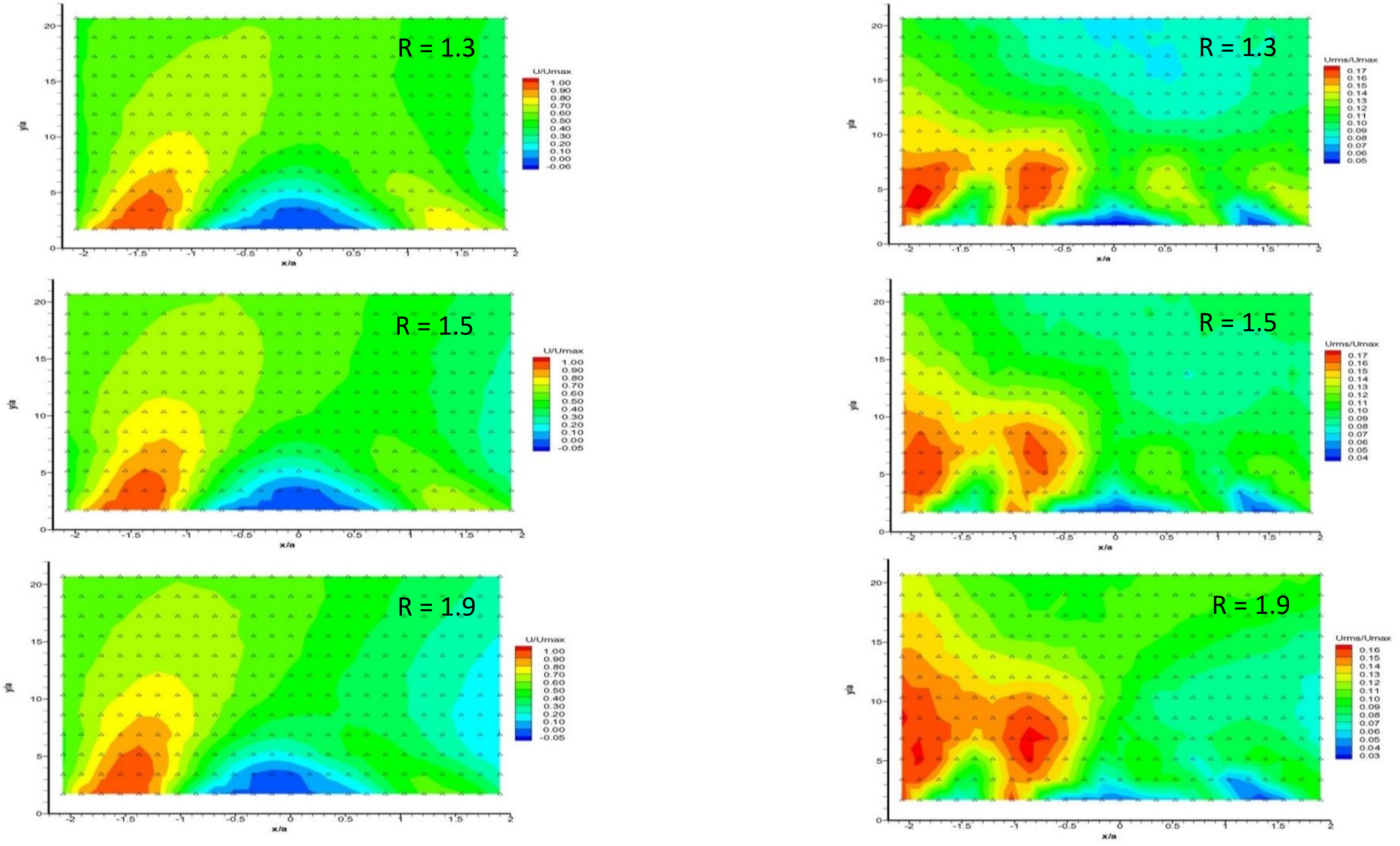

Fig. 19b. Streamwise velocity (left) and turbulence intensity distribution (right) of imbalanced jets (contour view) [30]

4.1.4 Comparison of a single jet with the combined twin jets

Literature reviews indicate that the combined twin jets will behave as a single jet [e.g., 1, 2, 6], and theories derived based on the single jet system should apply to the twin jets in the combined region. To verify this statement and check if the results in this work are valid, a comparison between the experimental results of twin jets from this work and the analytical solutions for single jet is shown in Fig. 20. The parameter used for comparison was U, and two well-known analytical solutions from Goertler and Tollmiern [24] for single jets are chosen. The experimental data match the analytical solutions well. Goertler's solution is slightly closer to the experimental data in the core flow region than in the outer shear layer region.

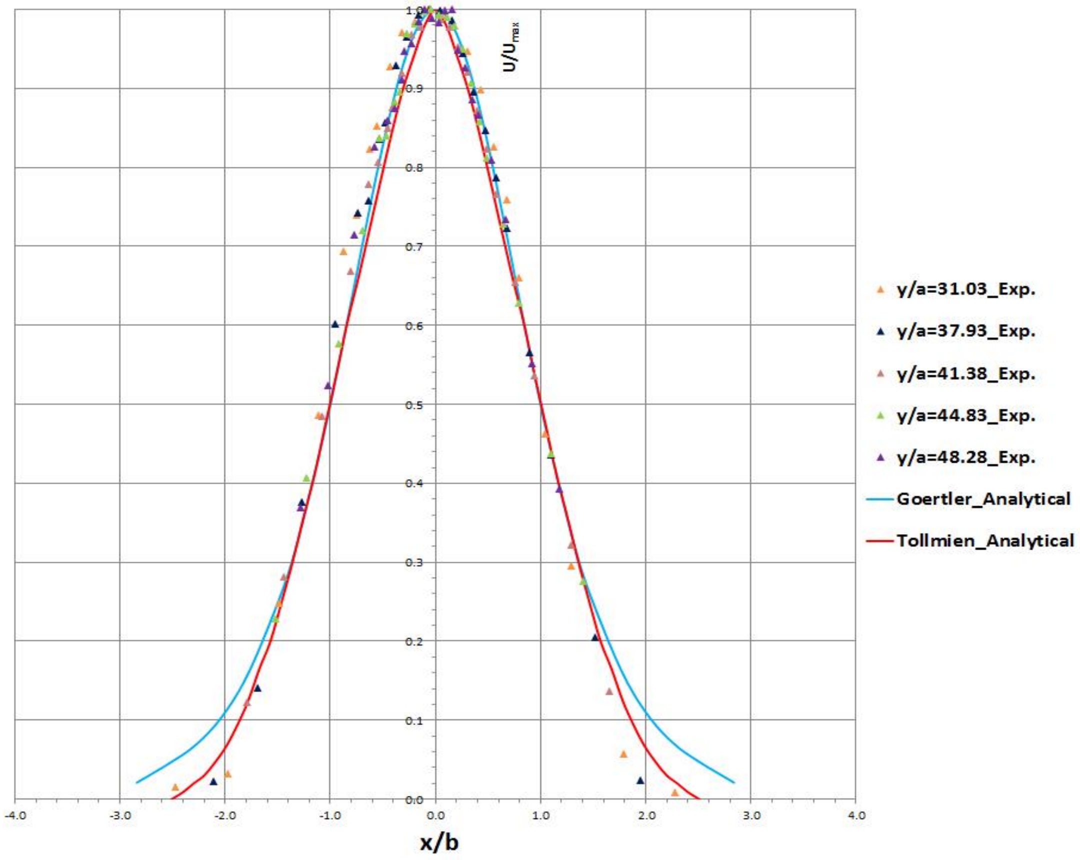

Fig. 20. Comparison of the analytical solutions of a single jet with our experimental results for the combined twin jets. *b* is the half width of the jet where U/U_{max} = 0.5 [30].

4.1.5 Results of the spectral analysis

LDA is an ideal tool to measure the fluctuation velocities in turbulent flows because it is a non-intrusive measuring technique with the ability to generate high spatiotemporal resolution data. LDA measurements rely on light reflection from random-arrival particles passing through the measuring volume. Many widely used spectral analysis methods such as fast Fourier transform (FFT) require the data to be equally spaced in time. Thus, the individual realization LDA data with velocity data irregularly spaced in time need to be reconstructed to meet the requirement. However, many other techniques for estimating the turbulent velocity spectra exist, such as the slotting technique [25] in which the data are not necessarily equidistant in time. Three well-known and simple reconstruction algorithms to evenly resample the data in the time domain are linear interpolation, the hold and shoot algorithm and nearest-neighbor interpolation. Eq. (8) defines the linear interpolation as follows [26]:

$$U_r = \frac{(t - t_n)U(t_{n+1}) + (t_{n+1} - t)U(t_n)}{t_{n+1} - t_n}, t_n < t \leq t_{n+1} \tag{8}$$

where *U* is the velocity, and *t* is the time index. The hold and shoot or zero-order hold algorithm generates the signal with equal time step by holding the most recent sample value for one unit time interval until the next sample arrives. Nearest-neighbor interpolation is the simplest: It just assigns the value of the nearest sampling point to the current position and the errors are obvious. Thus, the first two methods are more widely employed in the post treatment of LDA data. Hertwig et al. [27] processed discontinuous LDA data using the hold and shoot algorithm and successfully applied proper orthogonal decomposition and continuous wavelet transform to the study of turbulent flow. Ramond and Millan [26] compared the power spectral density estimations computed from the linear interpolation and the hold and shoot techniques. It was found that results from linear interpolation were closer to the results measured by HWA.

In order to verify if the reconstructed data computed from linear interpolation can represent the original velocity signal, a portion of the instantaneous streamwise velocity *U* sampled at an average frequency of 30 Hz was selected as the sample. Fig. 21 presents the original velocity signal and the reconstructed signals resampled at 100 Hz (Δt = 10 ms) and 1000 Hz (Δt = 1 ms). Nearest-neighbor interpolation results were displayed for comparison purpose. Clearly the resampling rate of 100 Hz in both Nearest-neighbor interpolation and linear interpolation failed to represent the true signal where a large gradient existed as shown in the red boxes in Fig. 21 (a). With linear interpolation, the higher resampling rate of 1000 Hz produced results almost identical to the original signal.

Linear interpolation seems perfect but may only work well for a signal sampled at a low data rate, such as at 30 Hz in the example. As mentioned previously, a data rate of 200 Hz was obtained by only measuring the u component at position *R* illustrated in Fig. 5. By applying linear interpolation to the signal sampled at 200 Hz, discrepancies were found for the RMS velocities as shown in Fig. 22. The resampling frequency was still 1000 Hz. The reconstructed signal dampens or underestimates the fluctuations of the original signal. There was no obvious reduction in the discrepancies observed when the resampling frequency was increased to 10,000 Hz. However, for the mean velocity, the two signals are almost identical as shown in Fig. 23, except in the near-wall region where *Z/a* is larger than 6.

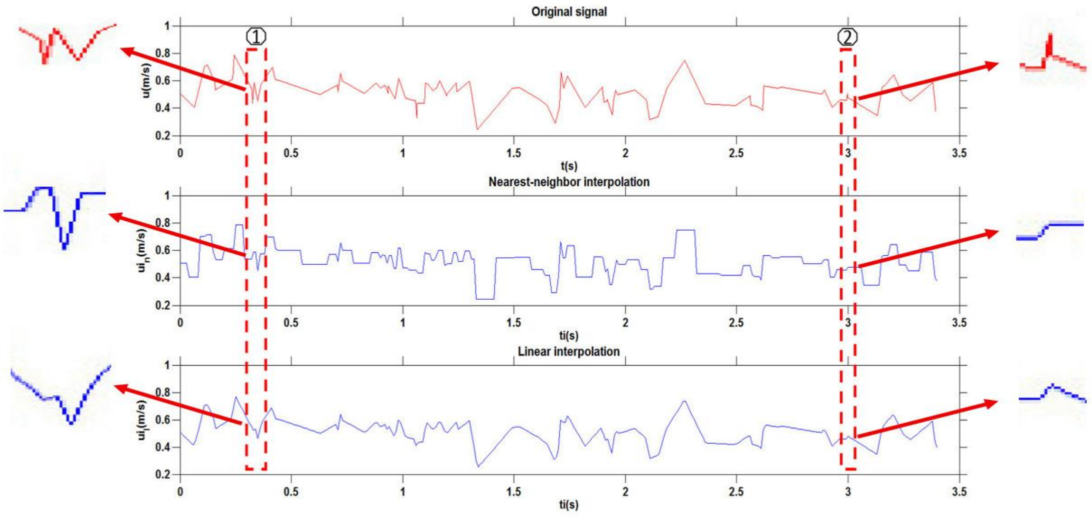

(a) Δt = 10 ms

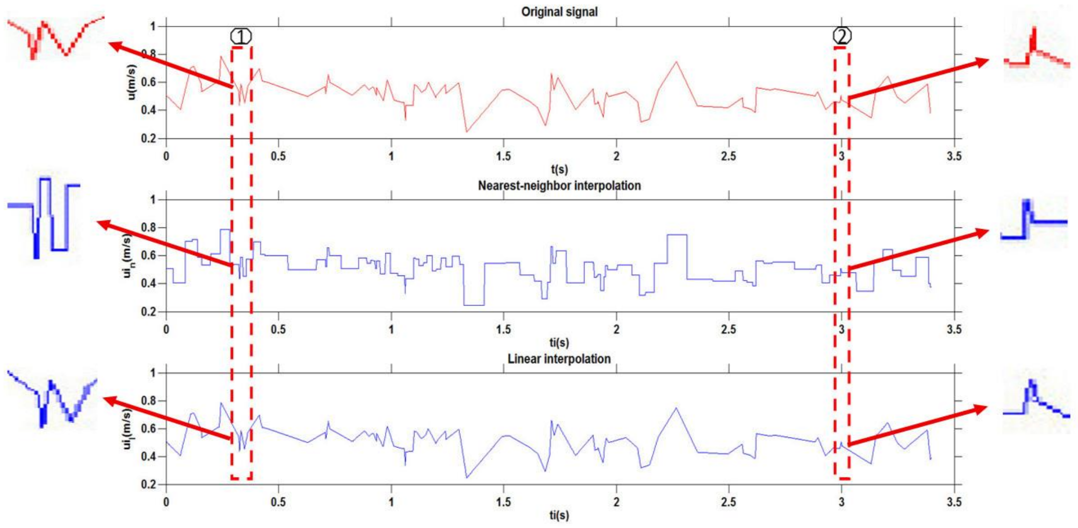

(b) Δt = 1 ms

Fig. 21. Comparison of the original velocity signal sampled at 30 Hz and the reconstructed signal computed from Nearest-neighbor interpolation and linear interpolation with sampling rate of (a) 100 Hz (Δt = 10 ms) and (b) 1000 Hz (Δt = 1 ms) [30].

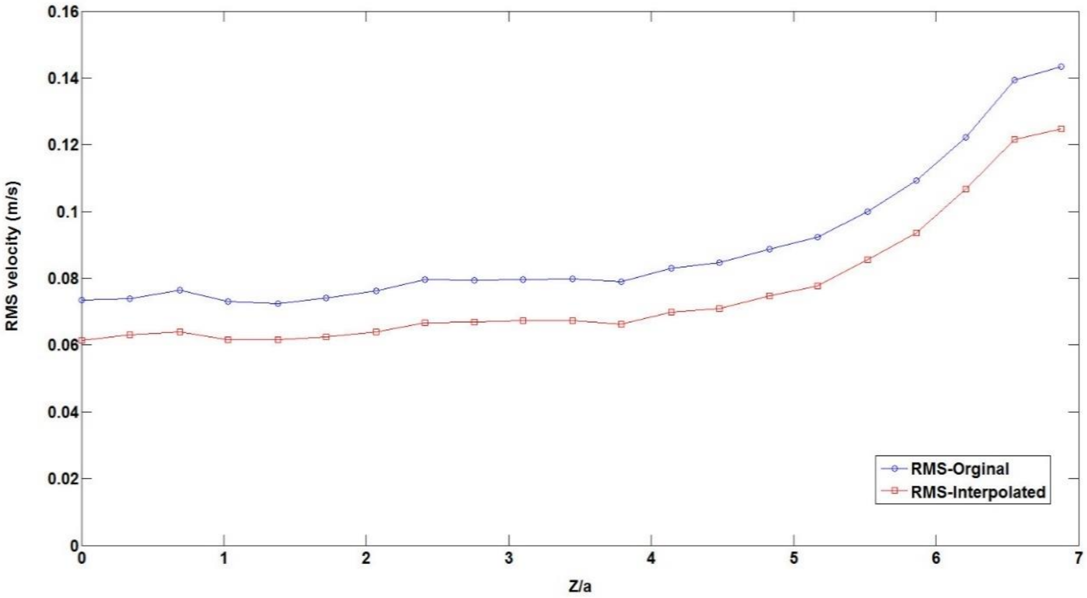

Fig. 22. Comparison of the RMS velocities of the original data with a data rate of 200 Hz and the reconstructed data computed using the linear interpolation method [30]

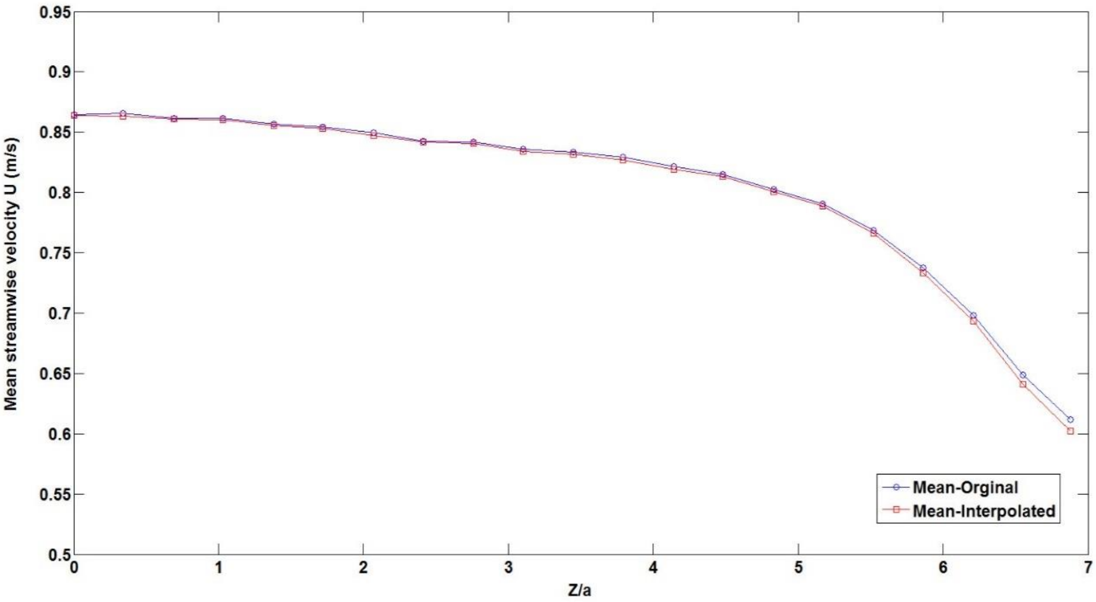

Fig. 23. Comparison of the mean velocities of the original data with a data rate of 200 Hz and the reconstructed data computed from linear interpolation method [30]

4.1.5.1 FFT results

An FFT study was first performed using the 30 Hz data of the fluctuation velocity at *R*, and the results are presented in Fig. 24. It shows that the dominant frequencies of the flow at point R fall within the range of 1 Hz to 10 Hz. According to the Nyquist-Shannon sampling theorem, the maximum frequency that can be detected from a given signal is no larger than half of the sampling frequency. This minimum sampling rate is called the Nyquist rate. Thus, for a signal sampled at 30 Hz, the maximum frequency that can be determined is 15 Hz. That is, measuring any changes in the flow that happen faster than 15 Hz will not be feasible.

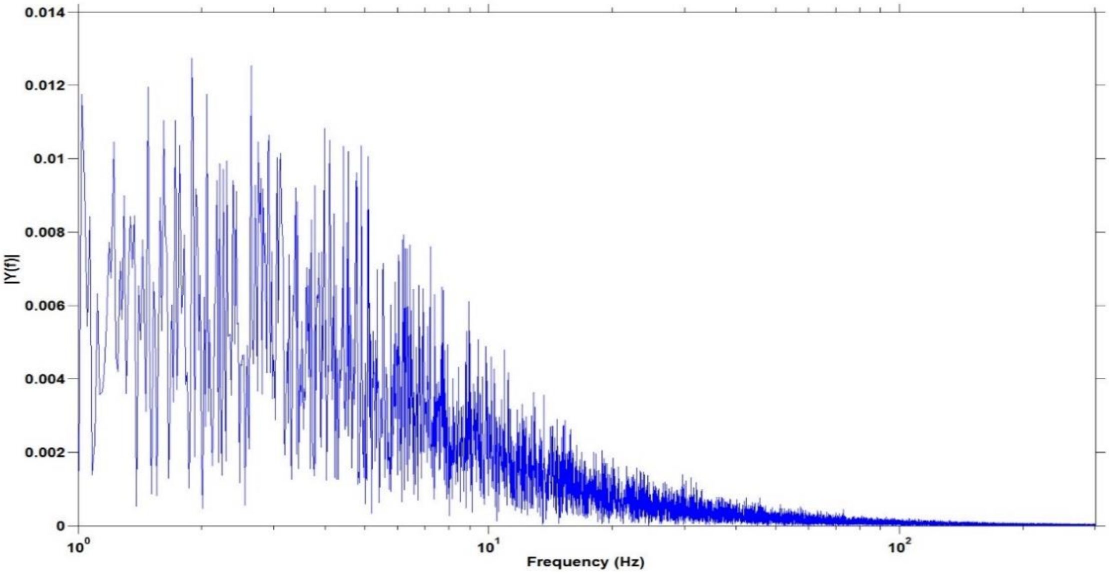

Fig. 24. Single-side FFT output of fluctuation velocity at location R with a sampling frequency of 30 Hz [30]

To resolve this issue and verify if the flow at R is dominated by frequencies of 1 Hz to 10 Hz, only one pair of the laser beams were turned on, and the resulting frequency was about 200 Hz. The FFT output shown in Fig. 25 (a) revealed significantly larger peaks — not only one, although they are too close together to be distinguished in the plot) — around 58.8 Hz. These peaks are considered noise induced by the pump vibration at a frequency of 57.67 Hz. A band-pass filter was employed to remove this noisy frequency. Fig. 25 (b) shows the filtered frequency spectrum indicating that the phenomena that happened in the flow were dominated by frequencies from about 2 Hz to 15 Hz. To quantify the influence of this filtering process on the magnitude fluctuation velocity, a comparison of the unfiltered signal s1 and the filtered one, s2, was carried out. For illustrative purposes, only a short period of the signal was studied. As shown in Fig. 26 (a), s2 matches s1 most of time except where the filtered signal creates a few wiggles at certain locations in time. By subtracting s2 from s1, the magnitude of the difference can be obtained (Fig. 26 (b)). The maximum difference occurred at around t = 5 s and was smaller than 0.03 m/s. A zoom-in view shown in Fig. 26 (c) reveals that the difference is actually a sinusoidal wave. Fig. 26 (d) is the FFT output of this sinusoidal wave showing that the peak frequencies — again, more than one very close to each other — were about 58.8 Hz, which was the frequency set for the filter. Thus, the FFT study here serves as a cross-check of the filter because, in theory, the difference between signals s1 and s2 is the part that the filter removed. Although the magnitude of difference of s1 and s2 was evaluated, the vibration of the pump does not only influence the magnitude of the velocity but also the turbulence structure and the onset point of the turbulence, which is extremely hard to quantify.

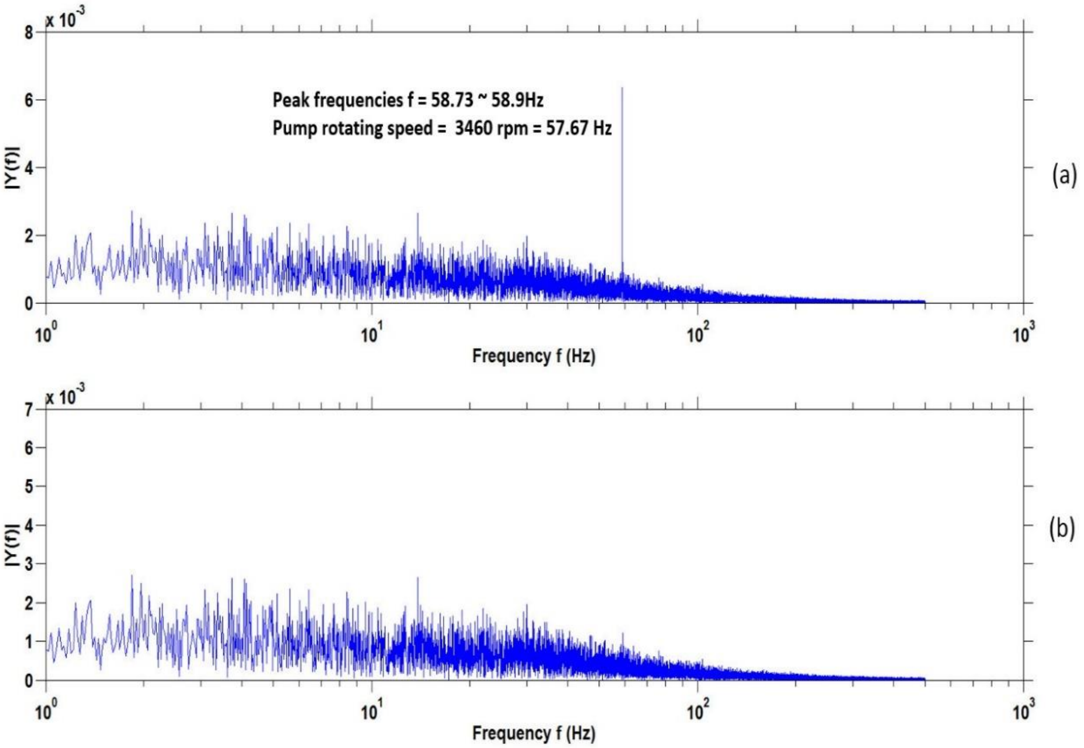

Fig. 25. Removal of the noises induced by the pump vibration using a band-pass filter [30]

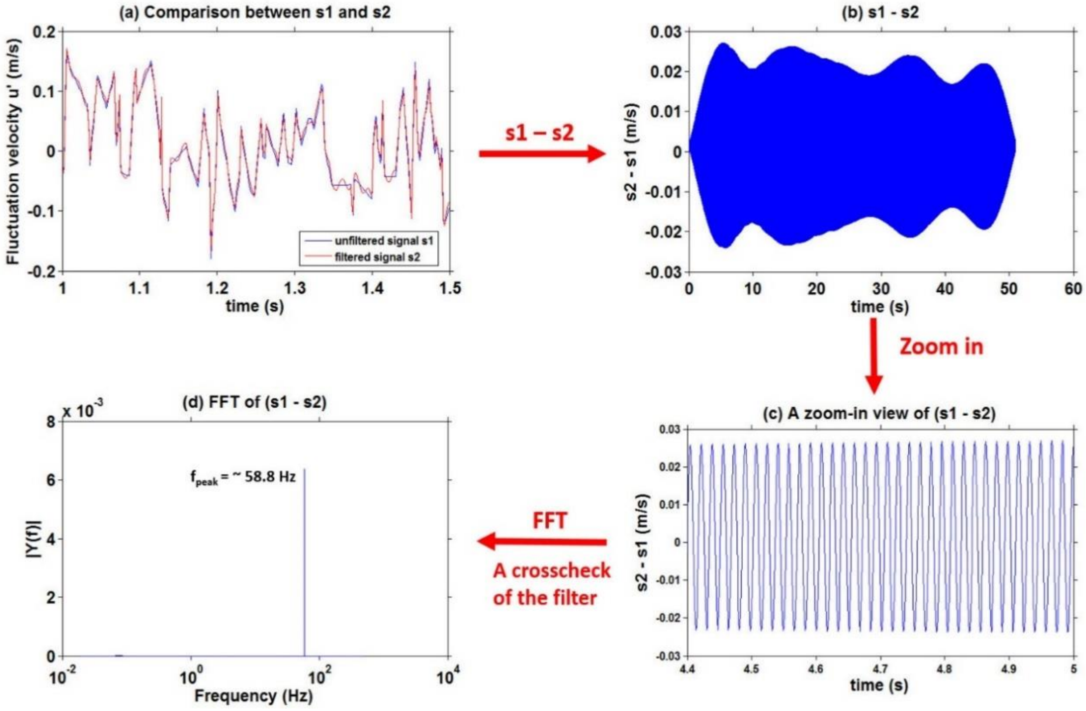

Fig. 26. Evaluation of the difference between the unfiltered and filtered signal [30]

4.1.5.2 PSD results

PSD study could serve as a benchmark for the current experimental data. Fig. 27 shows the PSD distribution in the time (frequency) domain for s1 and s2 computed using Welch's method [28]. The blue line indicates the famous -5/3 slope was found by Kolmogorov. The peaks caused by the pump vibration can be seen clearly in Fig. 27 (a) and disappear once the signal is filtered. The downward peak in Fig. 27 (b) was generated by the filtering process in which the power is set close to zero. The comparison indicates that the energy spectrum is not influenced by the filtering operation except for the removal of the peak. For the flow at location *R*, the energycontaining range is from about 0.1 Hz to 30 Hz, and the inertial region ranges from 30 Hz to 500 Hz, the maximum frequency that can be measured for the resampled data according to the Nyquist theorem. Obviously, a higher sampling rate is required to resolve the dissipation range.

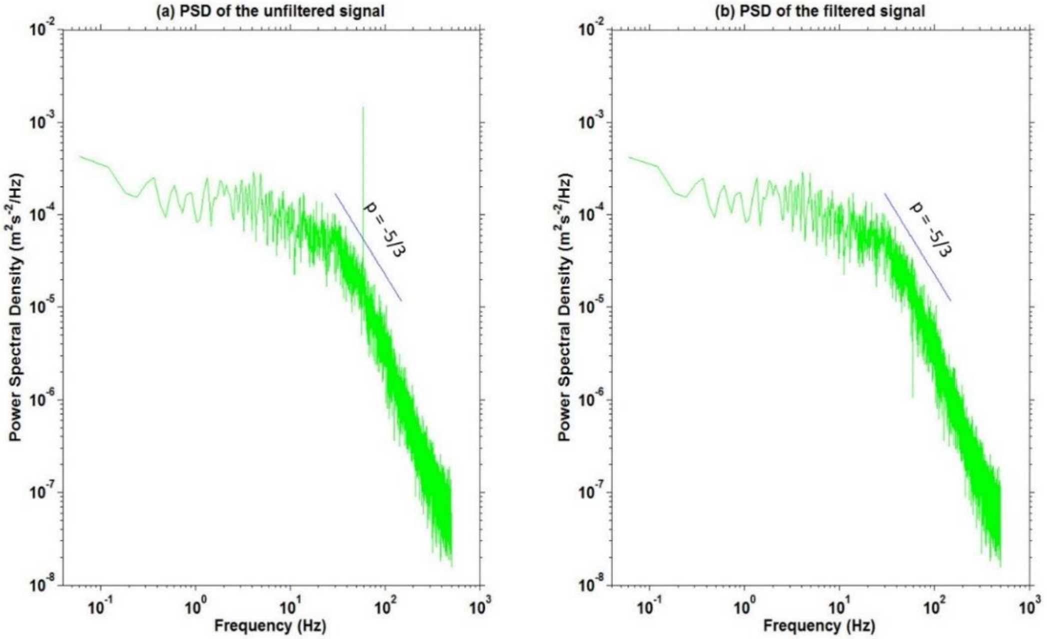

Fig. 27. PSD spectrum of u′ at location R in the time domain of signal s1 (a) and s2 (b) [30]

4.1.5.3 Wavelet results

Three time segments of the signal with an interval of 500 ms were studied. Fig. 28 presents the results of the wavelet transform and the FFT output of the signal between 6500 ms and 7000 ms. Two ordinates, scale and pseudo-frequency, are presented in Fig. 28 (b). Li and Nozaki [29] interpreted the position of the maximum value of the wavelet coefficient *W* as the scale of an eddy. Thus, four different scales of eddies can be observed in this time period. The largest one has a scale of 134 ms corresponding to a pseudo-frequency of about 6 Hz. At certain times, the flow may contain large and small eddies simultaneously. For example, eddies with scales of 134 ms and 40 ms occur simultaneously at t = 6620 ms. The breaking down of large eddies into small eddies was also observable by comparing the flow at t = 6780 ms and t = 6850 ms. As a validation, the FFT output of this segment of signal is shown in Fig. 28 (c). The peak frequencies from FFT match the pseudo-frequencies calculated from the wavelet transform, as indicated by the red lines. The evolution of eddies with different scales can be better observed from the 3-D view of the wavelet coefficients as presented in Fig. 29.

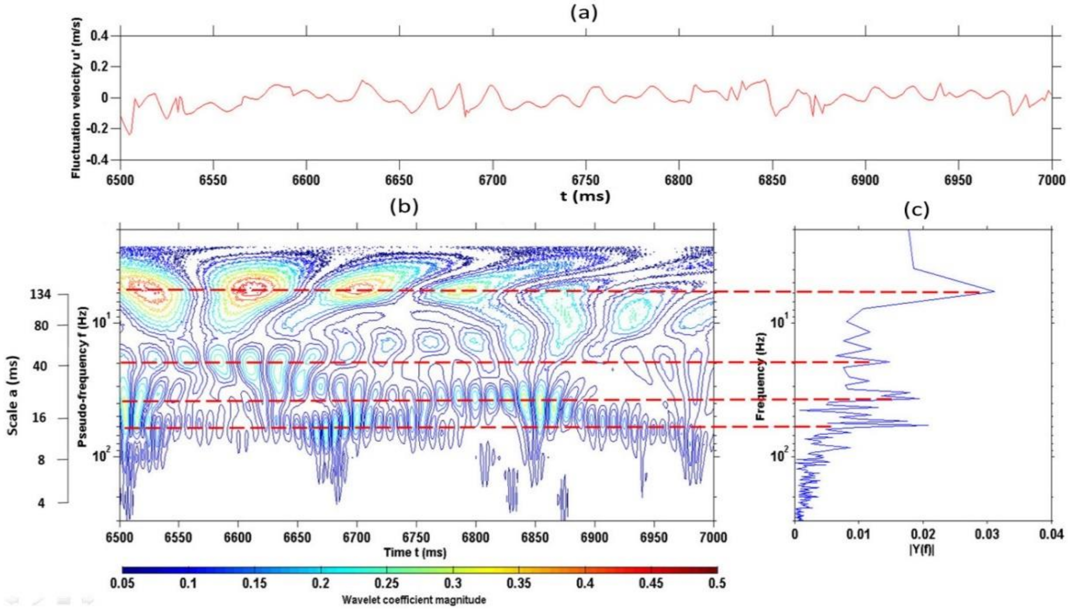

Fig. 28. Wavelet coefficients contours (b) and single-side FFT output (c) of fluctuation velocity at location R from 6500 ms to 7000 ms (a) [30]

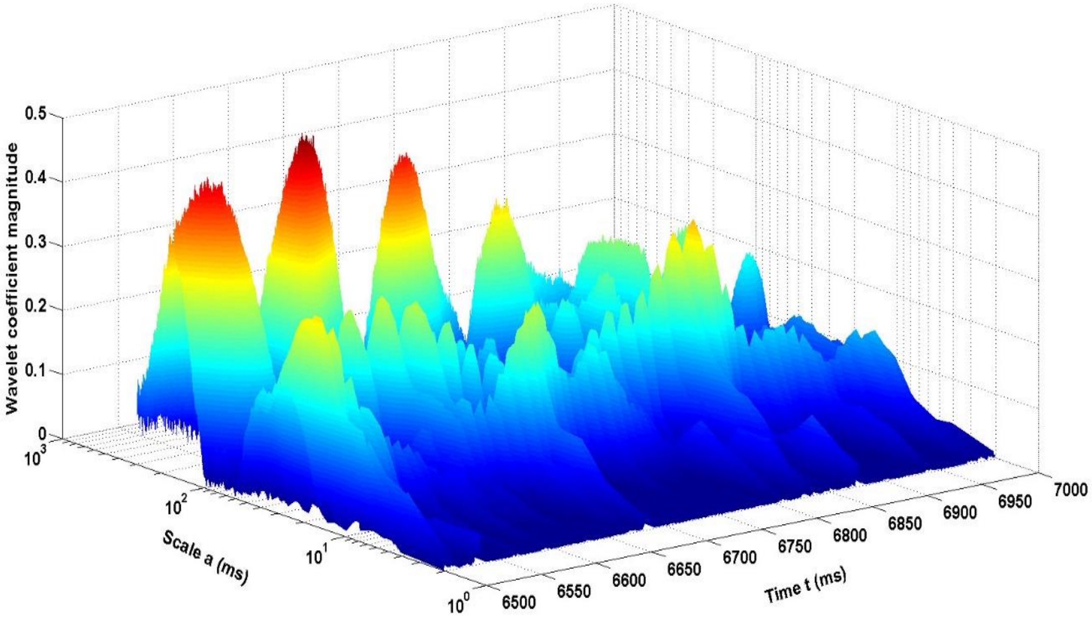

Fig. 29. 3-D view of the wavelet coefficients from 6500 ms to 7000 ms [30]

Fig. 30 shows results for the signals between 20,000 ms and 20,500 ms. No significant break down of large eddies was observed. Large eddies in this time period had a scale of approximately 200 ms corresponding to a pseudo-frequency of 4 Hz. Eddies with a scale of 12ms at t = 20,100 ms disappear later because they break into smaller eddies and the current sampling rate is not high enough to capture them. At t = 20,250 ms, large eddies of about 200 ms in scale are observed to contain at least two other smaller eddies with scales of 110 ms and 40 ms. The large eddy grows when it is close to the end of the signal as indicated in Fig. 31, which shows the wavelet coefficients distribution from 40,000 ms to 40,500 ms. The largest eddy is at a scale of 270 ms and breaks down into a smaller one after t = 40,400 ms. The FFT output contains fewer peaks compared to previous time periods, implying reduced activity in the flow.

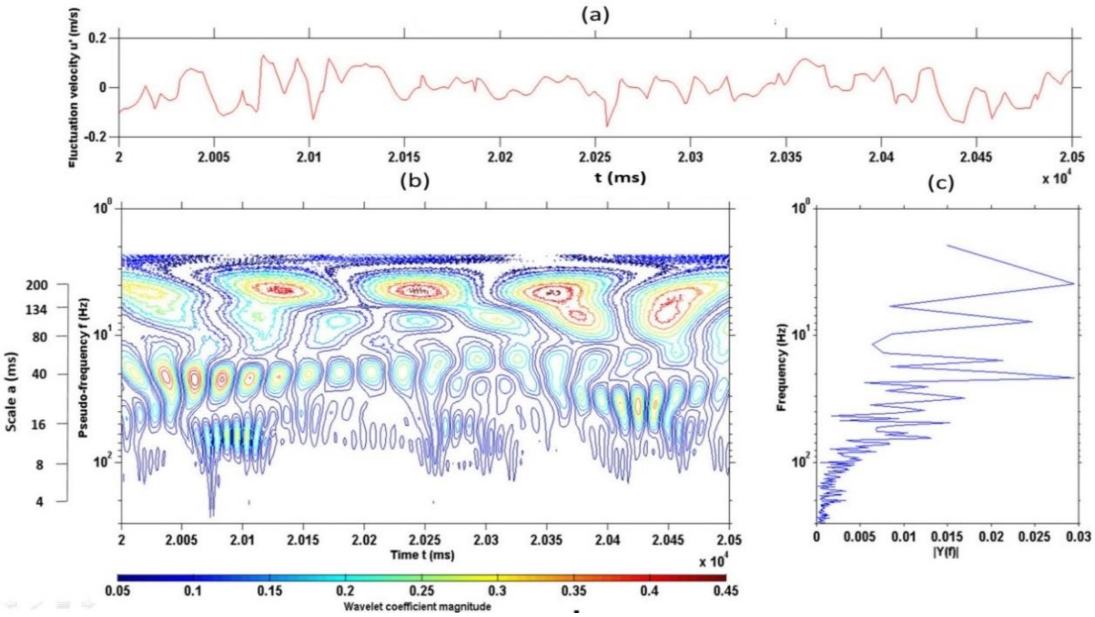

Fig. 30. Wavelet coefficients contours (b) and single-side FFT output (c) of fluctuation velocity at location R from 20,000 ms to 20,500 ms (a) [30]

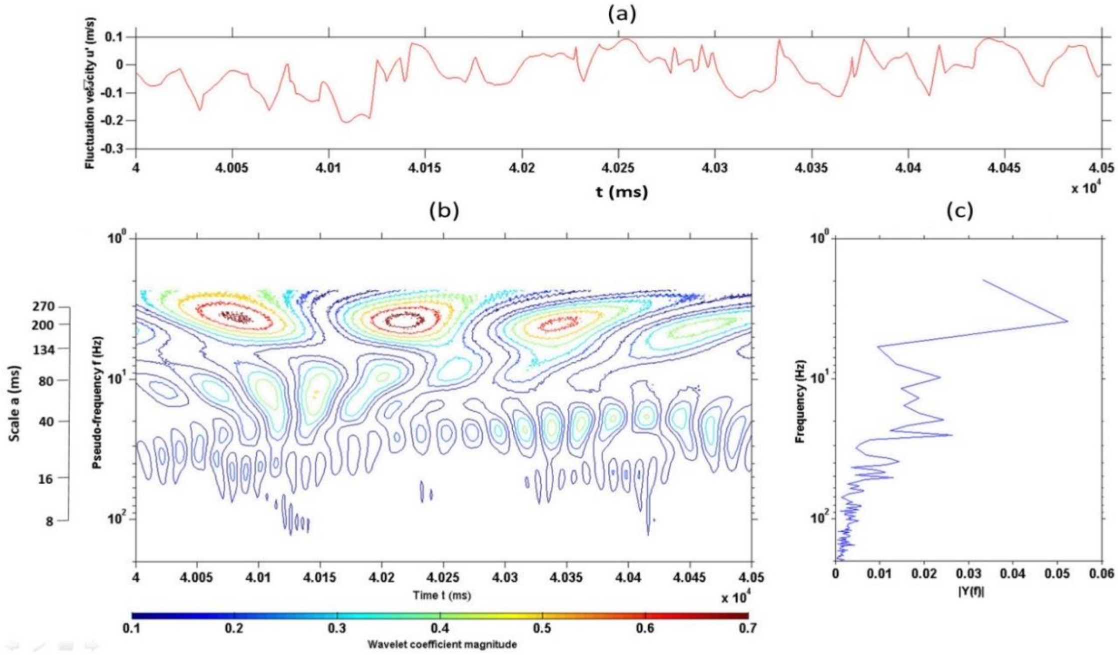

Fig. 31. Wavelet coefficients contours (b) and single-side FFT output (c) of fluctuation velocity at location R from 40,000 ms to 40,500 ms (a) [30]

By exploring the flow structures of different time segments, some flow patterns are found to repeat in the time domain. Fig. 32 (a) and (b) show that a medium-sized eddy at a scale of about 40 ms, which can also be observed in Fig. 32, occurred at both t = 6100 ms and t = 20,050 ms. Similarly, a large eddy at a scale of 270 ms displayed almost identical behavior in the time segments indicated in Fig. 32 (c) and (d). The repeated flow structures characterize the flow. The corresponding frequency of these repeated flow structures can be utilized to validate the transient CFD simulations, such as large eddy simulations (LES).

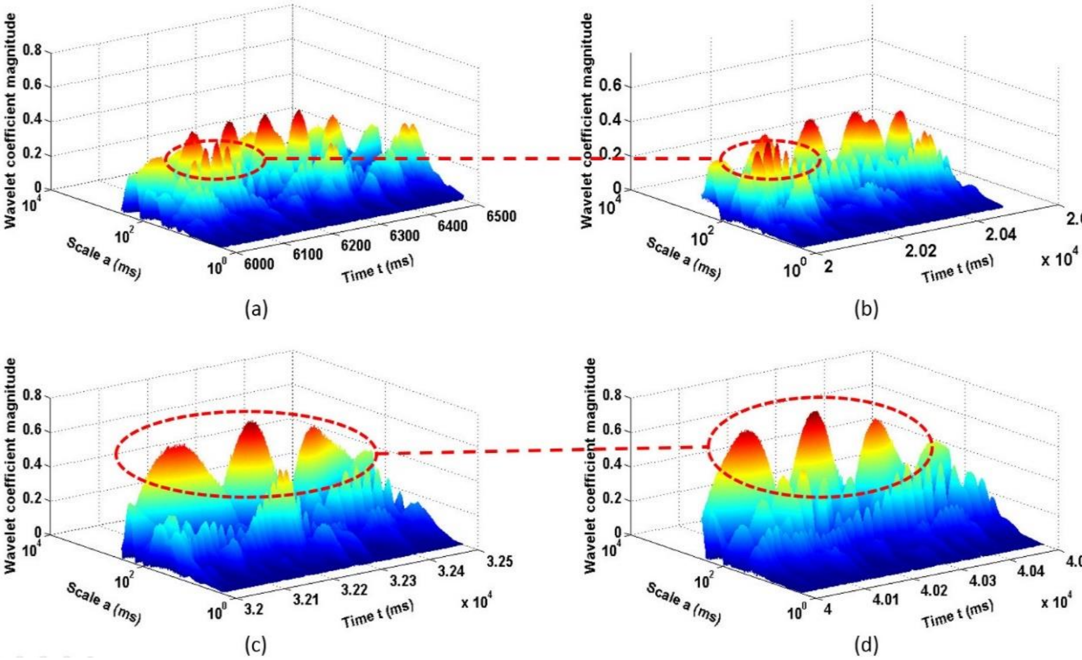

Fig. 32. Similar flow structures observed in different time periods [30]

4.2 PIV results

4.2.1 PIV measurement of 15Hz frame rate with a zoom-out view

As stated in section 2, the measurements were carried out using two scales, scale M1 and scale M2. Scale M1 corresponded to the area ranging from y/a = 0 to 12 while scale M2 was from y/a = 0 to 3. The purpose of running an extra measurement with scale B was to evaluate the enlargement effect of PIV. So the results reported in this work are based on scale A. Results from both scales will be comparted and discussed. Measurements using scale M1 were repeated three times to evaluate the uncertainties. These three measurements A, B and C were carried out at different times and independently. The system was cleaned and resampled before any new measurements started to ensure the independence of each measurements. The results from three measurements were then ensemble-averaged to evaluate the mean streamwise velocity *U*, mean lateral velocity *V* and other turbulence quantities, such as turbulence intensity, Reynolds stress and Z-vorticity.

4.2.1.1 Mean velocity

The mean velocities *U* and *V* were calculated by time-averaging over 800 frames or pairs of images. Then, as mentioned above, these three averaged mean velocities were ensemble-averaged again to obtain the final mean values. Fig. 33 presents distribution of *U* with streamlines. The two jets were symmetrical about the center axis. Obviously, the jets had not combined at y/a = 12.3, the highest elevation in this measurement. Streamlines clearly indicate the entrainment of surrounding fluid. In the recirculating zone, reversed flows were observed. One interesting phenomenon captured in this zone is that the flow, let's call it flow A, moved upward first from y/a = 0 then "met" another stream of flow B coming downward at about y = 1.4. Due to mutual forces from these two flows, flow B started to recirculate while flow A moved to the lateral direction. In addition, the flow, let's call it flow C, at some distance above flow B had an opposite moving direction. The point separating flow C and B is MP, where U is zero. The location of MP was found to be at about y/a = 3.45. In order for other researchers to compare with results in this work, U distribution at four different elevations are plotted in Fig. 34. The errors bars were the standard deviations from three independent measurements.

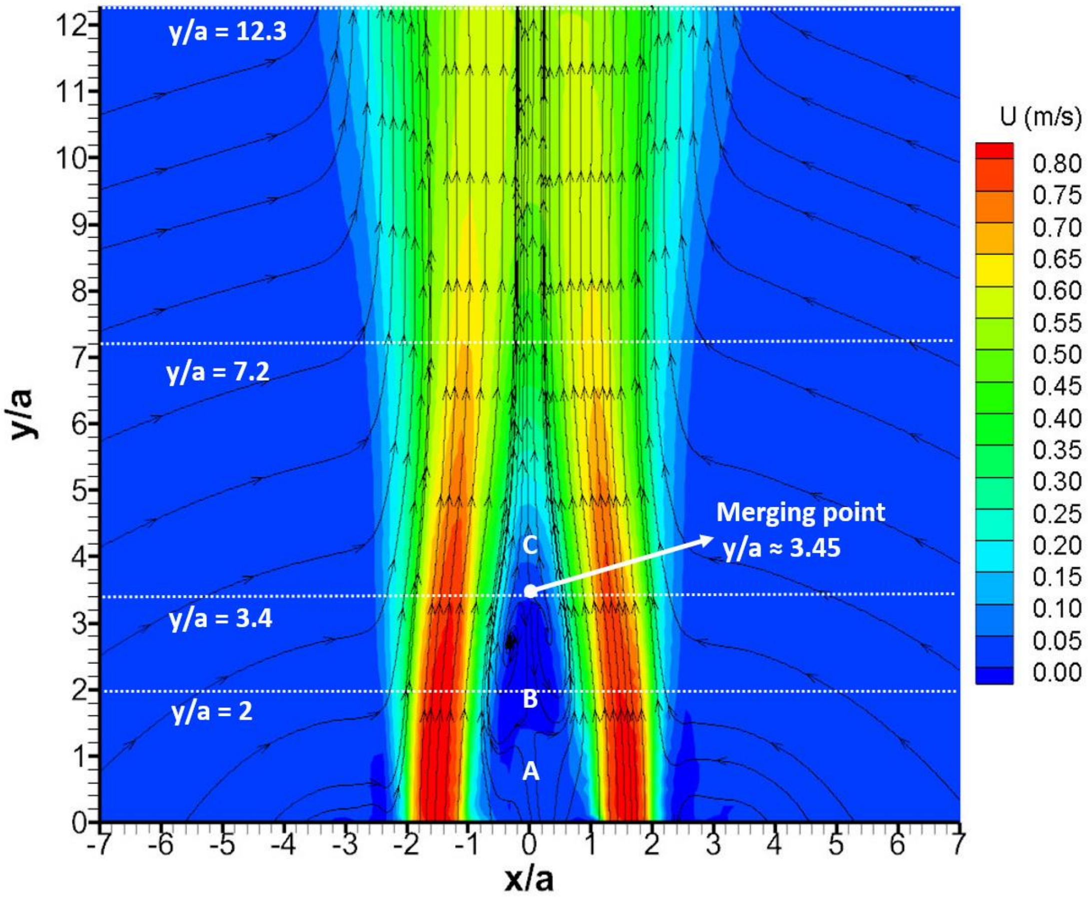

Fig. 33. Streamwise average velocity U profile and streamlines [31]

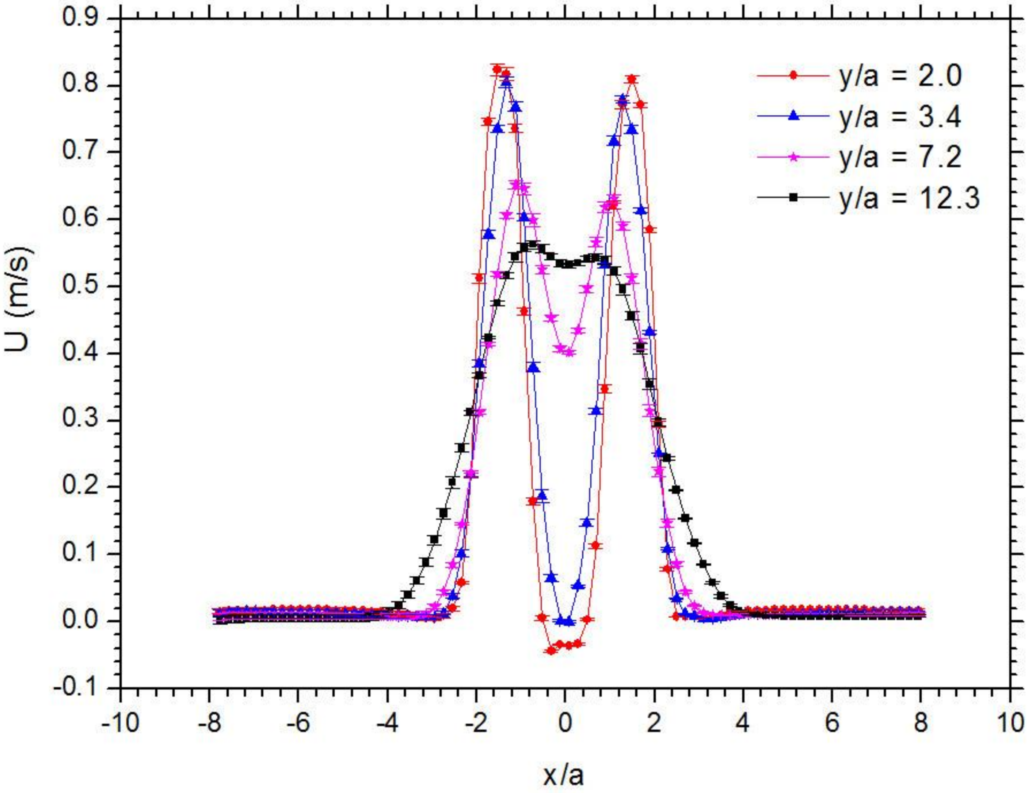

Fig. 34. Streamwise average velocity U at different elevations [31]

The distribution of V is shown in Fig. 35, and Fig. 36 presents the plots of V at different locations. Strong lateral movements of the flow were observed in the region between y/a = 2 and y/a = 5. This is the region that two jets were converging on. Lateral movements of the surrounding fluid were also significant near the outer edge of each jet. This implies that a low pressure region was formed due to the fast moving jets near the exit. In order to find the exact location of MP, the mean vector field, as shown in Fig. 37, was calculated using *U* and *V*. The mean vectors were highly symmetrical along the center line. The zoomed-in view of the region circled in Fig. 37 clearly confirmed the location of the MP, which was at about y/a = 3.45. This value is close to what was found in previous LDA measurements performed by the authors, which was located between y/a = 1.72 and 3.45 as there were no measurement points available inside this range [30].

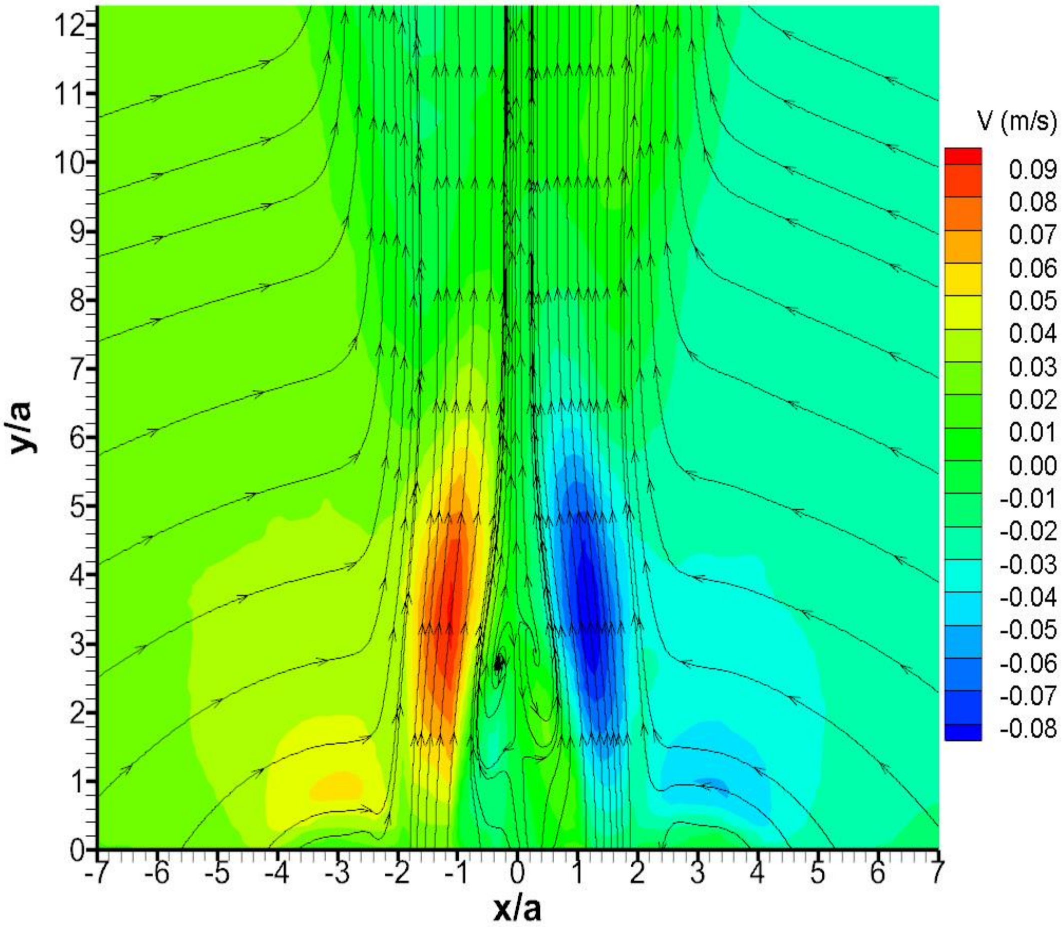

Fig. 35. Lateral average velocity V distribution [31]

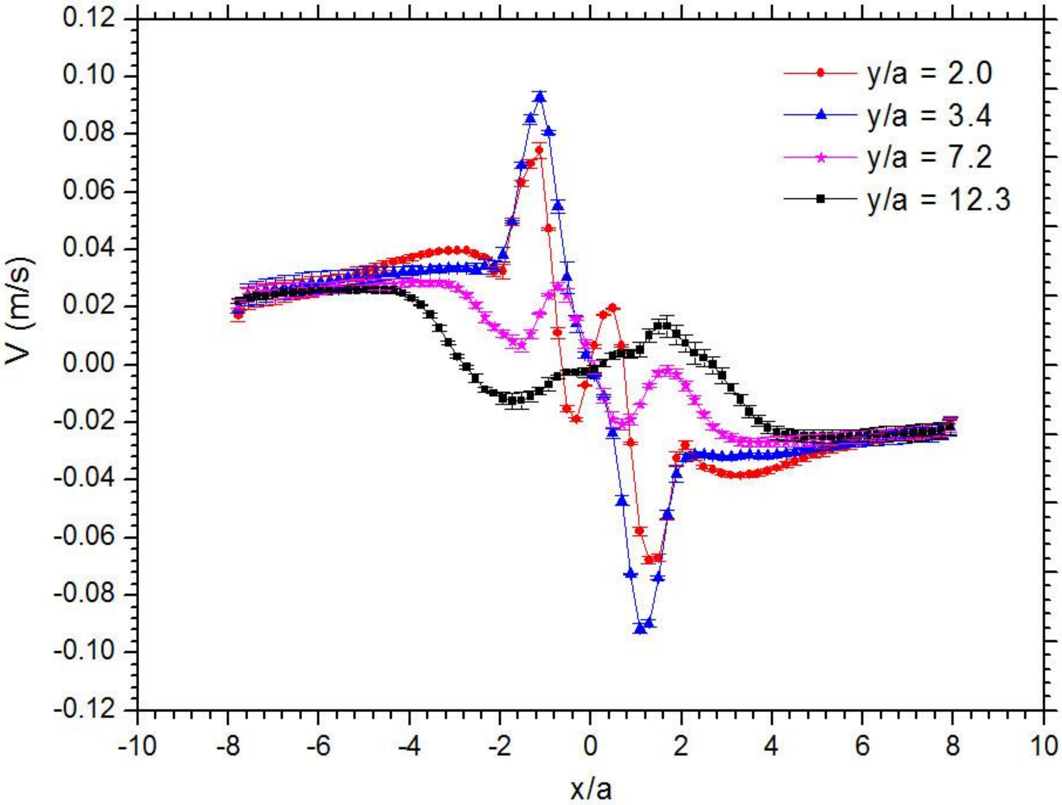

Fig. 36. Lateral average velocity V at different elevations [31]

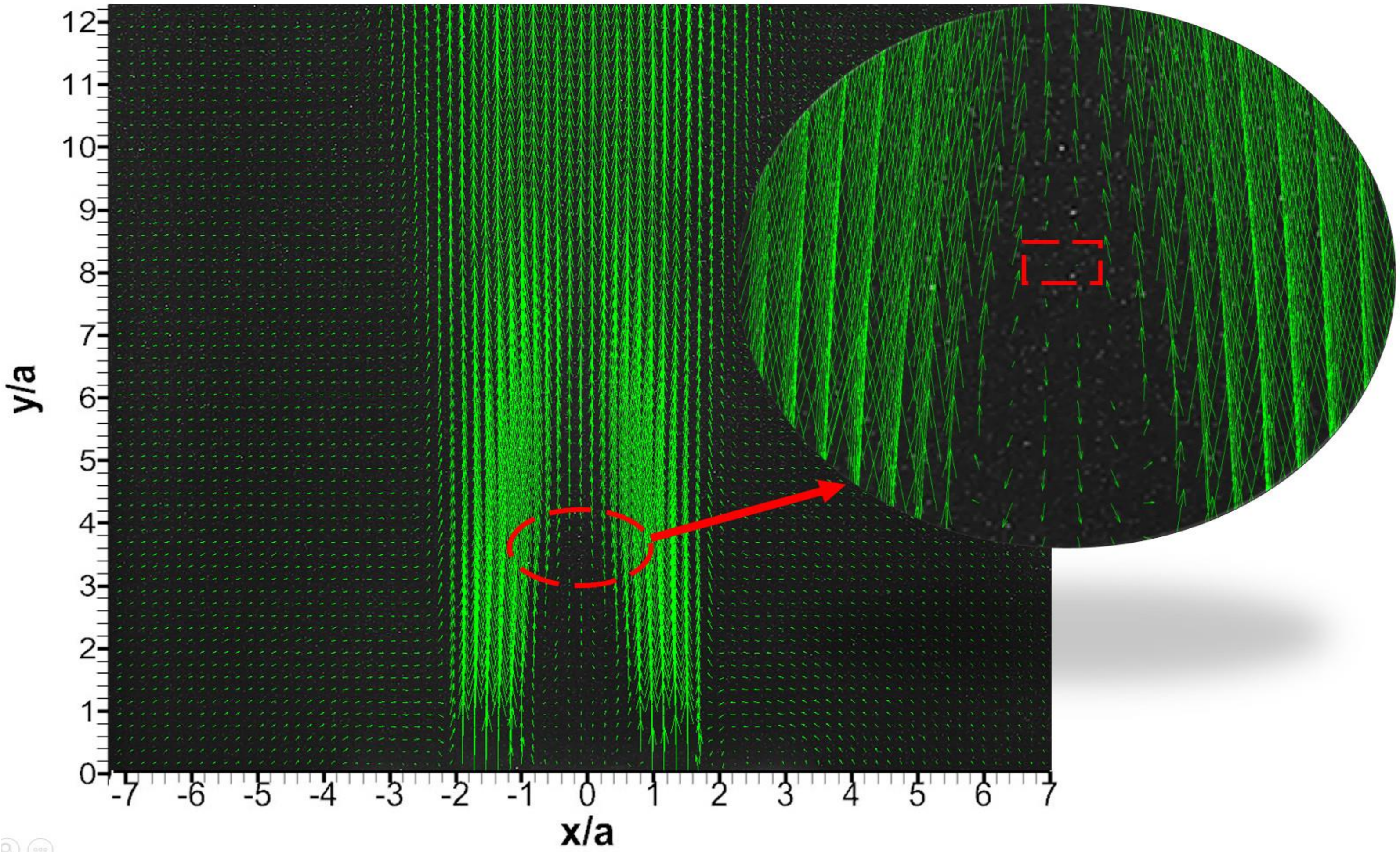

Fig. 37. Mean vector field and identification of the MP location where U = 0 [31]

4.2.1.2 Mean z-vorticity

With known *U* and *V*, z-component vorticity, an indication of the rotation speed of fluid particles in the x-y plane, can be computed. The mean z-vorticity distribution is shown in Fig. 38. The positive direction is pointed out of the x-y plane. Strong vortices were located at the edges of the jets. These vortices died out along the positive y direction. No strong vorticities were found at locations above y/a = 10. The friction forces between the moving jets and static surrounding them generated these vortices. Vortices in the inner edge area started moving closer around the MP indicating a strong combination of activities.

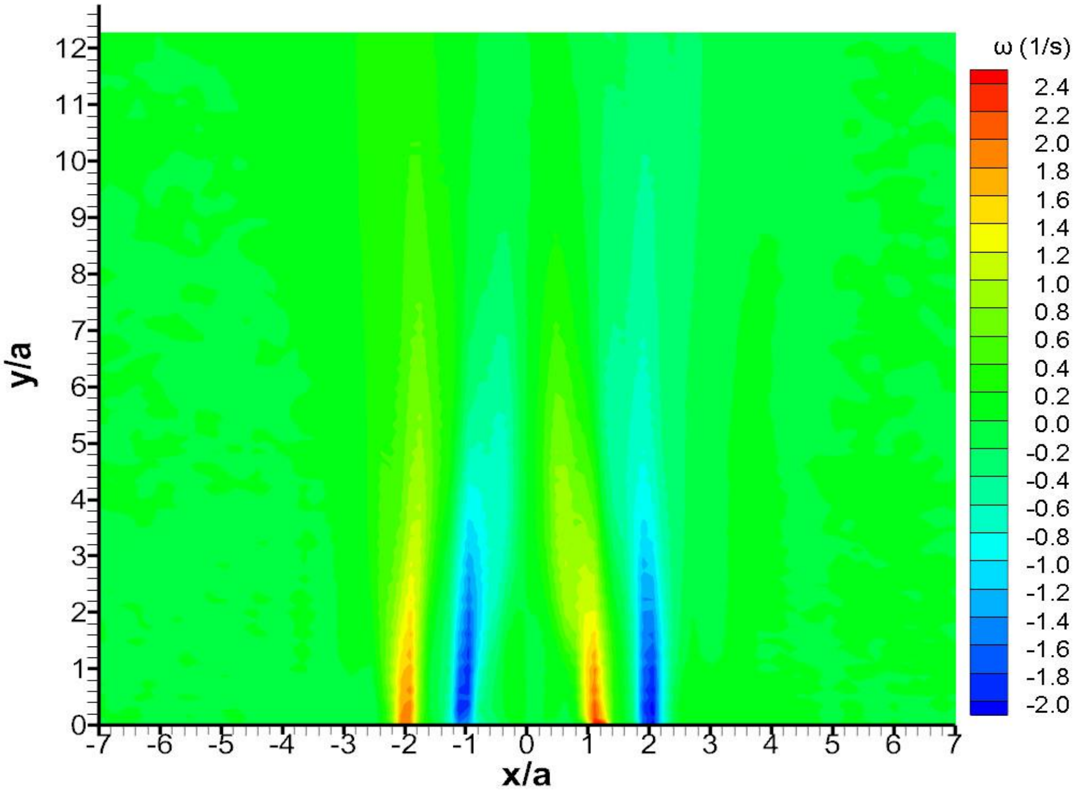

Fig. 38. Z-vorticity distribution [31]

4.2.1.3 Turbulence intensity

The power of turbulence can be evaluated by computing turbulence intensity, or put more simply, root mean square (R.M.S.) velocities. It represents the degree of fluctuations of fluid particles. The turbulence intensity near the jet nozzles determines the position of MP and the mixing condition in the converging region. Fig. 39 shows the profile of streamwise turbulence intensity U_{rms}, and Fig. 40 presents the values at four elevations. The two potential cores near the jet nozzles could be clearly observed, in which the turbulence intensities were close to zero. Due to the shear force, turbulence intensity was higher at the edges of the jets. A long and narrow low-fluctuation region was found in the space between the two jets. It was noticeable that the turbulence intensity was low in the recirculating zone although flow behaviors in that zone were complicated. Lateral turbulence intensity V_{rms} and the detailed values at different locations are presented in Fig. 41 and 42, respectively. Strong fluctuations existed in the merging region after the MP implying that the main momentum transfer happened in the merging region. The lateral fluctuations were not strong in the recirculating zone either. A relative low-intensity region was found around $y/a = 11$. This is because the major momentum transfer happened around $y/a = 7$, and energy exchange in the lateral direction was weak.

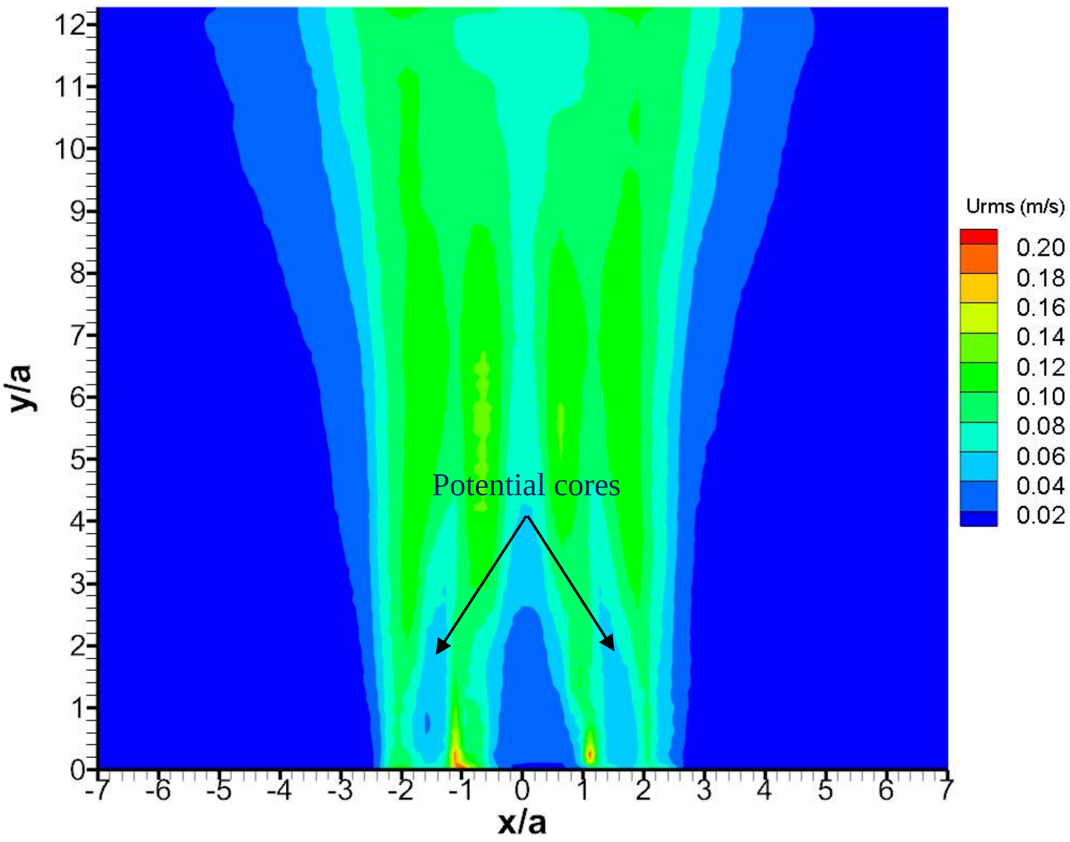

Fig. 39. U_{rms} profile [31]

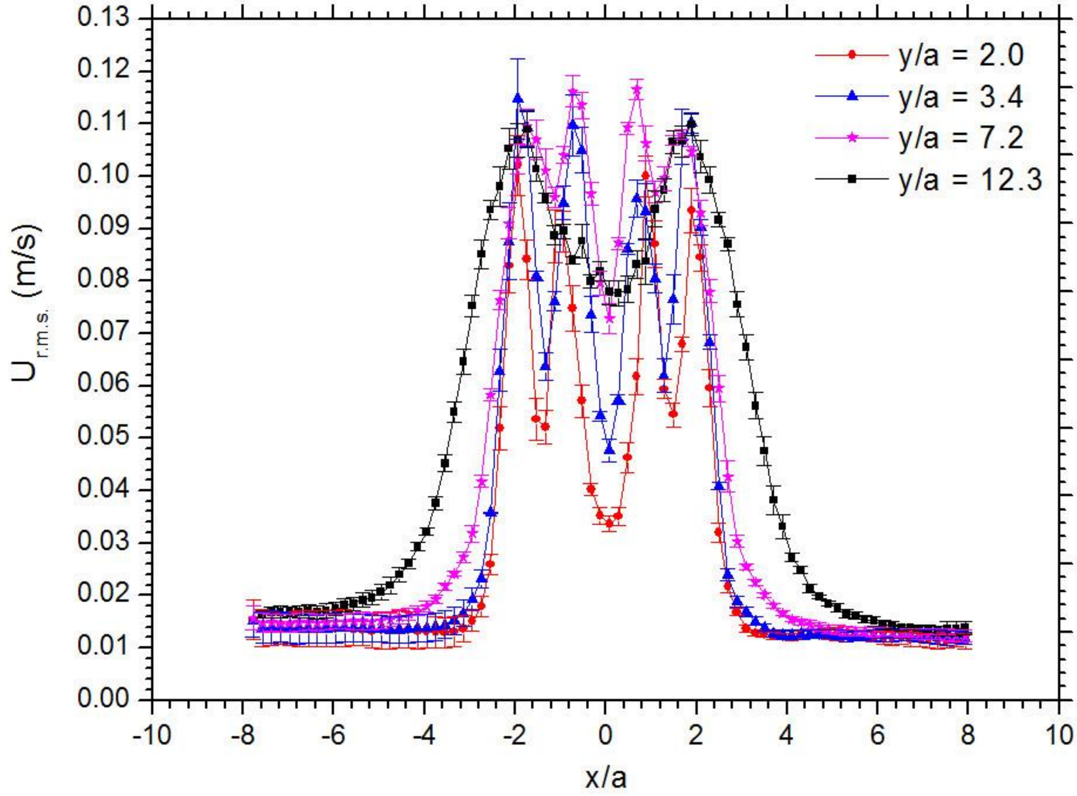

Fig. 40. Streamwise average R.M.S. velocity $U_{rms.}$ at different elevations [31]

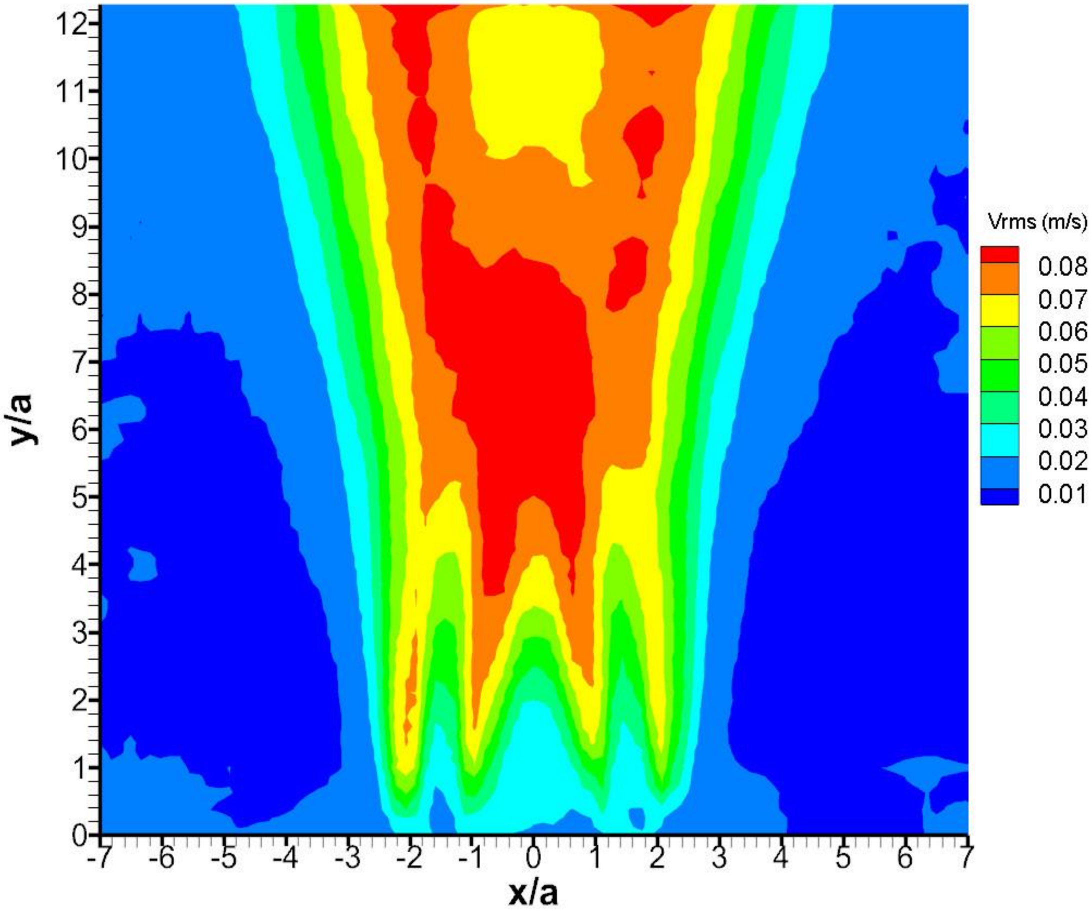

Fig. 41. V_{rms} profile [31]

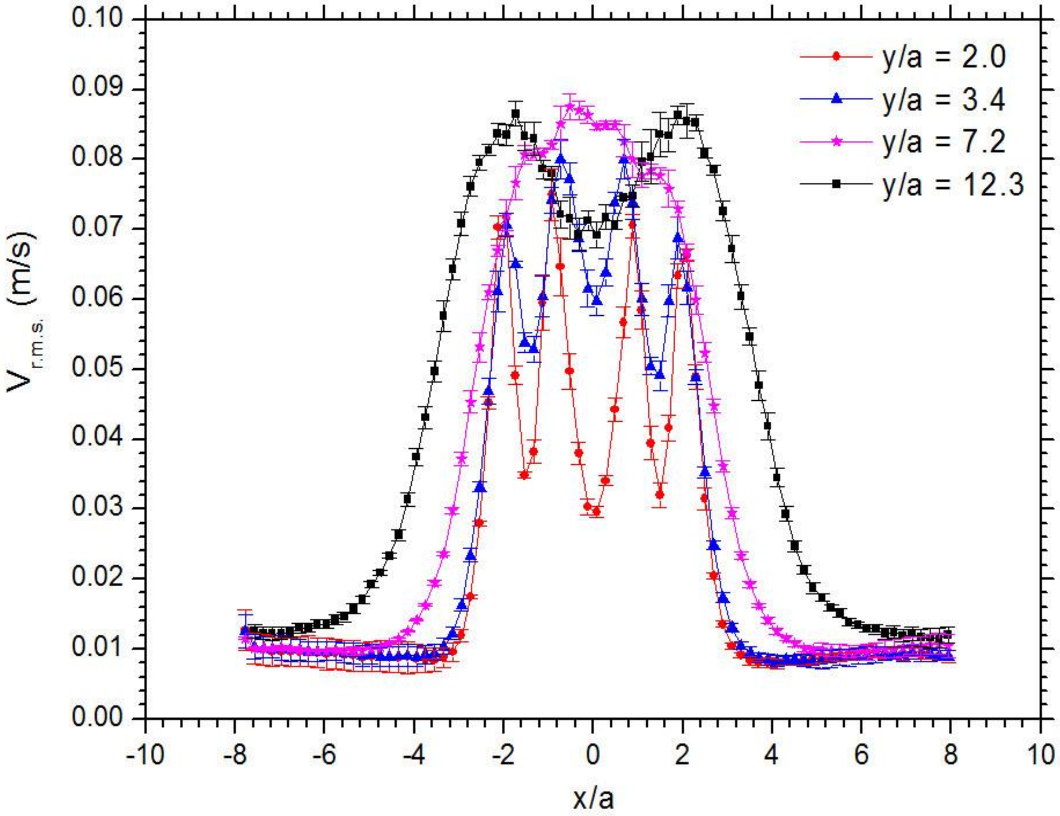

Fig. 42. Lateral average R.M.S. velocity V_{rms} at different elevations [31]

4.2.1.4 Reynolds stress

Reynolds stress is a measure of momentum flux in the flow. Fig. 43 shows the Reynolds stress component distribution. It shows that the strongest momentum transfer happened not in the converging region but in the merging region, specifically the region between y/a = 3.5 and y/a = 8.5. It is interesting to see that y/a = 3.5 is the exact location of MP. That is, the effective momentum transfer started right after the MP. Another region with significant momentum flux was the outer edge of the jet which ranged from y/a = 1.5 to y/a =12, which is the maximum value that this measurement could reach with respect to the satisfying resolution. Again, the majority of the momentum transfer happened in the merging region.

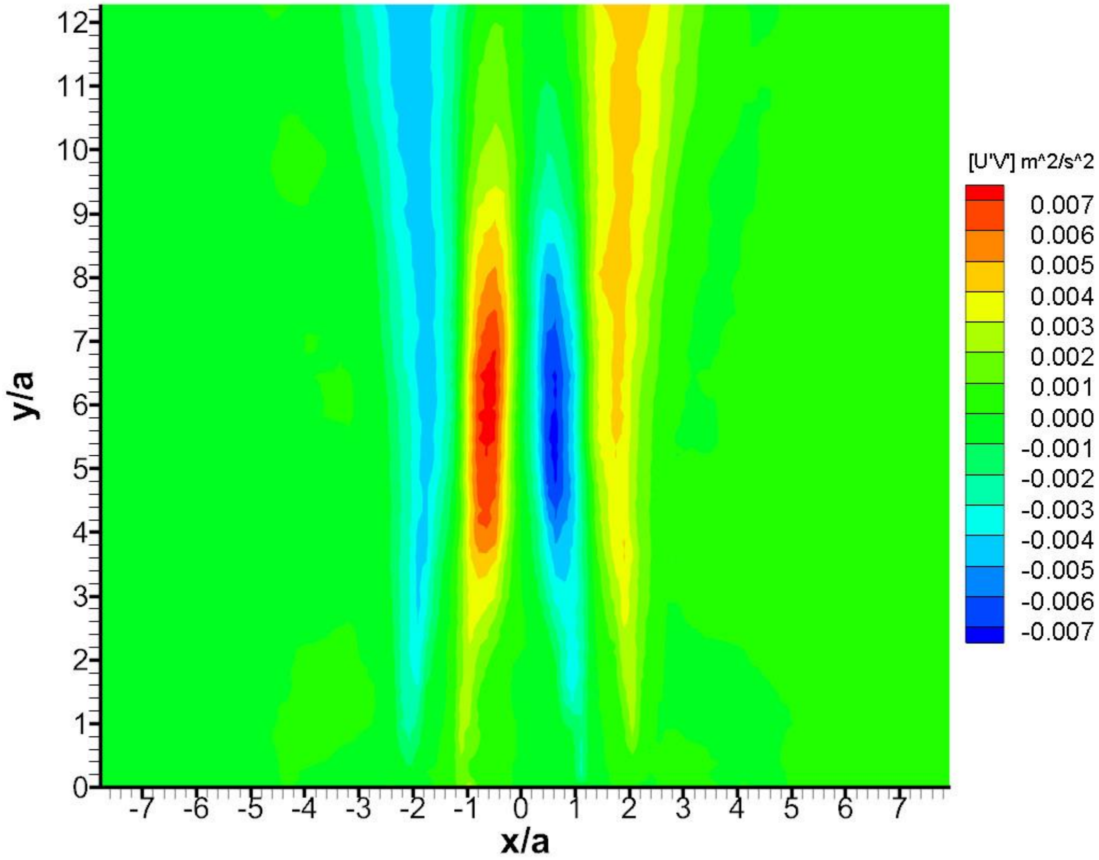

Fig. 43. Reynolds stress distribution [31]

4.2.1.5 Instantaneous vector field

One of the benefits of using PIV compared to LDA is that the full field instantaneous velocity profile can be captured simultaneously. Different from averaged quantities, instantaneous velocities enable us to better understand the evolution of the flow in the time domain. Because of the nature of turbulence, the flow pattern changes with time. Thus, studying the instantaneous velocities measured at different frames can help us reconstruct some meaningful information that is lost in the mean quantities. For example, as shown in Fig. 44, the movement of vortex A could be clearly identified. Since vortex *A* emerged periodically, the time period between these two frames might be necessarily equal to the real length of time that vortex A needed to travel to the position of A'. Similarly, the growth of the vortex could be clearly revealed.

Another interesting phenomenon found by analyzing the instantaneous vector field was how the two jets interacted with each other. Two characteristic interacting patterns were observed repeatedly as presented in Fig. 45. In the left picture, the two jets diverged immediately after hitting each other. However, as shown in the right-side image, the two jets rejoined and separated a few times before they fully merged. These vector profiles are useful for better understanding the behaviors of twin jets. This information was totally lost in the averaged quantities.

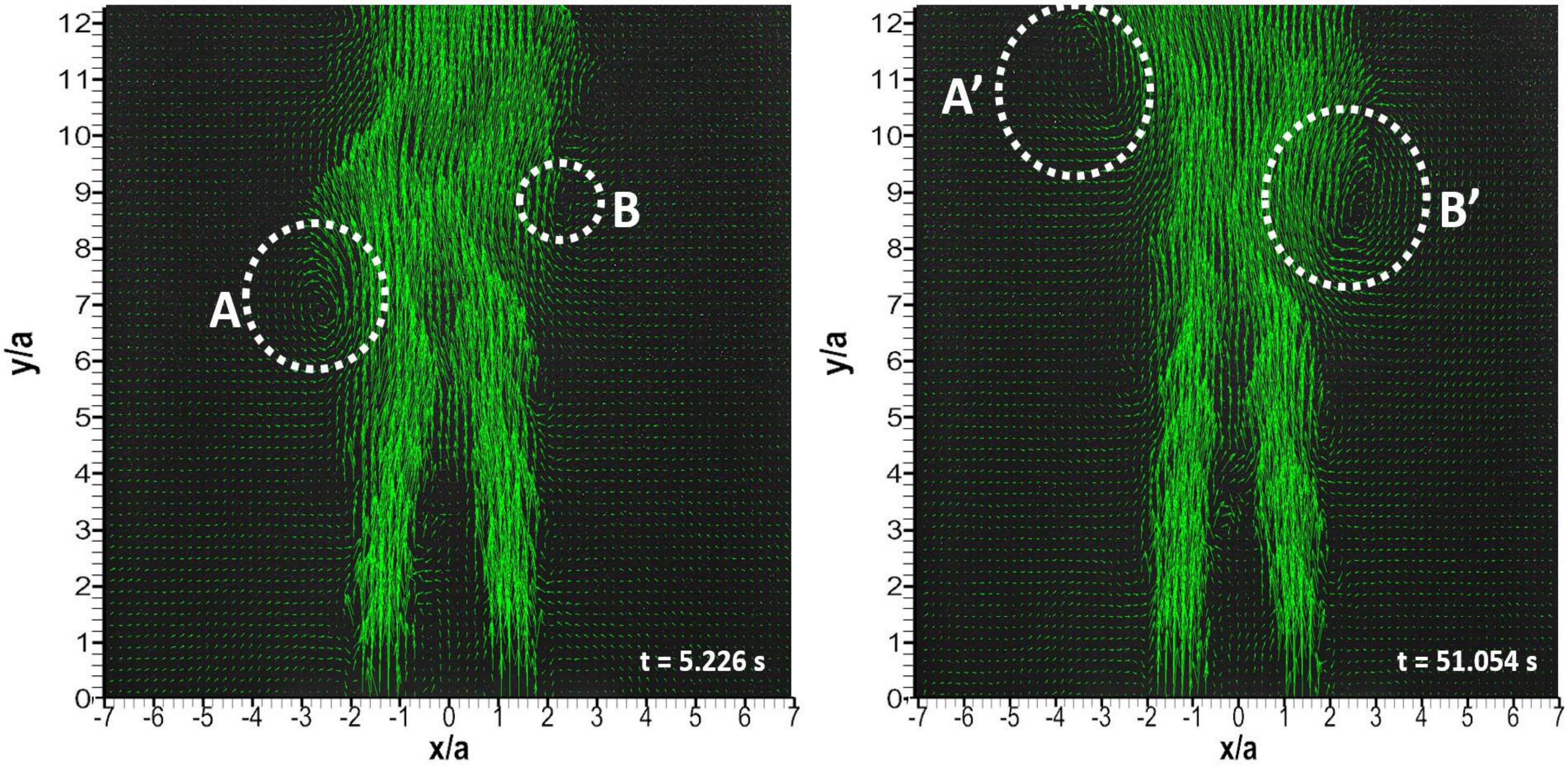

Fig. 44. Instantaneous vector field obtained at t = 5.226 s (left) and t = 51.054 s (right) showing the growing and movement of vertexes A and B (not within one period) [31].

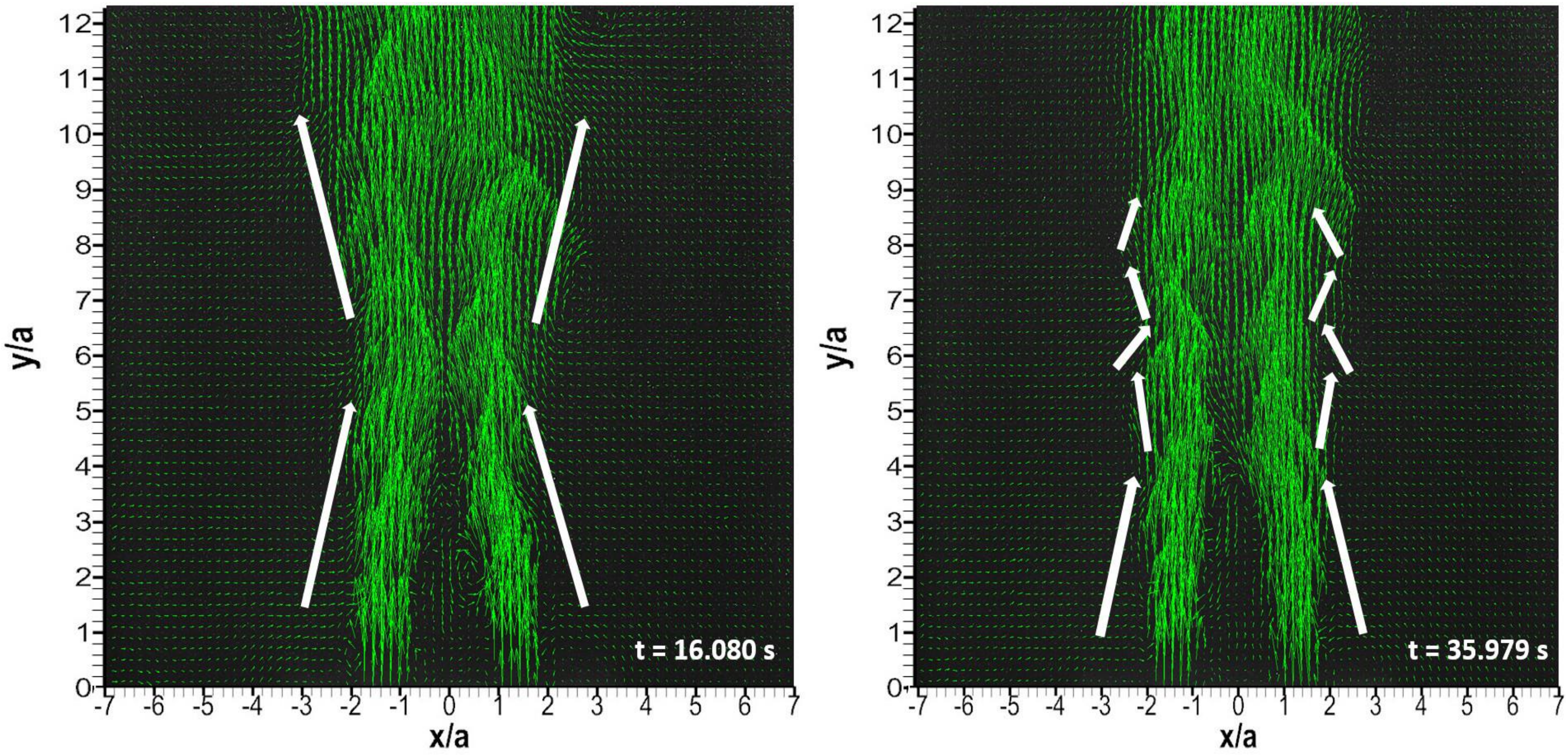

Fig. 45. Two characteristic and repeated patterns observed [31]

4.2.2 PIV measurement of 15Hz frame rate with a zoom-in view

In order to further investigate the flow behaviors in the recirculation zone, the camera was moved closer to the facility providing a zoom-in view of the recirculation zone. This magnification can generate clearer images of the particle movements in this region, which improves the accuracy of the turbulence statistics study. The setup of the parameters of the laser and the camera were the same as mentioned in section 4.2.1. Figs. 46 and 47 present the mean streamwise and lateral velocity distributions in the recirculation zone.

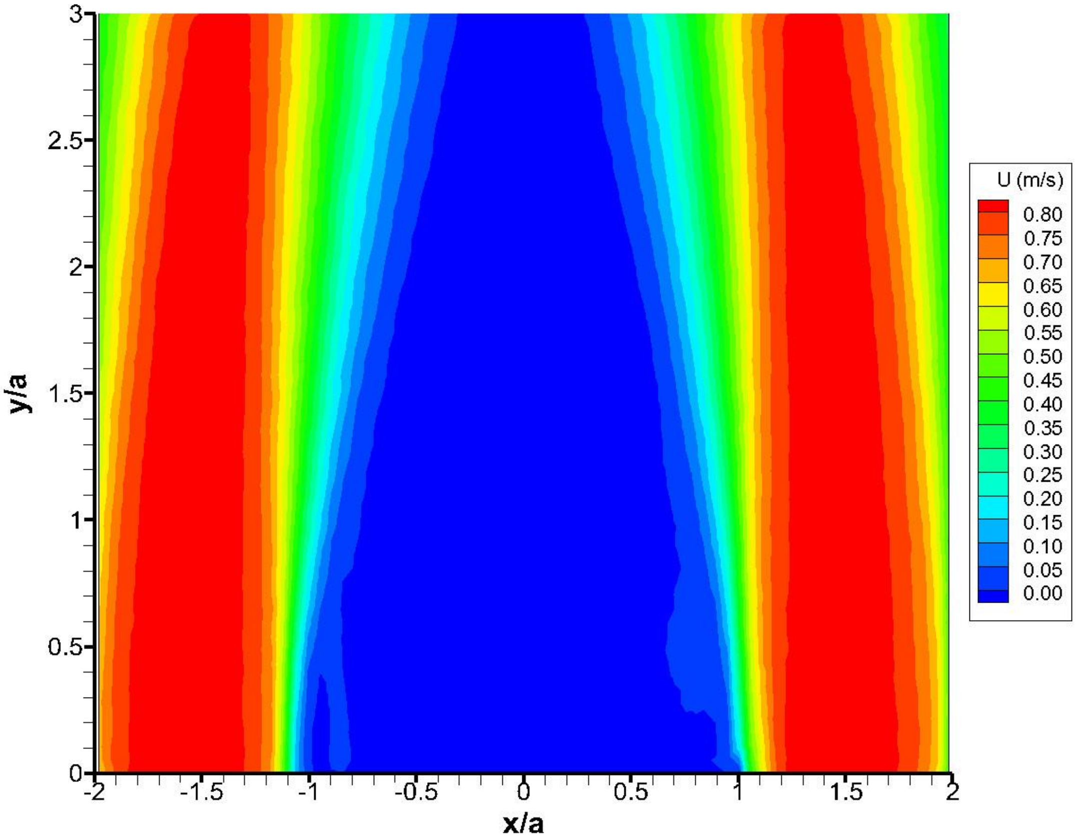

Fig. 46. Mean streamwise velocity *U* (m/s)

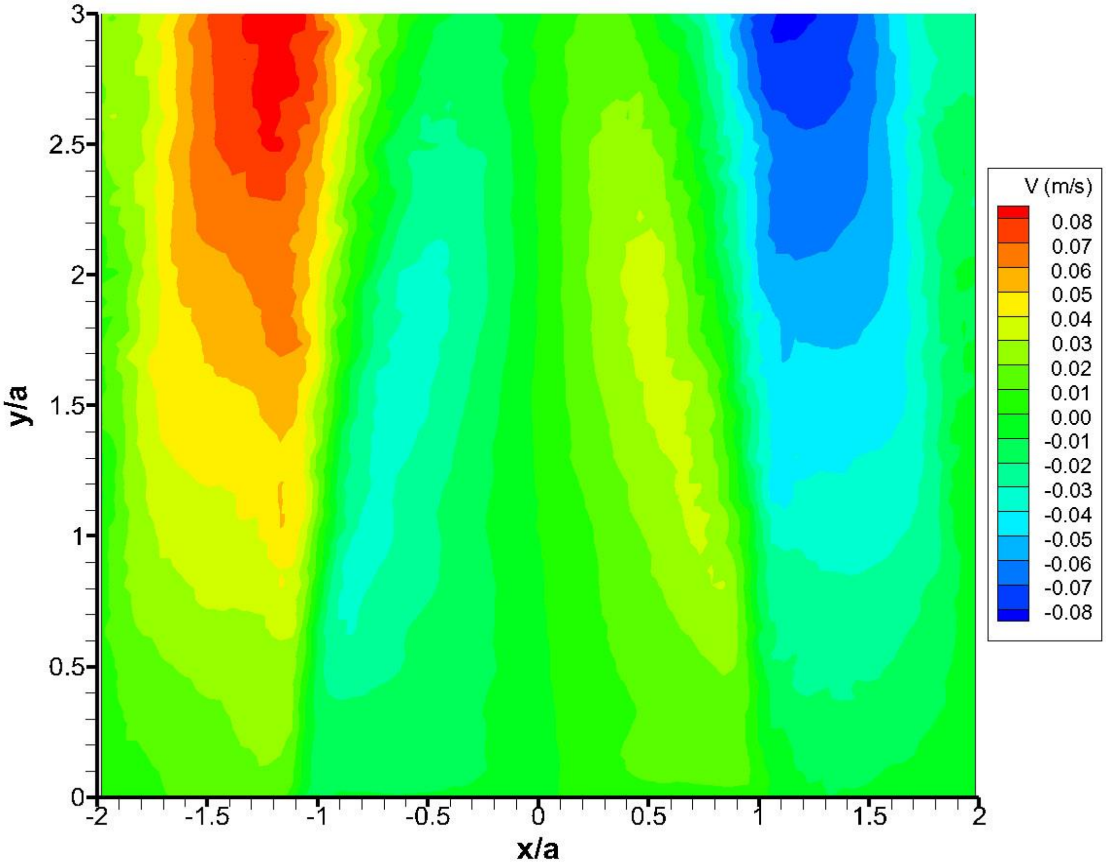

Fig. 47. Mean lateral velocity *V* (m/s)

It can be seen that the magnitudes of the velocities of the flow in the recirculating zone were much smaller compared to the main stream jet velocities in the streamwise direction. However, in the lateral direction, significant movements of the flow were observed in the region between *y/a* = 0.5 to 2.5 in the inner sides of the jets. In addition, the *V* velocity magnitudes of the two jets reached their maxima not at the middle of the recirculating zone as expected but the top of the recirculating region (*y/a* = 3). A vector field shown in Fig. 48 provides a better representation of the flow behaviors in this region. Due to the frictions between the jets and the originally static fluids between the jets, swirls are created near the inner edges of the jets. This is only the average movements of the flow but does not represent the transient situations under which the flow conditions are more random.

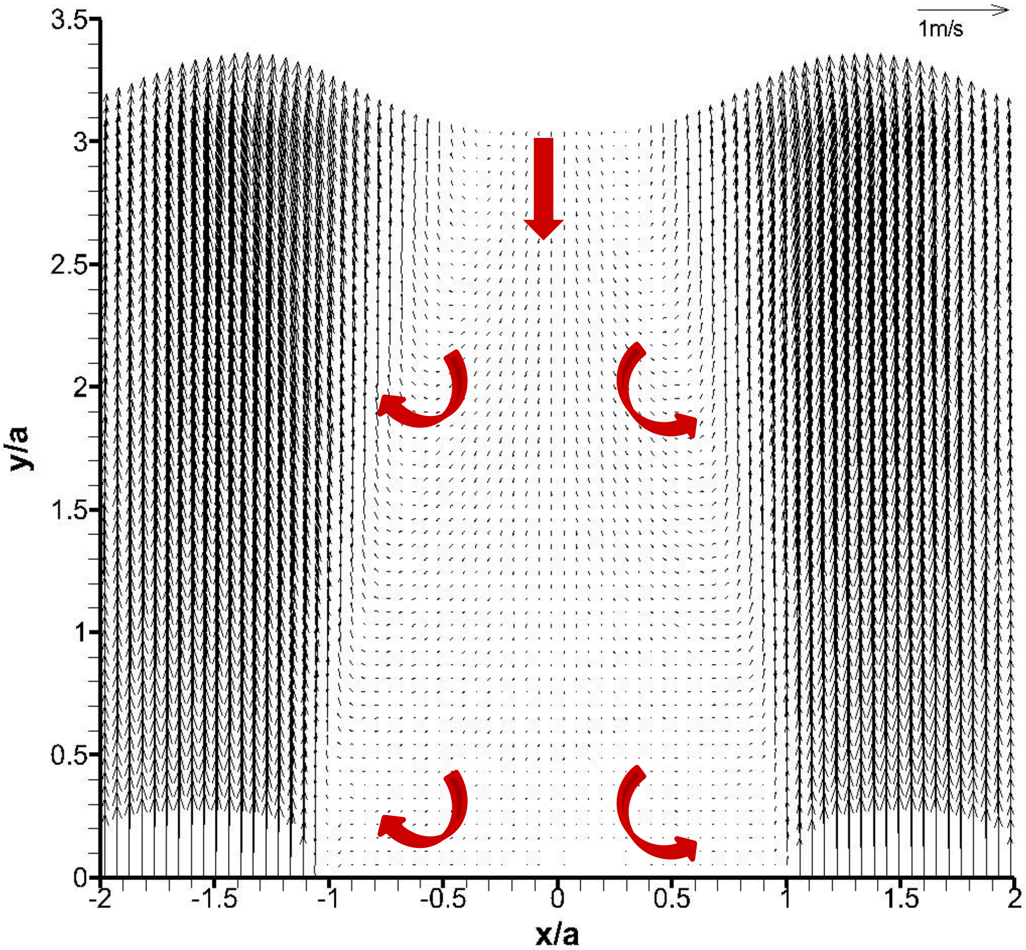

Fig. 48. Mean Vector field

Figs. 49 and 50 show the turbulence intensities in the streamwise and lateral directions. The potential cores can be clearly observed for both jets. The turbulence intensity values were low at the bottom of the recirculating region indicating an almost stagnant condition there. For the streamwise turbulence intensity, the values in the middle of the recirculating zone were higher than the top and the bottom. In the lateral direction, the fluctuations were mainly in the top region of the recirculating zone.

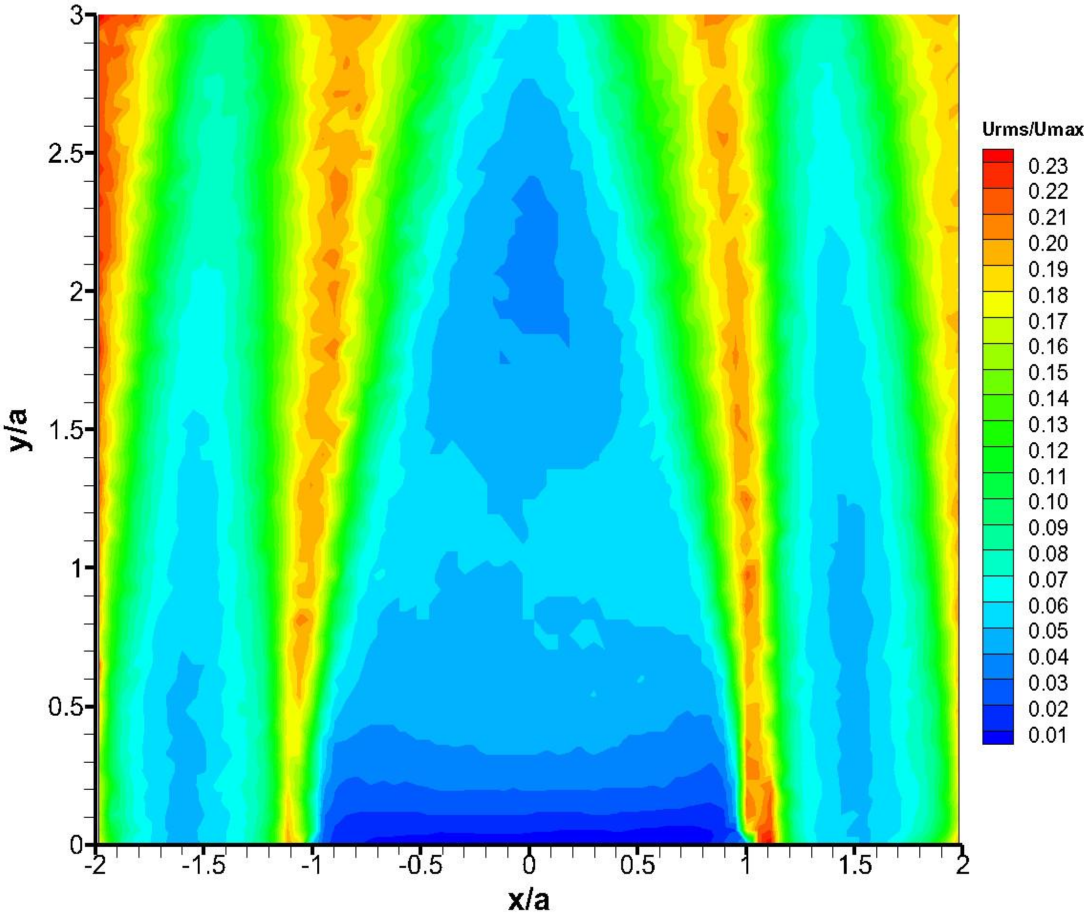

Fig. 49. Streamwise turbulence intensity

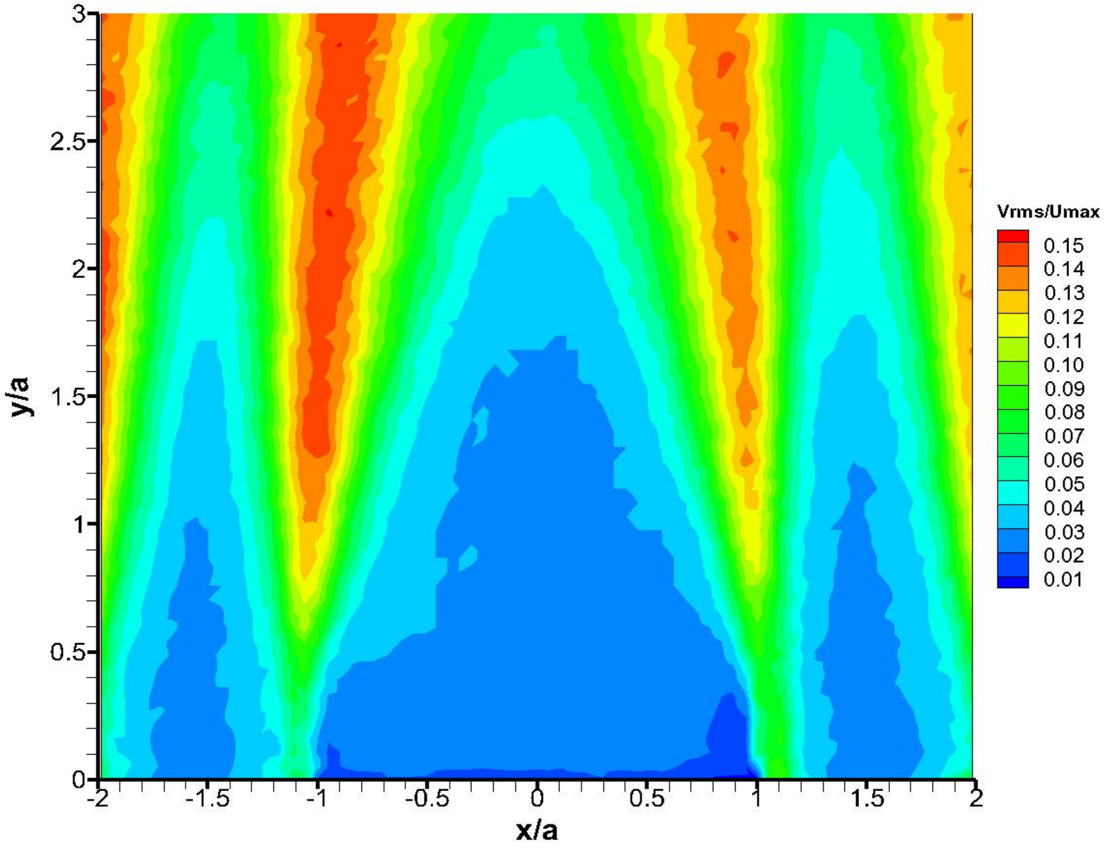

Fig. 50. Lateral turbulence intensity

The Reynolds stress component is presented in Fig. 51. Similar to previous results, significant momentum transfer happened at the edges of the jets as a result of the large shear forces. In the recirculating zone, the magnitude of the Reynolds stress was close to zero implying that the momentum transfer was weak. Although the flows in this region is recirculating, the momentum transfer was limited by the small magnitude of the velocity. The majority of the momentum was transferred near the inner and outer edges of the jets.

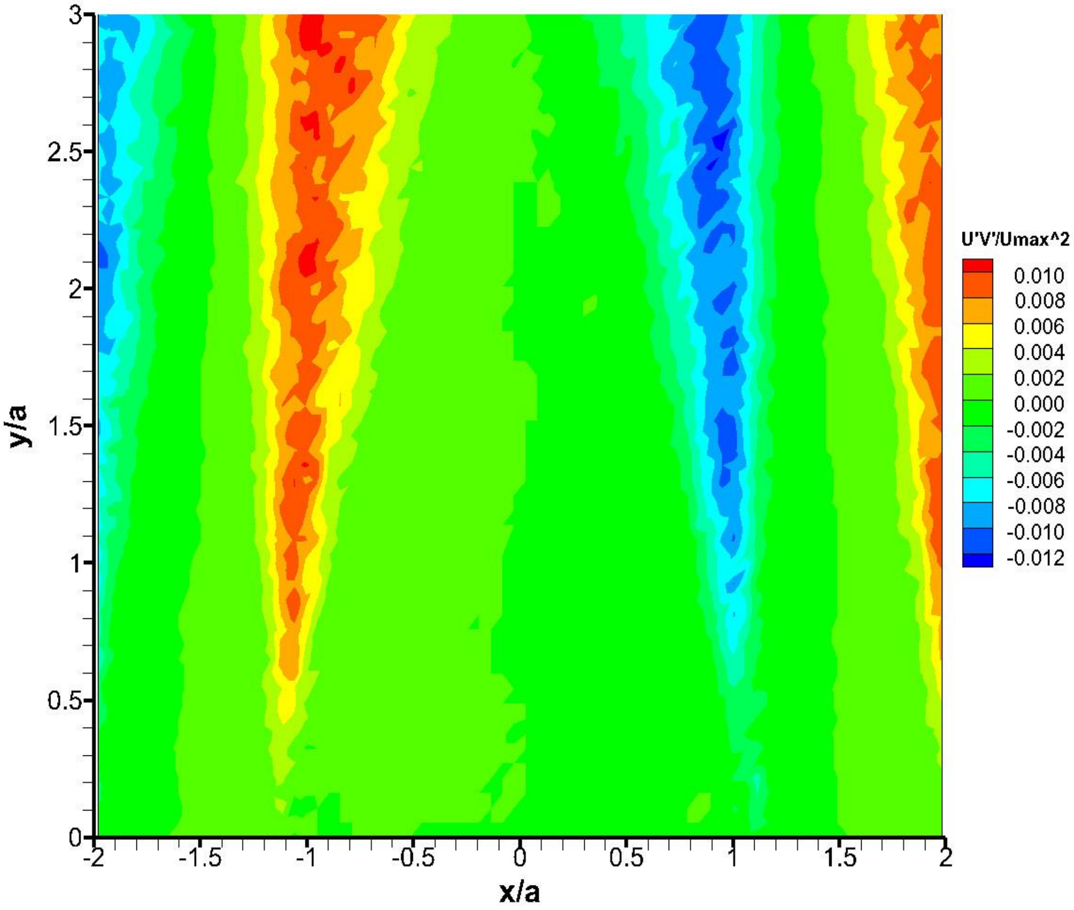

Fig. 51. Reynolds Stress Tensor

4.3 LDA vs. PIV_15Hz

As a comparison, *U* profiles at y = 1.74 (1.72) measured by LDV [30] and PIV are presented at Fig. 52. Results based on both scales M1 (zoom-out view) and M2 (zoom-in view) are shown. Obviously, M2 had many more points than the other two scales due to its high resolution. These three data sets agree very well with the majority of the zones, with the exception of the recirculating zone in which the flow behaviours were complex. Uncertainties of PIV_M1 were calculated using standard deviations based on the three measurements. The errors of PIV_M1 were less than 3% except for those points of velocities close to zero.

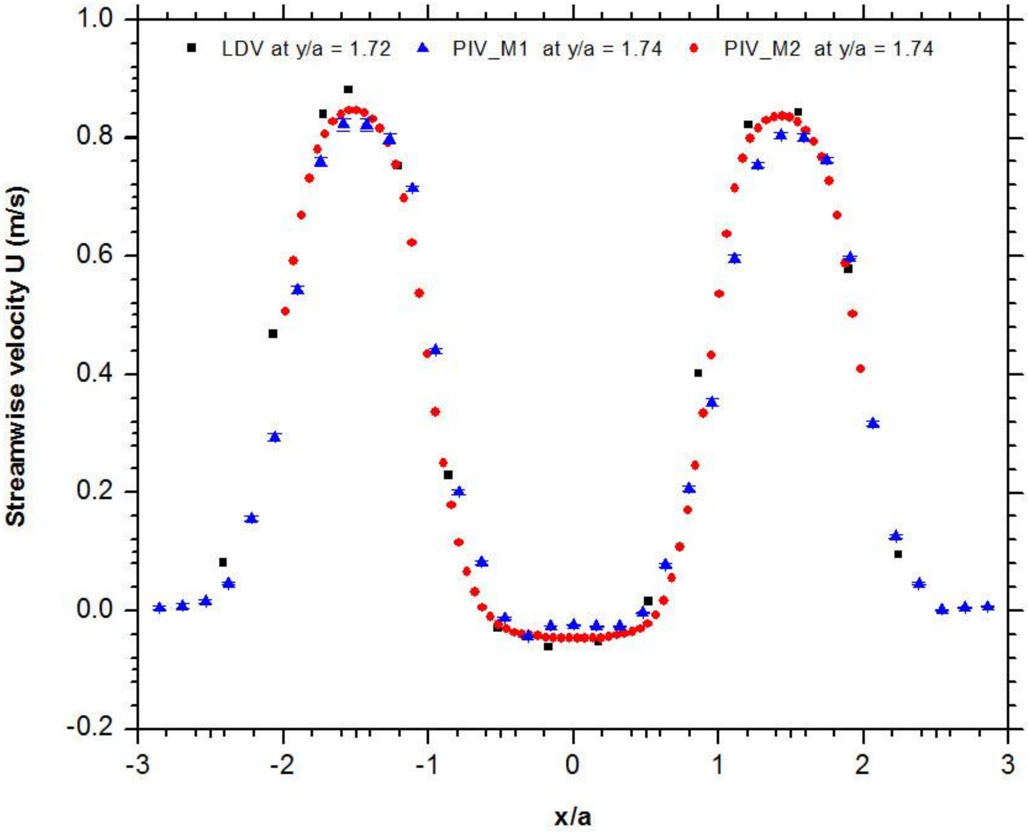

Fig. 52. U profile at y/a = 1.74 (1.72) measured by LDV [18] and PIV (scale of M1 and M2). M1 and M2 refer to different measuring scales. Scale M2 had a higher resolution than that of M1. Error bars of PIV_M1 is the standard deviation of three independent measurements [31].

The comparison of the lateral velocity *V* is shown in Fig. 53. In the core flow regions of the jets, LDA results were higher than the PIV data. These three agreed very well in the recirculating region. As for the comparison between M1 and M2, discrepancies were mainly in the region between *x/a* = 0.5 to *x/a* = 1, in which the shear forces were large. In the middle of the jets, these two results were very close to each other.

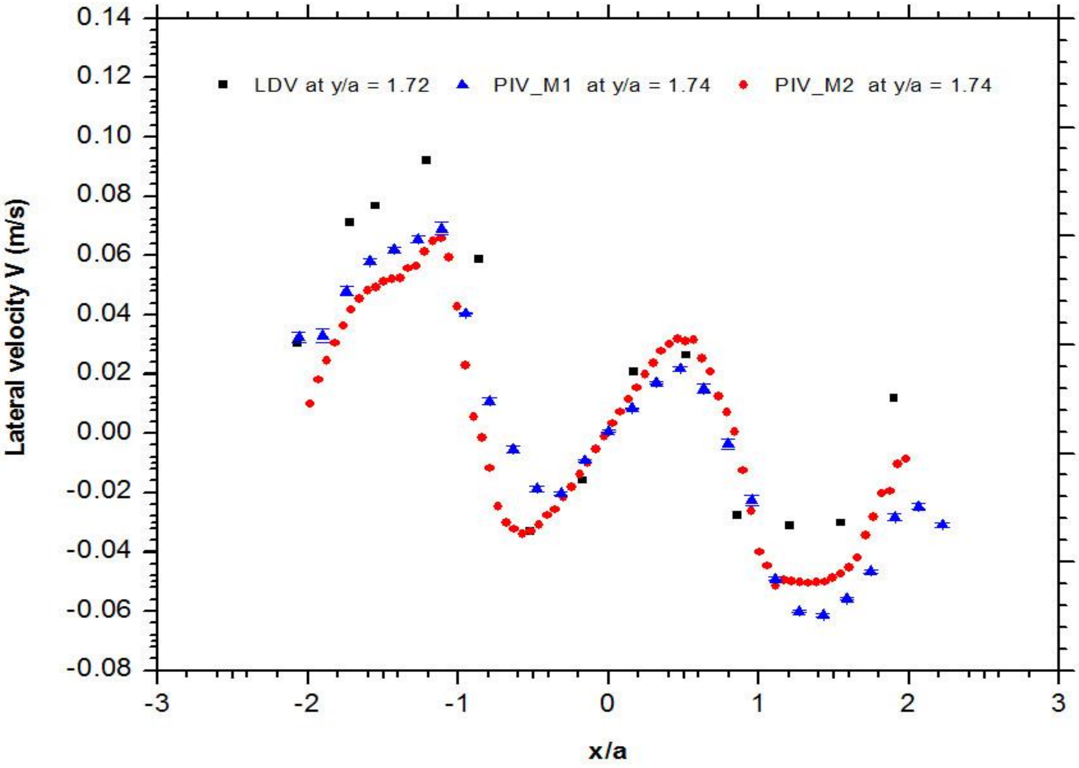

Fig. 53. Lateral velocity *V* comparisons

Figs. 54 and 55 present the comparisons of the results obtained from different measuring techniques for the turbulence intensities in the streamwise and lateral directions. For U_{rms}, the LDA results matched well with the PIV_M2 at the most of locations. In contrast, values from PIV_M1 were much lower than the other two in the inner edges of the jets, where the turbulence intensities reached their maxima. Similar observations were found for the lateral turbulence intensity. This can be attributed to the fact that the fluctuations of the particles cannot be captured accurately when the view is zoomed out.

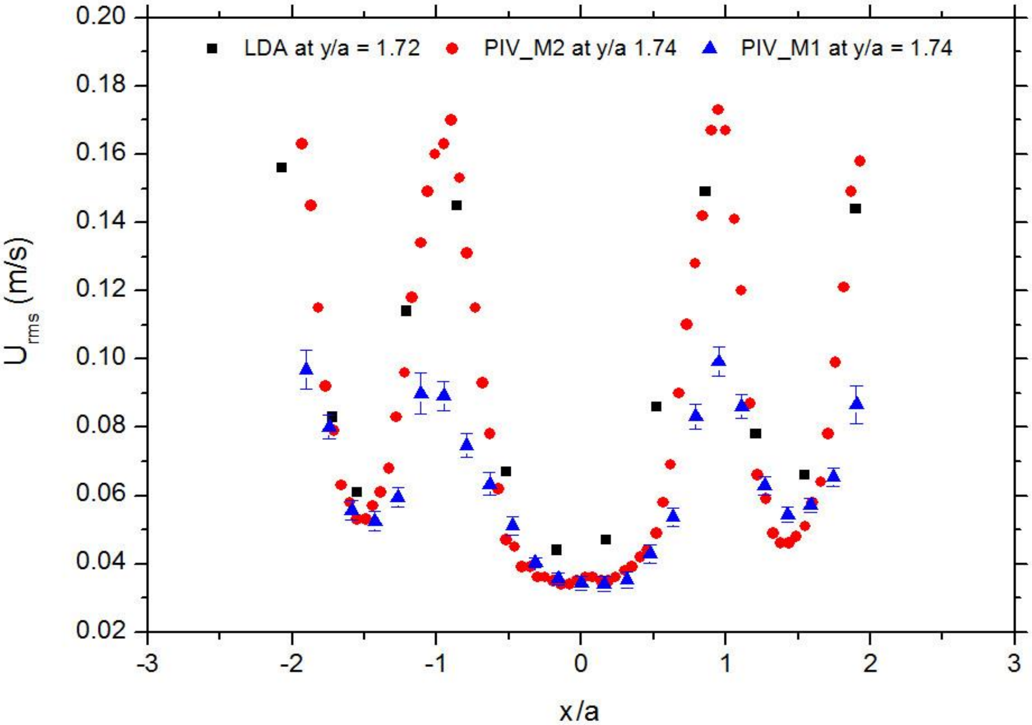

Fig. 54. Streamwise turbulence intensity comparisons

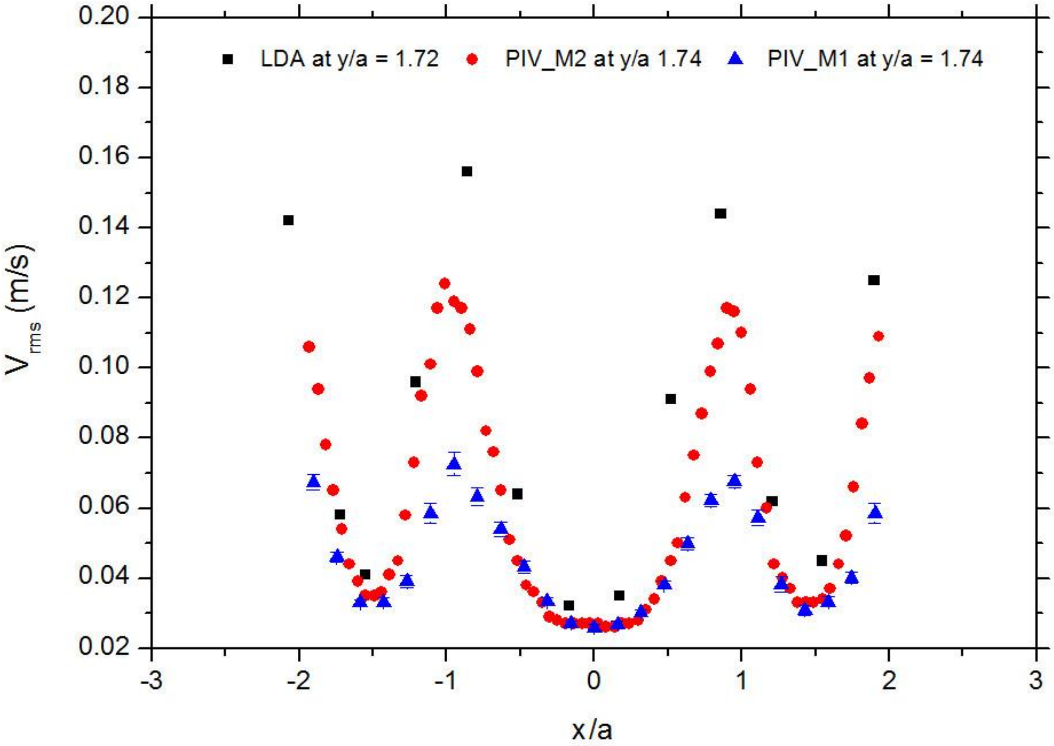

Fig. 55. Lateral turbulence intensity comparisons

The Reynolds stress is the most difficult parameter to be measured accurately in this study due to its small magnitude. As shown in Fig. 56, the LDA results still gave higher values compared to the PIV data in the edges of the jets. PIV_M2 matched well with the LDA results except at certain locations, such as *x/a* = -1. The comparisons between M1 and M2 indicated a good agreement between each other although discrepancies still existed at *x/a* = -1 and 1 at which the Reynolds stress reached the maxima.

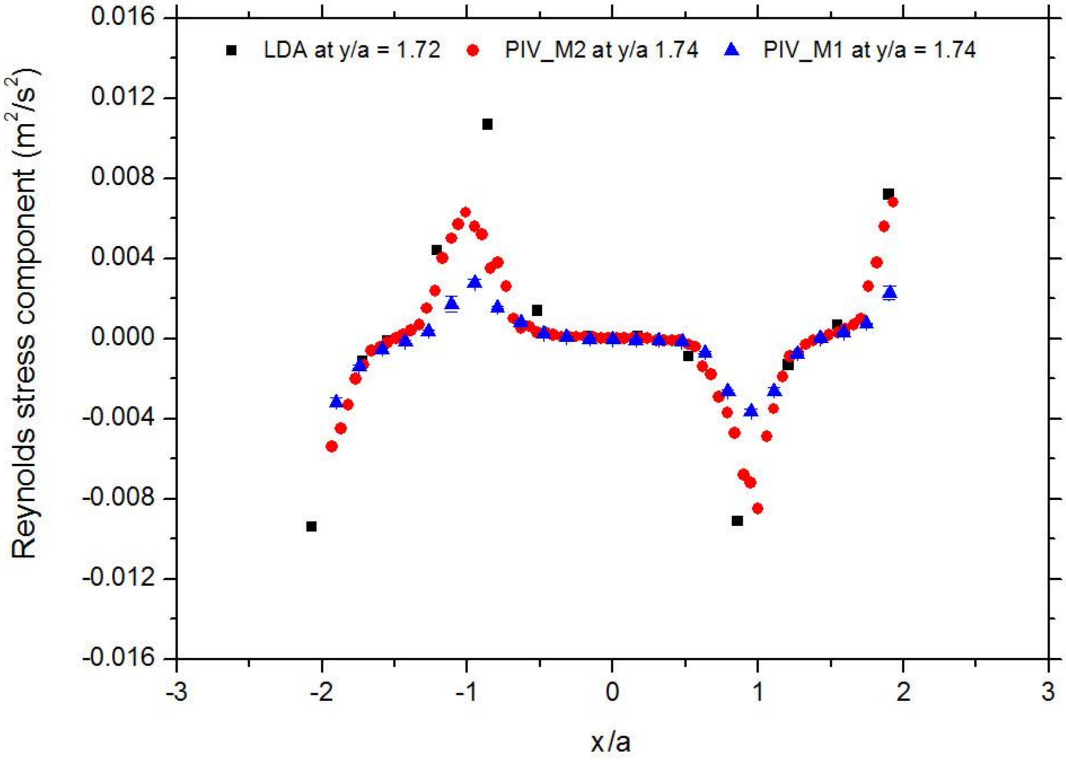

Fig. 56. The Reynolds stress component comparisons

5. CONCLUSIONS

Two-components LDA measurements were carried out to study the mixing condition of twin water jets issuing from two rectangular channels with a nozzle spacing ratio of 3.1 and an aspect ratio of 15.1. The wavelengths of the laser beams used in this work were 660 nm and 785 nm. The channel exit Reynolds number based on the dimensions of the channel was approximately 9100. The outlet condition showed that the flow out of the channel was fully developed turbulent flow. The average turbulence intensity at the measured plane (P2) 10 mm above the exit surface was 8%. The experimental results revealed that the merging point was located between $y/a = 1.72$ and $y/a = 3.45$ and that the combining point was at $y/a = 15.52$.

The turbulence study showed that outer edges of the two jets and the outer boundary of the combined jet had higher levels of turbulence due to high velocity gradients in those regions. The maximum Reynolds shear stress appeared at $y/a = 5.17$, which implies that the flows mix stronger in some location after the merging point. Spectral analysis revealed the scale and the evolution in time of varied-size eddies in the flow at a point in the mixing region.

The averaged quantities obtained by LDA are not only valid for benchmarking steady-state numerical simulations using turbulence models to solve RANS equations but they also enlarge the database of the experimental data for twin jets. This expansion will help propose possible empirical correlations to predict the flow field of parallel jets with small spacing ratios. The spectral analysis of a transient fluctuation velocity signal could be employed to validate the LES results.

Due to certain limitations in the experiment such as laser power, tank material and the fact that LDA is a point-by-point measuring technique, only a single point in the mixing region that had satisfying data rate was investigated. Future work will include the improvement of the data rate of LDA to resolve the dissipation region and PIV to capture the flow at multiple locations simultaneously. The auto-correlation of wavelet coefficients calculated from the PIV data can be utilized to investigate the coherent turbulent structures in the mixing and outer layer regions of the twin jets.

PIV measurements of turbulence mixing in the converging region and partial merging region of two parallel rectangular jets were carried out. The jets were of equal discharge velocity, and were at room temperature. The frame rate of the PIV measurement was 15 Hz, and the time interval between each pair of images was 0.5 ms. The particle used was hollow glasses centered at 10 μm. The study of mean velocities revealed interesting flow behaviors in the circulating zone. Three parts of flow moved at totally opposite directions generating a significant amount of recirculations. The lateral movements of the jets were found to be significant at the inner edges of the jets located between y/a = 1.5 and 6. The MP was located at y/a = 3.5 at which U was equal to zero. Two scales of PIV measurements, scale M1 and M2, were employed. By comparing the mean U profiles measured from two scales of PIV measurements and previous LDA results, it was shown that they agreed very well. The standard deviation of the measurement PIV_M1 was less than 3%. Turbulence studies implied that strong momentum transfer happened in the region ranging from y/a = 3.5 to 8.5. That is, the momentum started to be transferred significantly after the MP. Instantaneous vector fields were evaluated to identify the displacements and growth of vortices as well as their interaction patterns. Future work may include but not limited to the study of coherent turbulence structures using high-frequency PIV systems and evaluation of the uncertainties in the measurements of turbulence quantities resulted from the change of measurement resolutions.

REFERENCES

[1] Erdem, D. and Ath, V., 2002. Interaction of two parallel rectangular jets, Proceedings of 23rd International Congress of Aeronautical Sciences, Sep. 8-13, 2002, Toronto, Canada

[2] Miller, D. R. and Comings, E.W., 1959. Force-momentum fields in a dual-jet flow, Journal of Fluid Mechanics, Vol.7, No.2, 237-256

[3] Tanaka, E., 1970. The interference of two-dimensional parallel jets (1st report, Experiments on dual jet), Bulletin of the JSME, Vol. 13, No.56, 273-280

[4] Tanaka, E., 1974. The interference of two-dimensional parallel jets (2nd report, Experiments on the combined flow of dual jet), Bulletin of the JSME, Vol. 17, No.109, 920-927

[5] Marsters, G.F., 1977. Interaction of two plane parallel jets, AIAA Journal, vol. 15, 1756-1762

[6] Elbanna, H. and S. Gahin, 1983. Investigation of two plane parallel jets, AIAA Journal, Vol. 21, 986-991

[7] Elbanna, H. and Sabbagh, A., 1987. Interaction of two non-equal plane parallel jets, AIAA journal, Vol. 25, 12-13

[8] Ko, N.W.M. and Lau, K.K., 1989. Flow structures in initial region of two interacting parallel plane jets, Exp. Thermal Fluid Sci., 2, 431-449

[9] Lin, Y.F. and Sheu, M.J., 1990. Investigation of two plane parallel unventilated jets, Experiments in Fluids 10, 17-22

[10] Nasr, A. and Lai, J.C.S., 1997. Two parallel plane jets: mean flow and effects of acoustic excitation, Experiments in Fluids 22, 251-260

[11] Behrouzi, P. and McGuirk, J. J., 1998. Laser Doppler velocimetry measurements of twin-jet impingement flow for validation of computational models, Optics and Laser in Engineering, Vol. 30, 265 – 277

[12] Anderson, E. A. and Spall, R. E., 2001. Experimental and numerical investigation of two-dimensional parallel jets, Journal of Fluids Engineering, Vol. 123, 401-406

[13] Yin, Z. Q., Zhang, H. J. and Lin, J. Z., 2007. Experimental study on the flow field characteristics in the mixing region of twin jets, Journal of Hydrodynamics, Ser.B, 19(3), 309-313

[14] Nasr, A. and Lai, J., 2011. An investigation on applying Reichardt's hypothesis to flow prediction of ventilated two parallel plane jets, Advances in Aerospace Science and Applications, Vol. 1, No.1, 1 – 6

[15] Crosskey, M. and Ruggles, A., 2014. UTK Twin Jet Water Facility Computational Fluid Dynamics Validation Data Set, Proceedings of ICAPP, Charlotte, USA, April 6-9.

[16] Durst, F. and Ruck, B., 1987. Effective particle size range in laser-Doppler anemometry, Exp. Fluids 5, 305-314

[17] Flagan, K.W. and Seinfeld, J.H., 1988. Fundamentals of Air Pollution Engineering, Prentice Hall, Englewood, NJ, 296-304

[18] Cenedesse, A., Doglia, G., and Romano, G.P., 1994. LDA and PIV Velocity Measurements in Free Jets, Experimental Thermal and Fluid Science, 9:125-134

[19] Thielicke, W. and Stamhuis, E.J., 2014. PIVlab – Towards User-friendly, Affordable and Accurate Digital Particle Image Velocimetry in MATLAB, Journal of Open Research Software, 2: e30.

[20] Morlet, J., 1981. Sampling Theory and Wave Propagation, Proceedings of the Society of Exploration Geophysicists 51st Annual Meeting and Exposition, Los Angeles, CA, USA

[21] Farge, M., 1992. Wavelet Transforms and Their Applications to Turbulence, Annual Review of Fluid Mechanics, Vol. 24, 395-457

[22] Torrence, C. and Compo, G.P., 1998. A Practical Guide to Wavelet Analysis, Bulletin of American Meteorological Society, Vol. 79, No.1, 61-78

[23] Crosskey, M. and Ruggles, A., 2014. UTK Twin Jet Water Facility Computational Fluid Dynamics Validation Data Set, Proceedings of ICAPP, Charlotte, USA, April 6-9.

[24] Rajaratnam, N., 1976. Turbulent jets (Developments in Water Science, Volume 5), Elsevier Science Ltd, Amsterdam, The Netherlands

[25] Mayo, W.T. Jr, Shay, M.T. and Riter, S., 1974. Digital estimation of turbulence power spectra from burst counter LDV data, Proceedings of the 2nd International Workshop on Laser Velocimetry, Purdue University, West Lafayette, Indiana 16-26

[26] Ramond, A. and Millan, P., 2000. Measurements and treatment of LDA signals, comparison with hot-wire signals, Exp. Fluids 28, 58-63

[27] Hertwig, D., Leitl, B. and Schatzmann, M., 2011. Organized turbulent structures—Link between experimental data and LES, Journal of Wind Engineering and Industrial Aerodynamics 99, 296-307.

[28] Welch, P.D., 1967. The Use of Fast Fourier Transform for the Estimation of Power Spectra: A Method Based on Time Averaging Over Short, Modified Periodograms, IEEE Transactions on Audio and Electroacoustics, Vol. 15, No. 2, 70-73

[29] Li, H. and Nozaki, T., 1995. Wavelet Analysis for the Plane Turbulent Jet, JSME International Journal, Series B, Vol.38, No.4, 525-531

[30] Wang, H., Lee, S., Hassan, Y. A., and Ruggles, A.E., 2016. Laser-Doppler Measurements of the Turbulent Mixing of Two Rectangular Water Jets Impinging on a Stationary Pool, International Journal of Heat and Mass Transfer, Vol. 92, 206-227

[31] Wang, H., Lee, S., and Hassan, Y.A., 2015. Particle image velocimetry measurements of the flow in the converging region of two parallel jets. Nucl.Eng.Des., http://dx.doi.org/10.1016/j.nucengdes.2015.09.032